DISSERTATION

MESOSCOPIC REVELATIONS:
STUDYING THE SHAPE OF AOT REVERSE MICELLES

Submitted by
Christopher D. Gale
Department of Chemistry

In partial fulfillment of the requirements
For the Degree of Doctor of Philosophy
Colorado State University
Fort Collins, Colorado
Summer 2024

Doctoral Committee:

Advisor: Nancy E. Levinger

Amber Krummel
Amy Prieto
Kristen Buchanan

ABSTRACT

MESOSCOPIC REVELATIONS:
STUDYING THE SHAPE OF AOT REVERSE MICELLES

Aerosol-OT (AOT) reverse micelles are a quintessential model system for studying nanoconfinement, creating consistent reverse micelles with a repeatable and very small size (~1-10 nm) using just 3 components. These reverse micelles have been used for studying the behavior of water and solutes in nanoconfinement, modeling the behavior of key solutes and proteins in a system more analogous to *in vivo* work, synthesizing nanoparticles, and even as a vehicle for suspending proteins in a low-viscosity solvent for high quality NMR experiments. Despite their usefulness, AOT reverse micelle's shape is poorly understood, but important to understanding behavior within a reverse micelle. Interfacial properties have been found to be key to many aspects of behavior within AOT reverse micelles and distance from the interface as well as the actual amount of interface present are highly dependent on shape. Therefore, the study of shape is key to a better understanding of AOT reverse micelles and behavior in nanonconfinement. In this work, I develop a series of metrics for shape—coordinate-pair eccentricity (CPE), convexity, and the curvature distribution— and apply them to several simulations of AOT reverse micelles. The simulations were designed to test the impact of the force field on the shape and behavior of the reverse micelles, including the first parameterization of AOT into the OPLS force field. The system was extensively checked to ensure equilibration was achieved and the system was not biased by the starting configuration. To aid in the shape analysis, I have developed a model and a formal proof to predict how the CPE changes for an arbitrary shape as it grows to model the shape behavior of general core-shell structures. Ad-

ditionally, I measured the dipole moment of AOT, the rotational anisotropy decay of water, and several radial distribution functions to provide experimental verification where possible and further explore the behavior of the AOT reverse micelle system.

Several key findings emerge from this work. Most notably, I find that AOT reverse micelles are significantly aspherical and non-convex over every force field tested, providing robust evidence that AOT reverse micelles are aspherical at any given moment in time. This provides strong evidence in support of the idea that experimental observations of spherical particles are the result of ensemble averaging. I also observe that the shape at the AOT/oil interface is comparatively more spherical with a "Goldilock's" value of convexity, neither too high nor too low, compared to the water/AOT interface. My model predicts that the CPE should fall with the addition of a shell, here provided by the AOT surfactant layer, suggesting this is largely the result of geometry. There is great variation between simulations and metrics in their dynamics, but in general, the shape appears to change on the order of 10 ns. This provides a useful method of deducing which values may or may not be impacted by shape, based on the time scale. For instance, it can reasonably be said that shape likely has no impact on water dynamics based on the roughly four orders of magnitude difference in the time scales of each process, which is supported by my own findings. Across all metrics studied, there are noticeable differences between simulations, but none of the differences are consistent. I believe this observation has important implications for both the behavior and simulation of AOT reverse micelles. First, this implies that the forces and interactions giving rise to different aspects of the reverse micelle are complex and largely independent, and that there is a disconnect between molecular-level measurements like radial distribution functions and and mesoscopic-level measurements like shape. Second, this implies that any simulation parameterized on one measure has no guarantee that it reproduces any other aspect of the reverse micelle accurately.

ACKNOWLEDGEMENTS

I would like to, first and foremost, thank my advisor, Dr. Nancy E. Levinger, whose support made this work possible. There are very few advisors who would have supported a project as wildly new, speculative and different from their past work as the work presented here started out as and I will be eternally grateful for her support. Dr. Levinger's insight, patience, and encouragement are the only reason this work is finished, useful or even remotely intelligible. I also need to thank my mentor in molecular dynamics, Dr. Mortaza Derakhshani-Molayousefi, who was a wonderful guide and sounding board. I would like to thank Drs. Revati Kumar, Martin McCullagh, Alexander Hulpke, and Grzegorz Szamel, as well as Donald Minford, M.E.A., who have all helped develop the work here in various ways. Dr. Revati Kumar sparked the discussion that led to significant advancement in the CPE metric. Dr. Martin McCullagh provided expertise and advice for setting up my simulations. Drs. Alexander Hulpke and Grzegorz Szamel and Donald Minford, M.E.A., provided expert feedback and advice in developing the proof for how the CPE changes as a shell is added to an arbitrary shape. I must thank my parents, Chris and Alison Gale, whose support made it possible for me to complete the PhD program, as well as their dogs who were absolutely vital to this work via a certain *je ne sais quoi*. It has never been clear what the dogs do, but we enjoy investigating this mystery.

O sud an caraid dhiarrin-se,
A'n saoghal fiar is fàs.
Is taing O taing gum bheil iad ann,
Ged s ainneamh iad 's gach àit.

—John Campbell, *An Caraid Bu Mhaith Leam*

DEDICATION

DON’T PANIC

“It is a mistake to think you can solve any major problems just with potatoes.”

— Douglas Adams, *Life, the Universe and Everything*

And I took that personally, Mr. Adams

TABLE OF CONTENTS

ABSTRACT ii
ACKNOWLEDGEMENTS iv
DEDICATION v
LIST OF TABLES ix
LIST OF FIGURES x

Chapter 1 Introduction 1
 1.1 Introduction to AOT and Reverse Micelles 1
 1.2 Introduction to Molecular Dynamics Simulation 4
 1.3 Organization of the Dissertation 8

Chapter 2 Simulation Methods 11
 2.1 Creating an OPLS-Based Force Field for AOT 11
 2.2 Simulation Details 13
 2.3 Analysis 14
 2.4 Other Simulations 15

Chapter 3 A Brief Overview of Shape Metrics 21

Chapter 4 Coordinate-Pair Eccentricity (CPE) 27
 4.1 Eccentricity and an Introduction to CPE 27
 4.2 Examining a Continuous Measure of Oblate and Prolate Shapes 31
 4.3 The CPE of AOT Reverse Micelles 34

Chapter 5 Examining How CPE Changes Between Surfaces: Developing and Applying a Model 40
 5.1 Introduction to Changes in CPE Between Surfaces 40
 5.2 Model 42
 5.3 Introduction to ΔCPE 44
 5.4 ΔCPE of AOT Reverse Micelles 45
 5.5 Breakdown of the Model 48
 5.6 A ΔCPE Anomaly 51

Chapter 6 Convexity 59
 6.1 Introduction to Convexity 59
 6.2 Convexity of AOT Reverse Micelles 62
 6.3 Convexity Changes Across Surfaces and the Hedgehog Hypothesis 65

Chapter 7 Curvature Distribution 68
 7.1 Introduction to Curvature 68
 7.2 Curvature Distribution of the CHARMM Simulation 72

Chapter 8 Shape Dynamics 77
8.1 Introduction to Shape Dynamics 77
8.2 Shape Dynamics of AOT Reverse Micelles 78

Chapter 9 Water Rotational Anisotropy Decay 82
9.1 Introduction to Water Rotational Anisotropy Decay 82
9.2 Water's Rotational Anisotropy Decay in AOT Reverse Micelles . 84

Chapter 10 Radial Distribution Functions 89

Chapter 11 Force Field Parameters, Patterns and Groupings 97

Chapter 12 Selected Directions for Future Work with Shape Metrics 103
12.1 Scope and Theory 103
12.2 An Hypothetical Future for CPE 103
12.3 Speculation on the Hedgehog Hypothesis 106

Chapter 13 On the Requirements for Experimental Verification 111
13.1 Defining What we Want to Know 111
13.2 Potential Experiments to Address Each Question 113
13.3 Indirect Evidence of the Shape 118

Chapter 14 Conclusion 121

Appendix A Author Contributions for Published Work 142

Appendix B Model and Proof for the Change in CPE as a Shell is Grown 143
B.1 Introductory Notes 143
B.2 Math Notation 144
B.3 Language 144
B.4 Model 145
B.5 Overture 148
B.6 Mathematical Construction of the Model 149
B.7 CPE Changes with a Constant Increase in the Measures of Shape 152
B.8 How CPE Changes with the Addition of a Constant 158
B.9 Consideration for the Measures of Shape 164

Appendix C Full Data Sets 165
C.1 CPE Raw Distributions 165
C.2 Convexity Time Series 171
C.3 Shape Autocorrelations and Residuals 172

Appendix D OPLS Force Field Parameters for AOT 175
D.1 Atoms and Partial Charges 175
D.2 Intramolecular Parameters 179

Appendix E Relating Semiaxes and Moments of Inertia 183

Appendix F Derivation of CPE Equivalency 185

Appendix G Median of Mean Curvature as a Function of CPE 190

Appendix H Water Rotational Anisotropy Decay, Fit Parameters 195

Appendix I Full Range Radial Distribution Functions 196

Appendix J Concerning Hedgehogs 197

Appendix K Research is Good: But Could it be Better? 199

Appendix L The unanimous Declaration of the thirteen united State Functions of America 201

LIST OF TABLES

2.1 Summary of reverse micelle simulations 13
2.2 Equilibration Schedule for Reverse Micelles 14

D.1 Definition of new atom type needed for modelling the sulfonate moiety . 175
D.2 Atoms and Charges for OPLS Simulations 176
D.4 Definition of bond stretching parameters 179
D.5 Definition of angle bending parameters 180
D.6 Definition of proper dihedral parameters 182

H.1 Fit Parameters 195

LIST OF FIGURES

1.1 a) an artistic rendering of an AOT reverse micelle from my CHARMM simulation. Water and sodium are shown as Van der Waals spheres with red for oxygen, white for hydrogen and deep blue for sodium. AOT is shown in a ball and stick representation. The surface of the reverse micelle is shown as a transparent, glassy surface. b) The structure of AOT, bis(2-ethylhexyl) sulfosuccinate. Counterion not shown. 2

2.1 Depiction of how the surfaces are defined. Lines on the right illustrate which subset of atoms is included in each surface, as numbered, showing how each subsequent surface includes the previous set as well as the new atoms. 16
2.2 The starting configuration, configuration after 10 ns, and after 50 ns of equilibration for both the “reverse bilayer” and “reverse tubular micelle” starting configurations. 18
2.3 (a) Dipole moments of AOT in cyclohexane at a mole fraction of 2.1195×10^{-4} for 1, 2, and 3 AOT molecules. (b) Dipole moments of 2 AOT in 9434 cyclohexane for each force field for AOT used in this work. The black line on yellow indicates the median dipole moment measured over the trajectory, gray box indicates the interquartile range and whiskers indicate the full extent of the data. The red dashed line represents the experimentally measured dipole moment measured in Ref 89. 20

4.1 Two illustrations of how different shapes appear on CPE plots. a) A CPE plot colored according to the oblate/prolate-ishness of the shape. b) A CPE plot colored according to the asphericity of the shape. 30
4.2 (a) The distribution of CPE values observed over the entire trajectory for the CHARMM simulation, 1st surface, as a representative sample. Brighter colors denote a greater number of observations of that value. The cross represents the interquartile range, the cross center represents the median value, and the ends represent the upper and lower quartile in each dimension, rotated with a principal component analysis. (b-f) Summary of the CPE distributions over the entire trajectory for each surface of each simulation as labeled at the top. Here, the proportions of the time the reverse micelle is either oblate/prolate is given as the mean value over all surfaces. 35
4.3 A direct comparison of the average behavior of all surfaces for each simulation. The center of each circle represents the mean of the medians of the CPE distribution for each surface while the radius is roughly equal to the median of the interquartile range for each surface. 37

5.1 (a) The green cylinder represents the core while the purple cylinder represents the shell (shown as a cutaway). The “hairs” shown in yellow represent the additional thickness added to the measures of shape of the core cylinder to create the shell cylinder. This is why the hairs are oriented as shown: extending radial around the length to extend the radius, and normal along the flat ends to extend the length. 43
5.2 a-e) ΔCPE plots for each simulation. The difference distribution is colored so that brighter colors represent values observed more frequently. The percentage of points in each quadrant is provided as text in the respective corners of the plot. f) A comparison of the distributions. The center of the cross represents the median of the distribution and the span of the cross illustrates the interquartile range. 47
5.3 Some cartoons illustrating scenarios where our model breaks down. (a) A shape with sharp corners that a molecule will not fill effectively; (b) a deep, sharp “cut” causing the shell to have overlapping volume; (c) a generally non-uniform shell. 49
5.4 Difference in CPE density distribution for surface 1 between the full dataset at all times and only those times where there is anomalous difference in CPE betwen the inner and outer surface. Both the CPE distribution of the full dataset and only those frames where there is an anomalous difference in CPE were normalized so that they could be directly compared by the difference. Green colors indicate that it is abnormally likely to find an anomalous frame at these CPE values relative to the general likelihood of finding these CPE values over the course of the whole trajectory. Pink indicates that it is unlikely to find these CPE values. 53
5.5 The twist angle between the inner and outer surface of the reverse micelle as a histogram over all times simulated. Colors for each simulation are the same as in Figure 4.3. 55
5.6 Heatmaps of CPE colored according to the median value of mean curvature at the given CPE, averaged over all surfaces, for the simulation as labeled at the top of the plot. 57

6.1 A 2D demonstration of how convexity works. Each color represents a different shape, with each lighter color representing a shape with larger divots between the “petals”. The shapes were designed so that they all share the same convex hull, which is represented by the red dashed line around the outside of the figure. The convexity of several of the surfaces is provided in the textboxes. 61
6.2 (a-e) Convexity distributions for each simulation. The left plots for each simulation show the smoothed histogram of observed convexity values; while the right plots provides a box-and-whisker representation of the convexity distribution, where the center line represents the median, the box represents the interquartile range, and the whiskers encompass 95% of the data, with the remaining 5% considered outliers and plotted as individual points. 63

6.3 (a) Cartoon illustrating the Hedgehog Hypothesis in the low convexity case. (b) Cartoon illustrating the Hedgehog Hypothesis in the high convexity case. (c) Plot of the difference in convexity between surface 5 and surface 1 as a function of the convexity of surface 1. The black line represents the orthogonal distance regression linear fit to all simulations. (d) Cartoon illustrating how one might construct the linear trend observed in subplot c from the endpoints for several different plausible values representing different hypothetical micelles. 66

7.1 a-g) The mean curvature distribution of a selection of different ellipsoids. For each ellipsoid, semiaxis $a = 1$ while semiaxes b and c were varied. The exact values are given as a coordinate-pair in the plot as (b, c). h) A CPE plot for each of the ellipsoids whose mean curvature distribution is plotted above. 71

7.2 The curvature distribution of two random frames from the beginning (a) and end (b) of the trajectory (Legend: Raw Curvature). Each curvature distribution is fitted to the sum of two Lorentzians (Legend: Curves 1/2, and Total Fit). The distribution for the ellipsoid computed from the moments of inertia is also plotted, renormalized so it fits on the graph (Legend: Ellipsoid Curvature). The expected distribution for a sphere of this size is shown to provide a reference for an object this size (Legend: Sphere Curvature). Images on the right show the micelle at these times, colored by curvature with positive values in red. 73

7.3 (a) Mean curvature distribution from the early frame of Figure 7.2. The black vertical line is the median of the distribution. The other shades of gray represent percentile ranges encompassing a given % of the data around the median: from darkest to lightest, 30%, 50%, 70%, 90%. (b) Mean curvature distribution over all times. The example in part (a) represents a single slice of the data presented here, shown as a green line. (c) Gaussian curvature distribution over all times. 76

8.1 Fit parameters from biexponential fits to the CPE and convexity autocorrelations: (a) τ^i_{long}, long time constant, (b) τ^i_{short}, the short time constant, (c) bar graph representation showing how the amplitude is split between the short and long time component. The shades of each color match their corresponding time constant; the bottom, darker colored bar corresponds to A^i_s and the top, lighter colored bar corresponds to A^i_ℓ. 79

9.1 The rotational anisotropy decay for each simulation on a log-log plot. Each simulation is fitted to the sum of two stretched exponentials, shown as black lines. The dashed lines represent the fits for rotational anisotropy decay reported in literature[6,40]. Note that Piletic, *et al.* report time-resolved anisotropy, $r(t)$, which is related to rotational anisotropy, $C_2(t)$ by $r(t) = 2/5C_2(t)$; we multiply their fit by 2.5 to adjust for the difference[6]. . . 85

10.1 RDFs for some key atoms in the AOT reverse micelles, labeled above the plots. This figure focuses on the initial few peaks in the RDF, out to 10 angstroms. 91
10.2 The curvature-discriminated RDFs for each simulation. 94

11.1 A summary of the approximate similarities between simulations across each data type presented in this paper. Static shape refers to both CPE and convexity distributions. Shape dynamics refers to the autocorrelations of CPE and convexity. Water dynamics refers to the rotational anisotropy autocorrelation. Atomic interactions refers to the RDFs, provided in Chapter 10. 98

13.1 a) Plot w_0 versus aggregation number from several literature sources[42,45,46]. Letters after the hyphen denote the method used to measure the aggregation number. LS- light scattering, C- centrifugation sedimentation, S- simulation, SAXS- small angle X-ray scattering. b) A plot of the measured hydrodynamic radius versus w_0 from several literature sources[44,49,153,154]. The black line depicts the average of all datasets which was interpolated onto a common, regular grid. Maitra 1984 is starred because he reports that he used the data from Ref. 153, but his results do not coincide with their results, also plotted. However, Maitra's work is highly influential in the field so I leave it in for completeness. 119

B.1 The green cylinder represents the core while the purple cylinder represents the shell (shown as a cutaway). The "hairs" shown in gray represent the additional thickness added to the measures of shape of the core cylinder to create the shell cylinder. This is why the hairs are oriented as shown: extending radial around the length to extend the radius, and normal along the flat ends to extend the length. 147
B.2 Demonstration of Minkowski sum between the gray polygon, A, and the pink circle, B, to create the new, green shape, C. 149
B.3 A visualization of the vectors and angles arising from the addition of a constant thickness to the measures of shape. Here we show a cylinder as a representative shape with two measures of shape. a) Measures of shape for the outer surface, $\boldsymbol{S}'$ (green), are represented as a vector addition of the inner surface, $\boldsymbol{S}$ (black), and the vector resulting from adding t, $\boldsymbol{S}_t$ (purple). Here we examine the simpler, if uncommon, case where the outer surface can be obtained as shown in the equation below the vectors. As t increases, Θ is seen to decrease. b) The shaded region shows the directions where possible vectors for $\boldsymbol{S}_t$ may point, which follows from all measures of shape being measurable. If $\boldsymbol{S}_t$ is in the green-shaded region, then Θ will decrease. If $\boldsymbol{S}_t$ is in the maroon-shaded region, then Θ will increase. The dividing line is in the direction of $\boldsymbol{S}$ and will change as $\boldsymbol{S}$ changes. In both plots, c represents some scalar value. 161

C.1 CPE distributions for the CHARMM simulations, surfaces as labelled. . . . 166

C.2 CPE distributions for the OPLS-Std simulations, surfaces as labelled. . . . 167
C.3 CPE distributions for the OPLS-CM5 simulations, surfaces as labelled. . . 168
C.4 CPE distributions for the OPLS-RESP simulations, surfaces as labelled. . . 169
C.5 CPE distributions for the CHARMM-4P simulations, surfaces as labelled. . 170
C.6 Raw convexity time series and the associated population distributions for all simulations, as labelled. 171
C.7 a-e) Vector autocorrelations of CPE for each surface as well as the associated fits for each surface. Below the autocorrelations, in a gray plot, is the residuals for each fit. 173
C.8 a-e) Scalar autocorrelations of convexity for each surface as well as the associated fits for each surface. Below the autocorrelations, in a gray plot, is the residuals for each fit. 174

D.1 The index of each atom used in the attached GROMACS files and associated tables. Only non-hydrogen atoms are numbered. 176

G.1 a-e) A heatmap of CPE colored according to the median value of mean curvature when the RM has the CPE value indicated for the CHARMM simulation. Each subplot displays the mean curvature as a function of CPE for the surface as indicated at the top of the plot. f) The average distribution of mean curvature as a function of CPE over all surfaces. 190
G.2 a-e) A heatmap of CPE colored according to the median value of mean curvature when the RM has the CPE value indicated for the OPLS-Std simulation. Each subplot displays the mean curvature as a function of CPE for the surface as indicated at the top of the plot. f) The average distribution of mean curvature as a function of CPE over all surfaces. 191
G.3 a-e) A heatmap of CPE colored according to the median value of mean curvature when the RM has the CPE value indicated for the OPLS-CM5 simulation. Each subplot displays the mean curvature as a function of CPE for the surface as indicated at the top of the plot. f) The average distribution of mean curvature as a function of CPE over all surfaces. 192
G.4 a-e) A heatmap of CPE colored according to the median value of mean curvature when the RM has the CPE value indicated for the OPLS-RESP simulation. Each subplot displays the mean curvature as a function of CPE for the surface as indicated at the top of the plot. f) The average distribution of mean curvature as a function of CPE over all surfaces. 193
G.5 a-e) A heatmap of CPE colored according to the median value of mean curvature when the RM has the CPE value indicated for the CHARMM-4P simulation. Each subplot displays the mean curvature as a function of CPE for the surface as indicated at the top of the plot. f) The average distribution of mean curvature as a function of CPE over all surfaces. 194

I.1 Radial Distribution Functions for some key atoms in the AOT reverse micelles, labeled above the plots. This figure shows the full range of the RDF, out to the maximum distance possible for the simulations performed here and showing that the RDF has decayed to 0. 196

Chapter 1

Introduction

Portions of the information in this chapter have been published in Refs. 1–3. Specific author contributions are provided in Appendix A.

1.1 Introduction to AOT and Reverse Micelles

Aerosol-OT (AOT) has long been used to study water in nanoconfinement[4]. AOT is a trade name, hinting at the long history and industrial uses of the surfactant, whose chemical name is bis(2-ethylhexyl)sulfosuccinate, usually given as the sodium salt. The structure of AOT is shown in Figure 1.1. A plethora of studies, from characterizing molecular behavior in nanoconfinement to templating nanoparticle synthesis[5–15] make AOT reverse micelles exceptionally well characterized, and therefore a great system for testing new characterization methods. AOT is interesting in this work for it's ability to create reverse micelles, which are self-assembled particles comprising a water (or more generally, a polar) core and surfactant layer dispersed in a non-polar phase. An example of a reverse micelle from my simulations is shown in Figure 1.1. AOT reverse micelles are particularly useful because they produce highly consistent reverse micelles approximately 1-10 nm in diameter[4]. At sizes this small, there is a countable number of water molecules inside, allowing scientists an opportunity to study how the properties of water change in the intermediate regime between the microscopic and the macroscopic.

It is known that the properties of water shift inside of nanoconfinement, sometimes quite dramatically. For instance, previous results show a size-dependent drop in both rotational and translation water motion[16], and even the hydrogen exchange with protic solutes in reverse micelles slows down[9,17]. There are also unique spectroscopic signatures seen in nanoconfined water from numerous sources, clearly

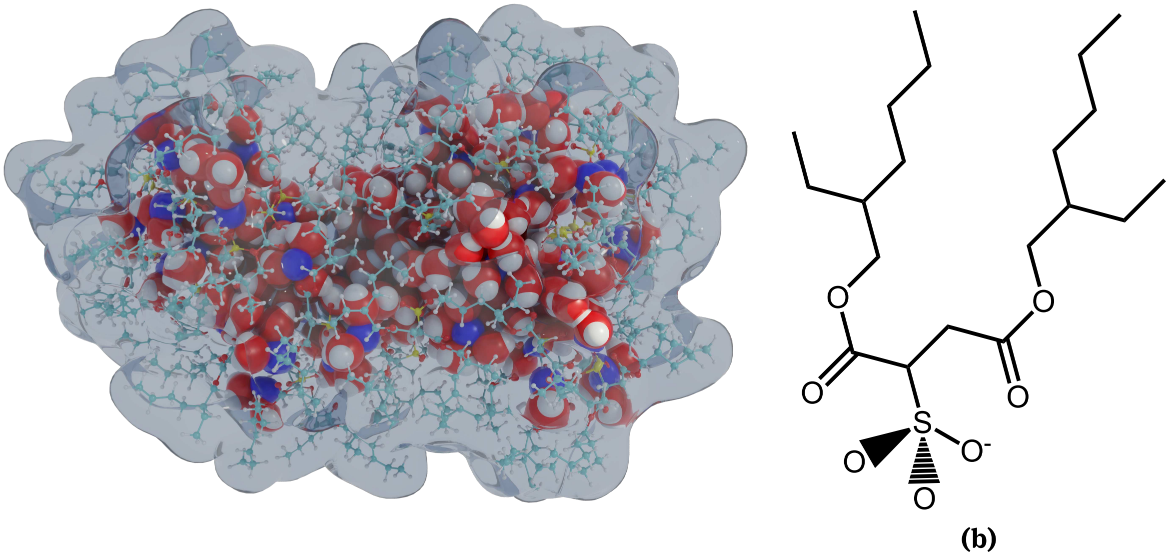

(a)

(b)

Figure 1.1: a) an artistic rendering of an AOT reverse micelle from my CHARMM simulation. Water and sodium are shown as Van der Waals spheres with red for oxygen, white for hydrogen and deep blue for sodium. AOT is shown in a ball and stick representation. The surface of the reverse micelle is shown as a transparent, glassy surface. b) The structure of AOT, bis(2-ethylhexyl) sulfosuccinate. Counterion not shown.

demonstrating that nanoconfinement is a unique environment with behavior not seen in bulk solutions[4,6,18–23]. Several studies have suggested the solutes inside of the nanoconfined water pool are not uniformly distributed but tend to preferentially be observed at the interface[8,9,24–26]. This has led to the general assumption that there are two water populations inside of reverse micelles, a core and a shell population[6], which suggests that water's behavior is governed by it's proximity to a soft and changeable interface. This implies that the shape of the reverse micelle plays a pivotal role in the behavior observed in nanoconfinement. This would be a trivial issue if AOT reverse micelles were spherical, like many past works have implicitly assumed[6,27–35]; however, all-atom molecular dynamics simulations consistently show the reverse micelles adopt shapes that are anything but spherical[36–43].

As a three component system, three degrees of freedom are required to completely specify the stoichiometry of the reverse micelle system. One of the most important parameters is known as w_0, given by (1.1).

$$w_0 = \frac{[H_2O]}{[AOT]} = \frac{n_{H_2O}}{n_{AOT}} \tag{1.1}$$

In (1.1), n_{H_2O} and n_{AOT} represent the number of molecules for H_2O and AOT, respectively, illustrating the key point: that w_0 directly represents the number ratio of water molecules to AOT molecules in a given reverse micelle. It is the w_0 that governs the size of AOT reverse micelles in experiment, and there are consistent relationships between the w_0 and the size[8,9,25,39,44]. To define the stoichiometry of the rest of the system, usually the total volume is set in some way, *e.g.* in experiments it is a simple matter of deciding how much solution to make, w_0 is set by experimental design, and one more relation has to be defined. This is usually just the concentration of AOT in the non-polar solvent of choice and the system will reach an equilibrium value for the total number of reverse micelles in solution and the AOT molecules per reverse micelle. However, in simulation, the number of AOT molecules must be explicitly defined. This is done with a parameter known as the aggregation number, which is simply the number of AOT molecules per reverse micelle. This value is very important to the simulation of AOT reverse micelles because too large of an aggregation number will create too large of a reverse micelle and vice versa. The effects of the aggregation number on the properties of reverse micelles have been noted several times before[40,42]. Experiments have measured the aggregation number and generally agree well, but with less precision than would be preferred[42,45,46].

AOT reverse micelles are very well characterized, but there is continued ambiguity on the shape of AOT reverse micelles. Many experimental works simply assume that the aggregates are spherical[27–31,34,35], although other experimental works observed non-spherical reverse micelles in certain situations[39,47–49]. Early simulations applied the same simplifications and assumed a spherical micelle[33], but the all-atom molecular dynamics simulations enabled by modern computing power have universally found the reverse micelles adopt a non-spherical shape, evidenced by snapshot images of the simulated reverse micelle[36–43]. The discrepancy between some experiments and the findings of all-atom molecular dynamics simulations could be explained by the ensemble averaging of the small-angle scattering experiments that report spherical reverse micelles. These experiments average over large numbers of particles and large amounts of time, and so theoretically, any flexible, pulsating particle is likely to appear spherical. This point of view is supported by the fact that not all experiments observe a spherical particle[39,47–49]. Simplifying assumptions are often made about AOT reverse micelles, *e.g.* that the reverse micelles are spherical, to build a framework for understanding the results[6,32]. For example, Piletic, *et al.*, used non-linear IR spectroscopy to demonstrate two distinct water environments, "shell"and "core"water, and calculated the thickness of the shell assuming a spherical shape[6]. Significant work needs to be done to account for a non-spherical particle, which is only sometimes possible[50]. In this work, I study the shape of the reverse micelles thoroughly to help determine if the observation of spherical reverse micelles is the result of ensemble averaging or some other reason. This work will also provide some tools for evaluating and working with non-spherical and amorphous configurations to aid in theoretical works on the subject.

1.2 Introduction to Molecular Dynamics Simulation

Molecular dynamics simulations have become a powerful tool for studying the behavior of many chemical systems, especially biological systems[51–54]. Molecular dynamics is a simulation that uses classical mechanics to propagate the system forward in time by some small increment, resulting in a trajectory that contains frames, or snapshots in time, in much the same way that a movie is made of a series of still images. A "force field" is the name given to the collection of all the parameters that are used to compute the interactions between atoms in the simulation and compute the forces. There are several different force fields available, developed by different people and groups for different purposes, including several common force fields. These common force fields are typically stored and handled internally by the molecular dynamics engine being used. This is such that for many simulations, particularly for protein simulations, there are sufficient tools and internal methods available that a student might be able to create a realistic and useful simulation without ever knowing how a force field worked.

The force field is then used to compute the forces between each atom pair in a simulation, which are then used in Newton's equations of motion and integrated to find the positions and velocities of the next step of the simulation[55,56]. With modern computing resources, MD simulation can easily range between tens of thousands of atoms to a few million atoms for several microseconds of total simulation length. The simulation can be one of several ensembles. Because this is a purely classical simulation method, bond breaking is not typically feasible to simulate[1]; so the number of molecules and atoms is set by the initial configuration of the simulation. Thermostats and barostats can be used to control the temperature and pressure of the simulation. Thermostats operate by scaling the velocities of all of the atoms to maintain a constant temperature for the system[57–61], while barostats scale the simulation box size and atom coordinates to maintain a constant pressure[58,62]. With the right choice of each, it is possible to create a simulation in the classical ensemble[57,59,60,62]. Finally, to simulate a system that behaves as if it is a part of a large solution with many times the volume possible with even a few million atoms, MD simulations almost always use periodic boundary conditions. These conditions link sides of the box so that a particle going out of, *e.g.* the right side of the box, will come back in the left side of the box. Equivalently, the periodic boundary conditions can be thought of as creating

---

[1] There are options available for simulating chemical reactions with molecular dynamics with different levels of approximations and computational expense, but they are beyond the scope of this work

a series of periodic copies, or images, of the simulation box around every face, edge, and corner of the simulation box. The periodic boundary conditions then effectively minimize edge effects and artifacts that might arise from a simulation bounded by a hard wall if they are not used, mimicking behavior found in a much larger system.

As previously stated, the force field is the collection of all the parameters that govern how every part of the simulation interacts with every other part of the simulation. These parameters are split into intra- and intermolecular interactions. Intramolecular interactions govern how bonded atoms behave, including 2 atom stretching, 3 atom bending, and 4 atom dihedral twisting. The intermolecular interactions, governing how atoms interact through space rather than through bonds, always involve pairwise interactions, split into an electrostatic portion and another potential representing all of the other quantum effects of interactions, usually represented by a Lennard-Jones potential. Each force field may use a different specific function for each term, but generally the potential energy function can be written as (1.2), which is the CHARMM force field's potential energy function but is a good representative example[63].

$$\begin{aligned} U(\mathbf{r}) = \sum_{\text{bonds}} K_b(b-b_0)^2 + \sum_{\text{UB}} K_{UB}(S-S_0)^2 + \sum_{\text{angle}} K_\theta(\theta-\theta_0)^2 + \\ \sum_{\text{dihedrals}} K_\chi(1+cos(n\chi-\delta)) + \sum_{\text{impropers}} K_{imp}(\varphi-\varphi_0)^2 + \\ \sum_{\text{nonbond}} \epsilon\left[\left(\frac{R_{min_{ij}}}{r_{ij}}\right)^1 2 - \left(\frac{R_{min_{ij}}}{r_{ij}}\right)^6\right] + \frac{q_i q_j}{\epsilon_\ell r_{ij}} \end{aligned} \tag{1.2}$$

In (1.2), the first term accounts for the bond stretching, the second is the Urey-Bradley term which accounts for two-body interactions separated by a bond, *e.g.* 1,3 interactions, the third term accounts for 3-body angle bending, the fourth term accounts for proper dihedrals, the fifth term accounts for improper dihedrals[2], and the last term includes all of the non-bonded interactions including both a Lennard-Jones potential and an electrostatic interaction potential. The K_k terms are the various force constants, b, S, θ, χ, and φ are the bond length, Urey-Bradley 1,3-distance, bond angle, dihedral angle, and improper torsion angle, respectively. In the Lennard-Jones potential, ϵ is the well depth and $R_{min_{ij}}$ is the distance of the Lennard-Jones minimum, *e.g.* the location of the potential well, while r_{ij} is the distance between atoms i and j. Similarly, q_i and q_j are the charges on atoms i and j, and ϵ_ℓ is the effective dielectric constant. The Urey-Bradley potential is not used by every force field while improper dihedrals are used as a tool to enforce planarity on certain molecules and neither need be considered too much here. The purpose of (1.2) is to illustrate that the forces on all atoms are the sum of several intramolecular terms as well as an electrostatic and typically a Lennard-Jones term to model the intermolecular interactions.

It is important to understand how the intermolecular terms interact with each other. The Lennard-Jones potential provides a useful and convenient qualitative model of the behavior between particles with a variety of quantum mechanical origins, *e.g.* the Van der Waals forces. However, it is difficult to directly measure the potential well between atom pairs precisely, but while electrostatics are relatively easier, being entirely determined by just one atom's properties in a molecule, they are also somewhat nebulous as it is difficult to experimentally determine the contribution of a single atom to the electrostatic properties of an entire molecule. On top of the issues with precisely matching these parameters to real life, it is also important to note that this is a classical representation of a quantum mechanical system. This makes MD inherently reductive, to some degree, requiring that the parameters

---

[2] Dihedrals are a 4-body interaction. A proper dihedral involves twisting along the bond between atoms 2 and 3 as measured by the relative orientations of atoms 1 and 4. An improper dihedral is a tool used to enforce planarity for molecules which need it.

be tuned to reproduce behavior rather than strictly reproducing the values they are meant to represent. Theoretically, the atom-wise electrostatic interactions are computed from the wavefunction of the molecule but there are numerous ways to compute the partial charges on atoms based on the same set of wavefunctions[64], and of course, multiple different sets of wavefunctions can be obtained at different levels of theory. The Lennard-Jones potential, used as a qualitative model of complex behavior, is purely empirical and a function that is always fitted to reproduce some experimental metric via either MD simulation or a similar method like Monte Carlo simulation[63,65,66]. This means that the intermolecular forces are at least somewhat colinear and there are multiple combinations of Lennard-Jones and electrostatic parameters that would likely give similar results for a given simulation parameterized on a given experimental measure, which is a large part of why so many different force fields exist.

1.3 Organization of the Dissertation

In this work, I created a series of five simulations of otherwise identical AOT reverse micelles using different force fields, varying both the force field for AOT and isooctane as well as utilizing different water models. These simulations were analyzed using a series of metrics of shape I developed to gain better understanding of what the shape of AOT reverse micelles are as well as the parameters important for those shapes. I also analyzed the dynamics of shape via the autocorrelation functions of the shape metrics. Finally, I performed some additional analyses, specifically computing several radial distribution functions and the water rotational autocorrelation functions. AOT reverse micelles are often used as a way to study the behavior of water in nanoconfinement and the rotational dynamics of water are an integral part of the study of water in nanoconfinement. Studying water's dynamics helps provide some comparison to past work as well as a method for investigating what impact shape has on the water's behavior. Meanwhile, the radial distribution functions are used to study molecular-level organization. Therefore, the radial distribution functions provide a connection between the study of shape and past work on AOT reverse micelles.

The remainder of this dissertation is organized in much the same way as the typical journal article that is split by topic. I start with the methods employed as well as introductory theory before considering each analysis as its own chapter, presenting both the results and discussion of those results in its own chapter. The last chapters are dedicated to higher level discussions using the information from multiple different metrics and chapters to see how it all fits together and then finishing with conclusions.

In particular, Chapter 2 addresses how the simulations used in this work were created. Chapter 3 discusses the theory behind the shape metrics employed in this work. The metrics I developed are by no means perfect, and Chapter 3 serves to illustrate why I chose the metrics I did and why I believe they represent adequate solutions to a challenging problem. Chapters 4-7 address each shape metric, including the formal definition of the metric, interpretation of the metric, the results obtained with the metric and discussion. Chapter 4 discusses coordinate-pair eccentricity (CPE), Chapter 5 addresses how CPE changes within the context of a core/shell model, Chapter 6 discusses the convexity, and Chapter 7 discusses the curvature distribution. Chapter 8 presents the shape dynamics as measured by the autocorrelations of CPE and convexity. Chapters 9 and 10 provide additional results unrelated but complementary to shape; Chapter 9 discusses the rotational dynamics of water within the reverse micelles and Chapter 10 discusses several calculated radial distribution functions. This entire project was originally predicated on the idea that changing the force field used in the simulations would allow patterns to emerge which indicate which parameters impact shape, how shape impacts other parameters (such as water dynamics), and potentially hint at the accuracy of the different force fields used. Therefore, Chapter 11 looks at all of the data presented in this work in aggregate to analyze the patterns between that have emerged. Chapter 12 is dedicated to some of the unfinished portions of this work and presents the progress I've made on these areas in the hopes of helping future researchers in these areas. Chapter 13 analyzes how this work relates to experimental findings and what instrumental requirements might be needed to confirm different aspects of our findings. Finally, Chapter 14 presents conclusions.

Chapter 2

Simulation Methods

Portions of the information in this chapter have been published in Refs. 1–3. Specific author contributions are provided in Appendix A.

2.1 Creating an OPLS-Based Force Field for AOT

I have created five simulations of AOT reverse micelles. Each simulation differed in the force field used to model the system. One simulation used the CHARMM36 force field for AOT and isooctane[36,67,68] and the TIP3P water model[69], the most commonly used parameters for all-atom MD simulations of AOT reverse micelles at present[36,38–43,70]. We created second simulation with a minor modification to the CHARMM simulation by using the same force field for AOT and isooctane but using the TIP4P/2005 water model[69,71], to understand how the water model impacts the shape and behavior of the reverse micelle. This simulation is expected to be quite different because CHARMM was specifically parameterized for use with the TIP3P water model[68]. I then introduce the OPLS force field to explore how the AOT model impacts the reverse micelle. Currently, no major force field family other than CHARMM models a sulfonate-bearing surfactant without modification. I chose the OPLS force field because the majority of the reverse micelle simulation comprises organic molecules, and the OPLS force field was designed for simulating organic molecules[65,72]. We used literature values to properly simulate the sulfonate group[73,74]. The literature values were parameterized for a sulfonate-bearing ionic liquid[73] and linear alkyl sulfonate surfactant[74] so none of the parameters are specific to the AOT molecule.

Without performing an expensive, full parameterization of AOT in the OPLS force field, I instead created two additional simulations that modify the partial charges on all atoms of AOT. Although this does not guarantee the parameters are accurate, with enough variation, it should at least ensure that the force fields straddle a minimum (with respect to any particular metric), with the additional benefit that these scheme will demonstrate specific parameters' impact on the reverse micelle's behavior. To do this, I obtained the molecular orbitals for the AOT anion using a density functional theory calculation. Geometry was optimized at the M06/pc-1 level with a level-shift algorithm to help converge the wavefunction to a solution using GAMESS[75–77]. At the single, optimized geometry, a single-point calculation using M06/pc-2 was performed to produce a final set of orbitals. These orbitals were used to compute the partial charges on every atom of AOT using the *Multiwfn* program[64]. I used both the Hirshfeld-based, CM5 method[78], as well as the electrostatic-potential-mapping method, RESP[79]. While only a single geometry was used to compute the charges, the results produced very little differences between chemcially-equivalent atoms or between the two tail groups, likely due to the fact that the majority of atoms in AOT are prototypical non-polar alkanes. All simulations employing OPLS-based force fields used the TIP4P/2005 water model[69,71]. Details about the OPLS force fields, including inter- and intramolecular parameters and partial charges are provided in Appendix D. The different force fields involved and the naming conventions we assign them in this paper are summarized in Table 2.1.

Table 2.1: Summary of reverse micelle simulations

Name	AOT+Solvent Model	Water Model	Notes
CHARMM	CHARMM36	TIP3P	
CHARMM-4P	CHARMM36	TIP4P/2005	
OPLS-Std	OPLS	TIP4P/2005	Sulfonate values from literature - Charges and intramolecular parameters[a] LJ parameters[b]
OPLS-CM5	OPLS	TIP4P/2005	OPLS-Std, with CM5 atomic charges
OPLS-RESP	OPLS	TIP4P/2005	OPLS-Std, with RESP atomic charges

[a] Parameters taken from Ref. 73

[b] Parameters taken from Ref. 74

2.2 Simulation Details

All reverse micelles were set to $w_0 = 5$, which has been shown to exhibit the effects of nanoconfinement clearly[6,16,33]. Each simulation used an aggregation number of 42, meaning that there were 210 water molecules. This mimics the numbers provided by the Abel lab, the only resource online providing stoichiometry suggestions for several reverse micelles, and fit well with the current best experimental estimates for $w_0 = 5$ reverse micelles[1,36,42,44,45]. The reverse micelle was dissolved in 1500 isooctane molecules. Using the average box dimensions of the simulations, the concentration of AOT in isooctane was ~0.17 M. All starting configurations were packed using PACKMOL[80]. The simulations were performed using the 2019 edition of GROMACS[55,56,81]. For all simulations, the system was minimized by steepest descent to remove bad contacts. The system was then equilibrated for a total of 10 ns in the NPT ensemble using a series of heavy-atom (*e.g.* non-hydrogen atom) position restraints as described in Table 2.2. This system was designed to heavily bias the system toward spherical geometries to prove that any non-spherical geometries that might be observed were not an artifact of the starting structure. Equilibration used the V-rescale thermostat[61] and Berendsen barostat[58] with a 2 fs step size. Following this, a production run of 1 μs was performed using the V-rescale thermostat[61] and Parrinello-Rahman barostat[57,62] with a 2 fs step size, saving the coordinates every 8 ps. To study water dynamics, I created a short, 100 ps extension to the production run, saving the coordinates every 0.1 ps, with all other parameters kept the same. Both the equilibration and production runs were held at 1 bar and 298 K. All simulations used the Particle Mesh Ewald scheme for computing electrostatic interactions[82].

Table 2.2: Equilibration Schedule for Reverse Micelles

Step Time (ns)	Total Time Equilibrated (ns)	Position Restraints (kJ/mol)		
		Water	AOT	Isooctane
0.2	0.2	1000	1000	1000
0.5	0.7	1000	1000	0
0.1	0.8	1000	500	0
0.1	0.9	1000	0	0
0.1	1.0	500	0	0
9.0	10.0	0	0	0

2.3 Analysis

For each simulation, the micelle was divided into five sufaces to study how the shape changes between the inner water pool and the oil/surfactant interface. Surfaces are numbered starting from the interior, so that surface 1 corresponds to the shape of the water pool and surface 5 corresponds to the shape of water+Na^++AOT.

Each surface is created by defining a subset of the atoms in the micelle, with each subset being contained and expanded on in the next subset, *e.g.* surface 1 is defined as all water molecules, surface 2 is defined as all water plus the sodium plus the sulfonate-group atoms, *etc.* The exact atoms in each surface are shown visually in Figure 2.1. To compute CPE, the atoms contained in each surface's subset are used to calculate the moments of inertia. To compute convexity and the curvature distribution, the atoms contained in each surface are used to generate a Willard-Chandler surface that was then used for the analysis[83]. Custom Python code was used for all analyses, with key packages including the MDAnalysis package for manipulating the simulation trajectory[84,85], the PyTim package for computing the Willard-Chandler surface[86], and the PyVista package for manipulating the mesh surfaces[87]. The code is provided on GitHub[88].

2.4 Other Simulations

I also ran two more sets of simulations to explore different aspects of the AOT reverse micelle system. The first two were designed as checks of my equilibration procedures intended to test whether I effectively removed starting structure artifacts in the observed shapes or not. The second set was designed to measure the dipole moment to compare how the various force fields simulated here match against experiment.

I simulated two alternative starting structures using the same stoichiometry as for the reverse micelles described above to test whether an alternative stable configuration existed, which if such a structure exists, would imply that the observed shapes in the other simulations are not truly representative of the equilibrium shapes of AOT reverse micelles. Both of these simulations were based on known surfactant formations: tubular micelles and bilayer sheets. In one simulation, I form a "reverse tubular micelle", where the water was contained within a cylinder 4 Å in diameter and 35

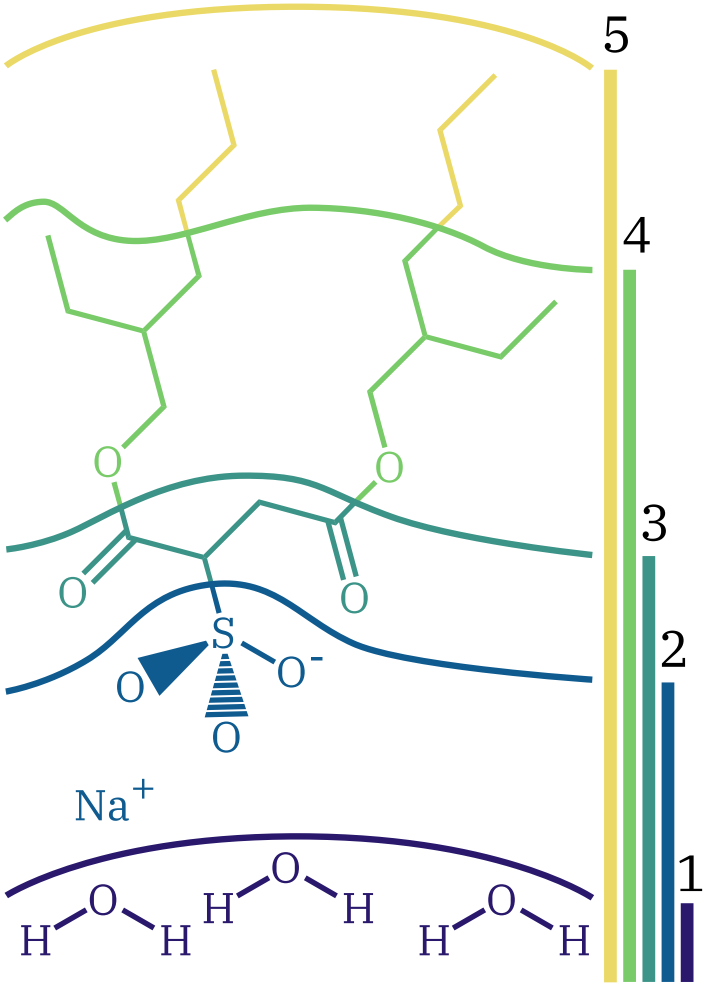

Figure 2.1: Depiction of how the surfaces are defined. Lines on the right illustrate which subset of atoms is included in each surface, as numbered, showing how each subsequent surface includes the previous set as well as the new atoms.

Å long with sodium and AOT covering the surface of the water pool. In a similar simulation, I form a “reverse bilayer” configuration, with water contained in a rectangular prism with dimensions 23 Å × 23 Å × 6 Å. The exact dimensions were somewhat arbitrary and primarily chosen to be such that the AOT could cover the surface of the water pool effectively. These simulations were equilibrated identically to the other AOT reverse micelle simulations, and then allowed to run for an additional 40 ns under identical conditions with no position restraints. Images of the starting structure, structure at the end of the regular equilibration schedule, and at the end of a 50 ns run for each simulation are shown in Figure 2.2. While the results were not perfectly identical to those found with a spherical start after the normal equilibration schedule, this is neither surprising nor proof of a stable alternative configuration. These simulations started from a configuration that was significantly farther from the equilibrium shapes observed in our other simulations, so it is reasonable that they take longer to reach equilibrium. As Figure 2.2 shows, after a longer equilibration, they are functionally indistinguishable from the normal amorphous shapes observed in the other simulations. Both of these alternative starting configuration simulations used the CHARMM force field with TIP3P water and the V-rescale thermostat[61] and Berendsen barostat[58] with a 1 fs step size with coordinates saved every 2 ps, following the system of heavy atom position restraints presented in Table 2.2.

There are not many ways to validate a force field for AOT reverse micelles, and in one sense, almost all of the work performed here is an attempt to validate these force fields as best may be. However, one metric that can be measured both experimentally and theoretically and should have some impact on the validity of AOT reverse micelle simulations is the dipole moment of AOT. The dipole moment provides a good measure of the electrostatic properties of the force field as well as how the AOT molecules interact with each other. I compared our simulations against an experiment of AOT in cyclohexane at successively more dilute concentrations[89]. All simulations used

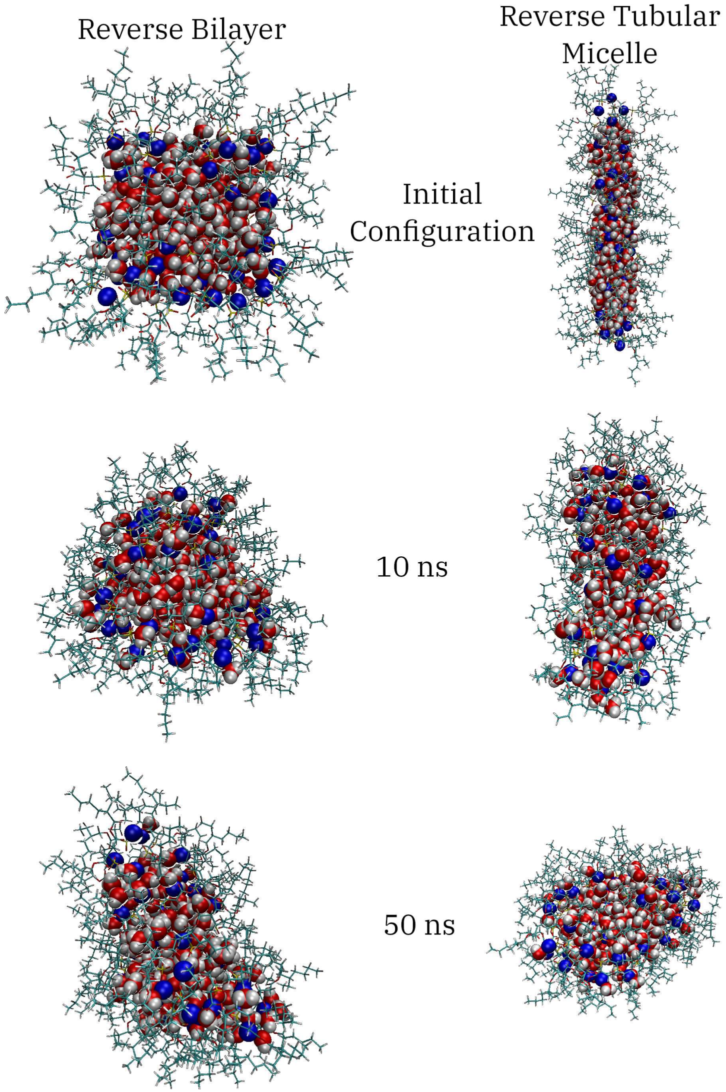

Figure 2.2: The starting configuration, configuration after 10 ns, and after 50 ns of equilibration for both the “reverse bilayer” and “reverse tubular micelle” starting configurations.

the V-rescale thermostat[61] and Berendsen barostat[58] with a 1 fs step size for 15 ns with coordinates saved every ps.

The goal was to copy experimental conditions as closely as possible. The largest consideration is that simulations can only model integer numbers of molecules, so I chose a single data point to replicate based on the one that could be replicated most closely in simulation with whole molecules. However, from experiment alone, it is unclear if Tanaka, *et al.* measured an AOT monomer, dimer, *etc*. Therefore, I first simulated a series with 1, 2, and 3 AOT molecules, including the sodium counterion, in 4717, 9434 and 14151 molecules of cyclohexane, respectively, for a mole fraction of 2.1195×10^{-4}, compared to the experimentally measured mole fraction of 2.120×10^{-4}[89]. All of these simulations used the CHARMM force field. Figure 2.3a shows the results of these simulations. Based on these results, it appears as though experiment was likely observing AOT dimers because the dipole moment of both the monomer and trimer were significantly different from the experimentally measured dipole moment. Then, another series of simulations was performed using the dimer configuration in 9434 cylcohexane molecules for each AOT force field simulated in this work, *e.g.* CHARMM, OPLS-Std, OPLS-RESP, and OPLS-CM5, shown in Figure 2.3b. Note that the CHARMM-4P simulation is only different from CHARMM because of the water model and there is no water in this system making it redundant here. Unsurprisingly, the two simulations whose partial charges were based specifically on AOT, that is the OPLS-RESP and OPLS-CM5 simulations, are slightly better than the other two force fields, however the difference is not very large and all force fields appear to reproduce the experimentally observed dipole moment of AOT well. It is not immediately clear how the dipole moment relates to the accuracy of the reverse micelle as a whole, but this is a topic that I investigate more fully in Chapter 11.

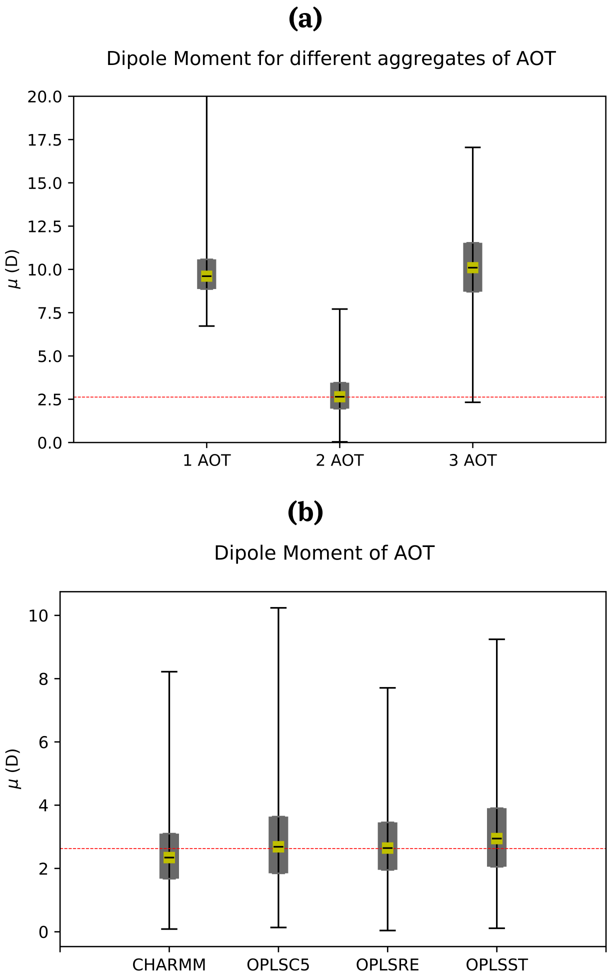

Figure 2.3: (a) Dipole moments of AOT in cyclohexane at a mole fraction of 2.1195×10^{-4} for 1, 2, and 3 AOT molecules. (b) Dipole moments of 2 AOT in 9434 cyclohexane for each force field for AOT used in this work. The black line on yellow indicates the median dipole moment measured over the trajectory, gray box indicates the interquartile range and whiskers indicate the full extent of the data. The red dashed line represents the experimentally measured dipole moment measured in Ref 89.

Chapter 3

A Brief Overview of Shape Metrics

Portions of the information in this chapter have been published in Refs. 1–3. Specific author contributions are provided in Appendix A.

In studying and modeling a shape that does not fit into the typical, regular geometric shapes, *e.g.* a sphere, we need to develop not only a new understanding of the shape itself but also a develop the metrics that will be used to gain that understanding. Chemistry has a long history of studying similar concepts to shape: from determining benzene's structure[90–92] to crystallography[93], including hallmark instances like determining the structure of DNA[94] and penicillin[95], to the larger field of protein structure determination and its many techniques[96–98], to the development of the modern understanding of symmetry and group theory[99]. However, the structure of amorphous and changeable shapes is a new area within this broader field. While a protein may have a generally amorphous shape, it still has a clear and well-defined shape measurable with techniques like crystallography; on the other hand, a soft material like a reverse micelle lacks both a well-defined shape and a consistent structure, instead changing from moment to moment and precluding the usual techniques.

In this thesis, I have developed a series of metrics that I use to analyze the shape of AOT reverse micelles, but because these are entirely new metrics in chemistry being used to study an entirely new problem, it is useful to take a moment and consider how these metrics were settled upon and how they fit together. The metrics I use are by no means singular or the only options available, nor are they perfect. Future work in this area is thus greatly facilitated by understanding why I have done as I did to determine the strengths and weaknesses of my approach and to provide a framework for extending the work along new avenues, which is the purpose of this chapter.

The problem with amorphous shapes is that they are unfathomably numerous. The more typical geometric shapes to which we are accustomed are really a special case of all possible shapes, and “amorphous” is the term we give to the remainder of shapes. To illustrate the scale of this issue, consider ellipsoids, which will feature prominently in this work. An ellipsoid’s shape is completely determined with three parameters that are known as the semiaxes of the shape and given the variables a, b, and c and by convention ordered so that $a \geq b \geq c$. If one normalizes the semiaxes to ignore the effects of size by setting $a = 1$, they obtain every possible non-similar shape of an ellipsoid. However, this still leaves two parameters that may vary continuously, $0 < \{b, c\} \leq 1$. This is an infinite set of potential shapes. In fact, it is an uncountably infinite set of shapes; and yet all of these shapes are still ellipsoids. The scale of amorphous shapes becomes clear when one considers that there are many, potentially infinite, different archetypal shapes like the ellipsoid which can each create infinite variations of that archetypal shape. This process could then be repeated *ad nauseum* for different topological groups, and each of these shapes would be considered amorphous, and all together still only represent the small fraction of amorphous shapes which can be reduced to some archetypal form.

On the other hand, it’s worth taking a look at the tools used to measure things in the most abstract and fundamental sense. In the broadest sense, the goal of a metric is to create a vector space that allows one to differentiate between different instances of whatever one is measuring. In the most common case, we measure a single value, such as measuring the amount of lead in a soil or water sample. This creates a 1D vector space and allows one to distinguish between all samples with different amounts of lead in the sample. But even in this simple case, the metrics are not truly 1D, because if lead content was the only metric, then one could not differentiate between two samples that had identical amounts of lead. Practically speaking there are almost always other metrics involved, even if they are as simple as numbering the samples, or recording the time and place the sample was collected, *etc*. Which is to say that the vector space defining the system is almost always expanded to more than one dimension to differentiate between samples, even when we don't realize it.

Ultimately, one would like to have a unique identifier of shape, but this is also the primary challenge in designing metrics to measure an amorphous shape. If we are to understand what the shape of AOT reverse micelles actually are and how they change from moment to moment, then the measured value of the metrics I use need to change as the shape changes. However, the sheer depth and variety of possible shapes that fall under the umbrella of "amorphous" makes it exceptionally difficult to determine how to set up a system that uniquely identifies the shape. Luckily, practical considerations provide some much needed leeway. First, AOT reverse micelles are expected to be topological balls the vast majority of the time, based on past works and their experience[1,3,36–38,40–43]. Even in the rare case that the topology changes, it should remain relatively simple such as a torus. A good example of this sort of deviation from the norm is observed in the work of Vasquez, *et al.*[39], but the majority of images for AOT reverse micelles reported in the literature illustrate topological balls[1,3,36–38,40–43]. And so I can reasonably assume that the shape should be a topological ball when designing the metrics, which limits the possible shapes significantly and makes the situation far more tractable. The second consideration is that molecules follow a continuous path. Small particles, such as a proton, may exhibit quantum tunneling but this is effectively impossible for whole molecules and these simulations are entirely classical in nature anyway. Therefore, the shape must smoothly change from one moment to the next. It seems highly unlikely that two shapes that are indistinguishable from one another would be so similar that they could be smoothly changed from one into the next with no changes in the metrics observed in between. Therefore, even if the metrics are imperfect and it is possible for two different shapes to give identical values for the metrics I choose, they are almost certainly separated in time. That should be good enough for the purposes of this work since it allows characterization of shape and measurement of the dynamics, even if the shapes are not completely unique.

A key part of the goal of a unique identifier is that the metrics be orthogonal to one another. This is a requirement for any basis of a vector space, such as the $\hat{x}$, $\hat{y}$ and $\hat{z}$ unit vectors that describe 3D space. It is this property that allows the basis to be used to uniquely describe every point in the vector space. This is somewhat challenging to determine for a shape metric. It is easy to prove mathematically that two vectors are orthogonal, but there is no similar procedure for determining if one measure of shape is completely independent of another measure of shape.

Finally, it is important that the metrics are not only sufficiently descriptive and orthogonal, but also that they are meaningful. These may seem like obvious requirements, but they are crucial requirements. For example, it is possible to sum a series of weighted spherical harmonics to converge on any arbitrary shape, provided that the shape is star shaped, meaning that it is a topological ball and that any ray from the geometric center will intersect the surface only once[100,101]. Based on literature experience, these sums require several thousands of terms to properly converge to the real shape. This method has been used to model small sand particle's shapes. AOT reverse micelles are not solids, but MD simulation allows us to view instants in time with complete knowledge of all atoms positions, theoretically enabling this analysis to be used on AOT reverse micelles. This series of spherical harmonics method is a truly unique identifier— at least in the limit of an infinite sum of terms— with each value guaranteed to be completely orthogonal to every other term by virtue of the properties of spherical harmonics. However, I do not believe that these spherical harmonics provide a useful tool for analyzing the shape. The result is a vector several thousand terms long which acts much like a serial code identifying each shape. But just like individual numbers hold no significant meaning within a phone number, these numbers hold very little information about the shape itself. The changes can be tracked precisely, but it is virtually impossible to truly understand what these changes represent. Therefore, it is also critical that the metrics I use hold intrinsic meaning. Additionally, while it is not the main reason for not using a series of spherical harmonics, it is worth noting that the restriction of a star-shaped object is unlikely to be useful for AOT reverse micelles which have been observed to fold.

With these considerations in mind, I have designed a set of metrics of shape to use in studying the shape of AOT reverse micelles. Those are the coordinate-pair eccentricity (CPE), convexity and the curvature distribution. In coarse terms, the CPE measures the distribution of mass, the convexity the bending, folding and dimpling of the shape, and the curvature distribution measures the curvature of the surface. They were all chosen on the assumption that the shape would be a topological ball. Technically, all of the metrics will produce a number for any topology, but the usefulness of that number is significantly reduced if the shape is not a topological ball. The metrics were also designed to be as orthogonal as possible. There is no formal or rigorous way to test that the metrics are orthogonal as far as I am aware, but I offer the following heuristic arguments. It is possible to change the CPE without changing the convexity, most easily by creating two different ellipsoids; ellipsoids are convex so convexity remains unchanged while the CPE changes by definition. Conversely, it is possible to change the convexity without altering the CPE, simply by adding golf ball-style divots symmetrically over the surface, with the pattern aligned with the moments of inertia. Therefore, it seems likely that CPE and convexity are orthogonal to each other and measure independent properties of the shape. The orthogonality between CPE and the curvature distribution is demonstrated in the same way as convexity. For convexity and the curvature distribution, one should be able to alter the curvature distribution by changing the shape. For example, if the “original” shape is a horseshoe-type shape with some value of convexity, a barbell shape could also be made to have the same convexity value but the curvature distribution of this shape should be different.

Chapter 4

Coordinate-Pair Eccentricity (CPE)

Portions of the information in this chapter have been published in Refs. 1 and 3. Specific author contributions are provided in Appendix A.

4.1 Eccentricity and an Introduction to CPE

Coordinate-Pair Eccentricity (CPE), is an extension of eccentricity itself. Eccentricity has an incredibly long history, coming from the study of conic sections[102], and being published by Kepler for the study of the orbits of heavenly bodies in 1609[103]. Eccentricity is a measure of how elliptical an ellipse is, obtained by comparing the semiminor and semimajor axes of an ellipse. Let a and b represent the semimajor and semiminor axis respectively, then the eccentricity is defined by (4.1).

$$e = \sqrt{1 - \frac{b^2}{a^2}} \tag{4.1}$$

Note that the fact that a is considered the semimajor semiaxis implies that $a \geq b$, which means that $0 \leq e \leq 1$, reaching a minimum when the semimajor and semiminor axes are exactly equal— they are both equal to the radius and the ellipse is a circle— and eccentricity reaches a maximum as either $\lim_{b \to 0} e$ or equivalently as $\lim_{a \to \infty} e$.

Eccentricity is a commonly used metric for analyzing the shape of materials and is often interpreted as being a measure of the sphericity of an object, or how spherical an object is[36,40,41]. This is done using the moments of inertia for a simulated object, in this case a simulated reverse micelle. The magnitude of the principle moments of inertia can be related to the semiaxes of an ellipsoid of constant density that shares the same moments of inertia, where an ellipsoid is the 3D analogue of an ellipse. In other words, it is possible to find a representative ellipsoid that rotates in the same way as the object being studied. Being based on the moments of inertia and the rotation of the object, this method works for any arbitrary shape of any kind or topology, so long as it is 3-dimensional. From this ellipsoid, a "semimajor" and "semiminor" axis can be extracted from the three semiaxes of an ellipsoid and used to calculate the eccentricity from (4.1).

However, the use of classical eccentricity for reverse micelles contains a key error: the shapes that are being measured are 3-dimensional objects while eccentricity is designed for analyzing a 2-dimensional ellipse. This is showcased by the fact that an ellipse has two descriptors— the semimajor and semiminor axes— and similarly, that eccentricity takes two arguments. By contrast, an ellipsoid has three semiaxes. This has a profound impact on the efficacy and interpretation of the parameter. 2D eccentricity only needs to differentiate between circular and not circular. For any given, eccentric ellipse, switching the values of the semimajor and semiminor axes is equivalent to a 90° rotation, making them identical and equivalent shapes. On the other hand, a 3D ellipsoid has three possible structures that need to be differentiated. An ellipsoid can be spherical or not, in much the same way that an ellipse can be circular or not. However, when an ellipsoid is not spherical, it can be either prolate or oblate ellipsoidal. And so there are three cases to distinguish between and a single parameter cannot distinguish between more than two cases, making it insufficient for fully interpreting the shape of a 3D object.

In fact, there are several parameters similar to eccentricity exist, all based in various ways on the moments of inertia. And some of these other parameters use two equations to fully differentiate between the possible 3D shapes encountered[37,104]. In general, any measure classifying a shape into approximately spherical, oblate, or prolate ellipsoidal must be composed of two equations. This conclusion can be found from a degrees of freedom argument but a simple graphical argument is easier. A 1D number line can only differentiate between two possibilities, *e.g.* to the left or to the right. To differentiate between 3 possibilities, one needs a second dimension. CPE addresses this need for an additional parameter quite simply. While eccentricity compares two semiaxes, CPE simply uses two copies of the eccentricity equation to compare all three semiaxes of an ellipsoid, as shown in (4.2).

$$\begin{aligned} e_{ab} &= \sqrt{1 - \frac{b^2}{a^2}} \\ e_{ac} &= \sqrt{1 - \frac{c^2}{a^2}} \end{aligned} \tag{4.2}$$

Just like eccentricity, e_{ab} and e_{ac} have a range on the interval $[0, 1)$. For a sphere, $a = b = c$, and therefore $e_{ab} = 0$ and $e_{ac} = 0$. for a prolate ellipsoid, $a > b = c$ and so $e_{ab} > 0$ and $e_{ac} > 0$. For an oblate ellipsoid, $a = b > c$ and so $e_{ab} = 0$ and $e_{ac} > 0$. In order to plot these values, I have chosen as a matter of convention to plot e_{ab} on the x-axis and e_{ac} on the y-axis. This means that spheres and near-spherical objects will appear around the origin, prolate ellipsoids and near-prolate ellipsoidal objects will appear along the line $y = x$, and oblate ellipsoids will appear along the y-axis. Notice that none of these appear below the line $y = x$ and there is a good reason for this. A point below the line $y = x$ implies that the x-value is greater than the y-value, or in this case, that $e_{ab} > e_{ac}$. The semiaxis a is common to both of these values and so the only way for this to be true is if $b < c$. However, by convention, the semiaxes were named so that $a \geq b \geq c$. Therefore, by virtue of the conventions commonly used for ellipsoids, it is impossible to ever observe a point below the line $y = x$ in a plot of CPE. In all CPE plots provided in this work, this region is blacked out to remind the reader that this space is forbidden. One could reverse this by defining the semiaxes in the opposite order and adjusting the equations for eccentricity accordingly; the

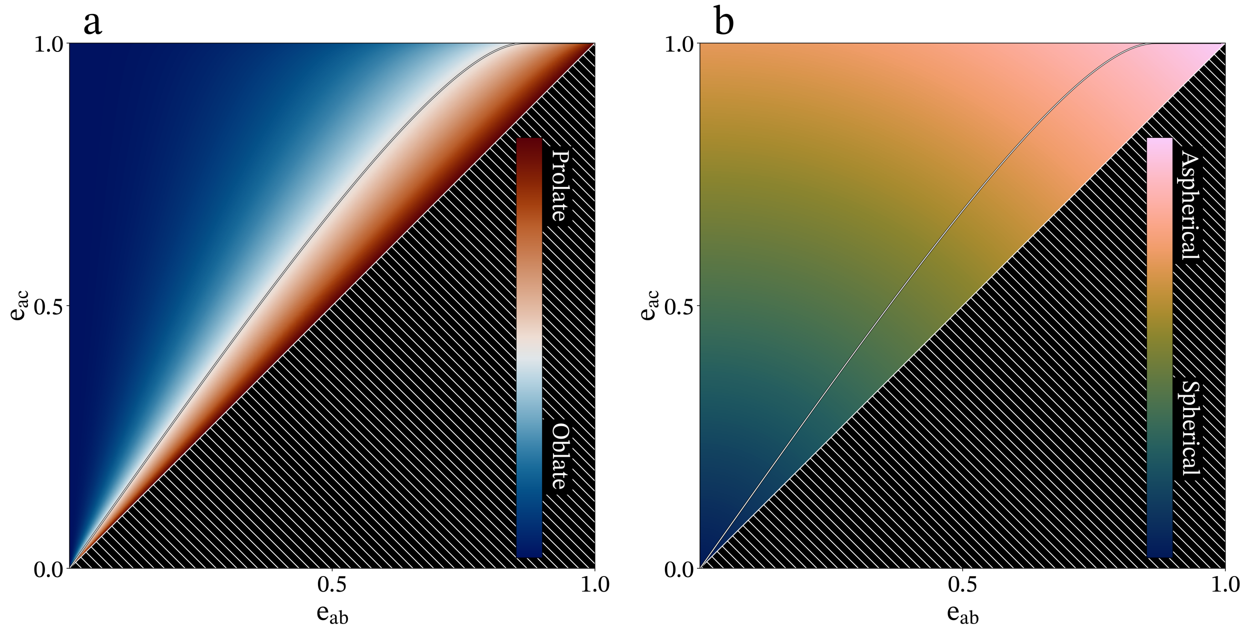

Figure 4.1: Two illustrations of how different shapes appear on CPE plots. a) A CPE plot colored according to the oblate/prolate-ishness of the shape. b) A CPE plot colored according to the asphericity of the shape.

ratio of square of the semiaxes must always be less than one for the equation to be a real function. In this hypothetical case, all points would only appear below the line $y = x$ and a similar blacked-out triangle would appear in the plot, only now above the line $y = x$, so there is no reason not to use the more commonly-held conventions. An example of how CPE relates to both oblate and prolate sphapes as well as sphericity and asphericity is provided in Figure 4.1.

Figure 4.1 illustrates some of the weaknesses of using eccentricity as opposed to a two-parameter metric like CPE. The asphericity is related to the distance from the origin. However, by using only one of the two equations for CPE, as has been done in past literature[36,40,41], a drop in the value measured could indicate either the shape becoming more spherical, or the shape becoming more prolate, or some combination of the two. It is impossible to differentiate between these possibilities, which implies that past works were most likely somewhat inaccurate in their analysis of shape.

Although there are other metrics that do essentially the same thing as CPE and have some precedent in the literature[37,104], I will continue to use CPE throughout this work. There are several reasons for this. First, while other metrics appear in literature, they are hardly popular enough to constitute a consensus with only one instance known to me for each metric. Then, because all of these metrics are based on the principal moments of inertia, they should be effectively equivalent and simply map the eccentricity codomain into different forms. In fact, I have been able to show that CPE is exactly equivalent to one of these methods, the "Eta parameters" from the work of Chowdhary, *et al.*[37] (name created by me to differentiate it from other parameters), which I believe is sufficient to illustrate this point. This is demonstrated in more detail in Appendix F. Therefore, the choice of the exact metric is mostly cosmetic. Several works have studied the (2D) eccentricity of AOT reverse micelles, establishing some precedent in the field to continue in this tradition and use CPE[36,38,40,41]. CPE is also a convenient function to use. The range in both dimensions is finite, while other metrics tend to have at least one parameter which ranges to infinity. CPE is also symmetric, with both dimensions behaving exactly identically, making interpretation convenient and easy. This symmetry was also key to being able to develop my model and proof presented in Appendix B. Lastly, CPE is based on shape from the outset. Since it is based on the semiaxes derived from the principal moments of inertia rather than the moments of inertia themselves, it provides a simple and straightforward method for interpreting the results not available with the other metrics.

4.2 Examining a Continuous Measure of Oblate and Prolate Shapes

A perfectly prolate ellipsoid is defined such that $a > b = c$ while a perfectly oblate ellipsoid is defined such that $a = b > c$. However, these are typically defined as set geometric shapes. That is, one creates a shape by first assuming that it is oblate and then creating the resulting surface, making it a binary affair. A shape is either oblate, so that $a > b = c$ precisely, or it is not oblate. On the other hand, the entire point of CPE and metrics like it is to classify intermediate and amorphous shapes as closer to being one thing or another: a continuous metric. So it is important to consider how one works with and even thinks and talks about a continuous definition of oblate and prolate.

Take a simple example case: say that I start with a perfectly oblate ellipsoid with semiaxes given by $a = 10$, $b = 10$, $c = 1$, in appropriate units, and then I change semiaxes b by some small amount $\zeta \ll 1$ so that the new ellipsoid has semiaxes $a = 10$, $b = 10 - \zeta \approx 10$, $c = 1$. In this case, it is only natural to to think that this new ellipsoid is almost, but not perfecttly, oblate. Following this line of reasoning leads us to a natural definition of what it means to be oblate or prolate on a continuous scale by looking at how the semiaxis b compares to a and c.

$$a - b > b - c \qquad \longrightarrow \qquad \text{prolate-ish} \tag{4.3}$$

$$a - b < b - c \qquad \longrightarrow \qquad \text{oblate-ish} \tag{4.4}$$

If $a - b = b - c$, because this is neither one region or the other, then this must represent the division between oblate- and prolate-ish[3] ellipsoids. Notice that this definition of a division between oblate and prolate runs directly through the origin and therefore includes a sphere. In this case, $a = b = c$ and therefore $a - b = b - c = 0$.

---

[3] Formally, an oblate ellipsoid is one for which the condition $a = b > c$ is met exactly, with prolate ellipsoids defined similarly. There is not a word I am aware of to describe the situation encountered here, where an ellipsoid is closer to being oblate rather than prolate. Until someone creates a new word which formally matches the situation encountered here and is broadly adopted by the geometry community, I will employ the words oblate-ish and prolate-ish as a practical and easy solution to this problem.

This fits well with the qualities one would expect from a divider between oblate and prolate ellipsoids.

To parameterize this relation into a function, with e_{ac} given as a function of e_{ab}, We begin by noting that $a - b = b - c$ implies that both sides are also equal to some constant n, representing the difference between the semiaxes. We could therefore express the semiaxes by setting b to unity and writing $a = 1 + n$ and $c = 1 - n$. Note that this implies a limit to n. The relationship between semiaxes, $a \geq b \geq c$ means that $0 \geq a - b \geq 1$ and therefore, $0 \geq n \geq 1$. To generalize this a bit further, we introduce a scaling factor d that allows us to express this relationship for ellipsoids of any arbitrary size. If we put this all together, we find that:

$$a - b = b - c \qquad \Longleftrightarrow \qquad \begin{cases} a &= d(1+n) \\ b &= d \\ c &= d(1-n) \end{cases} \tag{4.5}$$

where n is the normalized difference between semiaxes and d is a scaling constant, $d \in \mathbb{R}^{+}$. If n is zero, then the ellipsoid is a perfect sphere, which is neither oblate nor prolate; and if n is one, then the length of semiaxis c is zero, which only makes sense if taken as the limit as $n \to 0$, indicating that the shape is an infinitely thin shape, either a rod or a disk. Note that this definition is fully general and covers all possible sizes of ellipsoids via the scaling constant, d, while also covering all possible asphericity values by varying the value of n. Therefore, we can substitute these generalizations into the equations for CPE to obtain a parametrically defined curve in terms of the new “eccentricity” parameter, n. The values of d cancel out, as is expected because CPE is an intensive property while d is included specifically to account for the fact that semiaxes lengths are extensive.

$$e_{ab}(n) = \sqrt{1 - \frac{1}{(1+n)^2}} \qquad e_{ac}(n) = \sqrt{1 - \frac{(1-n)^2}{(1+n)^2}} \tag{4.6}$$

We can remove the parameter n to obtain a function of the form $e_{ac}(e_{ab})$ (*e.g.* in the form of a common 2D function, $y = f(x)$) by solving $e_{ab}(n)$ for n and then substituting this expression into $e_{ac}(n)$. I skip the algebra for the sake of the reader and arrive at the expression:

$$D_{OP}(e_{ab}) = 2\eta^{-1}\sqrt{\eta - 1} \quad , \quad \eta = \sqrt{\frac{1}{1 - e_{ab}^2}} \tag{4.7}$$

where $D_{OP}(e_{ab})$ represents the "D̲ivider line, O̲blate/P̲rolate as a function of e_{ab}". However, the parametric equation in 4.6 is only defined for $0 < n < 1$ and so there are similar limits on the divider line in equation 4.7. Once again, I omit the algebra for the sake of the reader and obtain the final expression with correct limits.

$$D_{OP}(e_{ab}) = 2\eta^{-1}\sqrt{\eta - 1} \quad , \quad \eta = \sqrt{\frac{1}{1 - e_{ab}^2}} \quad , \quad 0 < e_{ab} < \sqrt{\frac{3}{4}} \tag{4.8}$$

Because this divider line is important to interpreting CPE plots, it has been included in all plots of CPE: Figure 4.1, Figure 4.2, and Figure 4.3.

4.3 The CPE of AOT Reverse Micelles

I measured the CPE of each of my 5 main reverse micelle simulations, each analyzed at each of the 5 surfaces of the reverse micelle. The sheer number of points made any sort of plot involving every time point impractical and unproductive. Instead, I have taken the 2D histogram of the individual values to present a heatmap representation of each simulation and surface. An example is shown in Figure 4.2a. There are 25 plots of this kind in total and comparison is still difficult, so I have further reduced the data down to a mean and interquartile range represented by a cross in Figure 4.2b-f, while the remaining "raw" heatmap plots are provided in Appendix C.

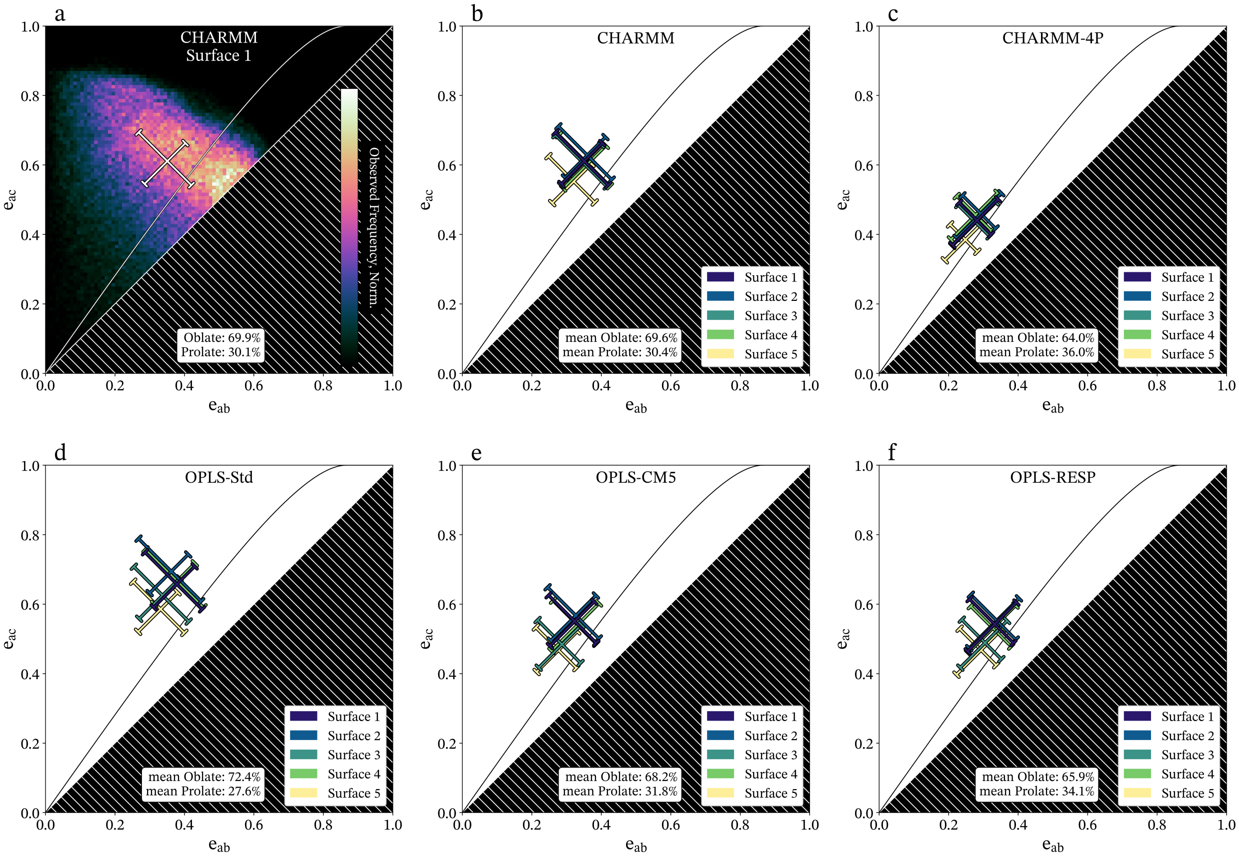

Figure 4.2: (a) The distribution of CPE values observed over the entire trajectory for the CHARMM simulation, 1st surface, as a representative sample. Brighter colors denote a greater number of observations of that value. The cross represents the interquartile range, the cross center represents the median value, and the ends represent the upper and lower quartile in each dimension, rotated with a principal component analysis. (b-f) Summary of the CPE distributions over the entire trajectory for each surface of each simulation as labeled at the top. Here, the proportions of the time the reverse micelle is either oblate/prolate is given as the mean value over all surfaces.

The simplest and most notable observation arising from Figures 4.2b-f is that none of the simulated reverse micelles are truly spherical. Many experiments and models for AOT reverse micelles have assumed AOT reverse micelles are spherical[6,24,32,105,106]. However, the work presented here demonstrates consistently, across many different parameter sets, AOT reverse micelles are significantly aspherical. More specifically, the reverse micelles are typically more oblate than prolate, although there is clearly quite a bit of variation. Given the diverse set of simulations presented here, the observation of aspherical $w_0 = 5$ AOT reverse micelles is highly robust, dramatically increasing the likelihood that experimental AOT reverse micelles are also aspherical at $w_0 = 5$.

To aid in the comparison between different simulations, I plot the average CPE behavior over all surfaces of each simulation together in Figure 4.3. To emphasize the comparison between simulations, so the center of each circle accurately represents the median averaged over all surfaces, but the extent of the circle only approximates the average of the interquartile range over all surfaces (that is, Figure 4.2 demonstrates generally asymmetric distributions while a circle is symmetric representation). Figure 4.3 reveals natural groupings between our simulations. A "generic" group consisting of CHARMM and OPLS-Std, that is also the most highly eccentric group. An "AOT-specific" group including OPLS-CM5 and OPLS-RESP, that has a lower CPE than the generic group and is therefore relatively more spherical, although still eccentric overall. Finally, the CHARMM-4P simulation stands alone as the most spherical of all the simulations. Given that CHARMM was designed for use with TIP3P water,[68] this simulation is unlikely to accurately capture the interaction between the AOT headgroups and water. Although the CHARMM-4P simulation may not represent reality well, it clearly demonstrates that the water/AOT interaction plays an important role in the shape. Based on the magnitude of the difference compared to the differences observed between other simulations, the water/AOT interaction may even be the dominant factor impacting the shape.

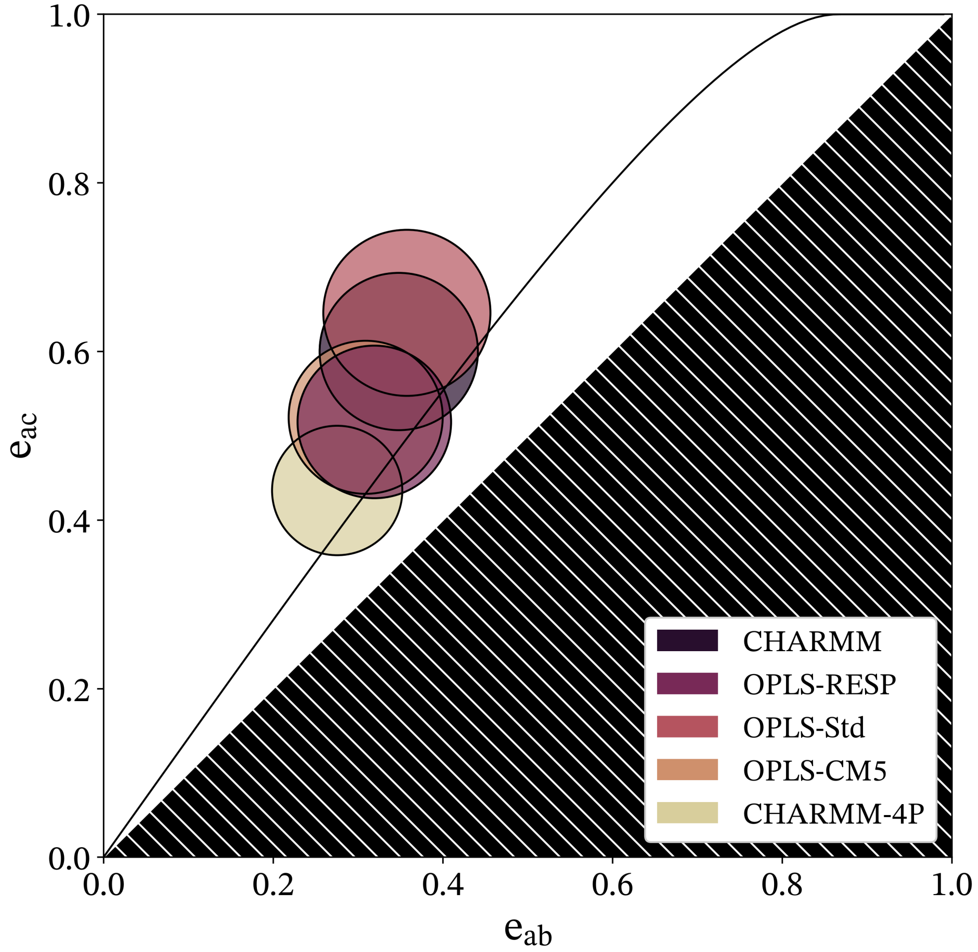

Figure 4.3: A direct comparison of the average behavior of all surfaces for each simulation. The center of each circle represents the mean of the medians of the CPE distribution for each surface while the radius is roughly equal to the median of the interquartile range for each surface.

The similarity between the simulations that use the correct water model for their respective force fields suggests that any simulation with the correct water model produces a reasonably accurate representation of reverse micelles, but it is unexpected that the simulations split into the generic and AOT-specific groups like we observe. The generic group includes CHARMM and OPLS-Std., two force fields developed in different ways for different purposes that we expect would lead to different atomic pairwise interactions. The water/AOT radial distribution functions (RDFs), shown in Chapter 10, indicate that some of the largest differences exist between CHARMM and OPLS-Std. Nevertheless, Figures 4.2 and 4.3 show that these force fields result in roughly the same shapes. Similarly, the AOT-specific group includes OPLS-CM5 and OPLS-RESP, two force fields based on DFT calculations, but whose specific charges are calculated by very different methods resulting in very different partial charges for AOT. And yet, Figures 4.2 and 4.3 show these two force fields lead to very similar shapes, at least in terms of the mass distribution analyzed by CPE, but that are also different from the generic group simulations. We made no changes to the Lennard-Jones parameters of AOT to create the OPLS-CM5 and OPLS-RESP force fields, so it is possible that the lower average CPE for the AOT-specific group is simply the consequence of changing the intermolecular interactions, which are a combination of Lennard-Jones interactions and electrostatic interactions. However, the exact charges on each atom in the CM5 and RESP charge schemes are quite different. If the differences we observe in Figures 4.2 and 4.3 were due to a simple mismatch between the electrostatic and Lennard-Jones parameters resulting in incorrect interaction energies between atom pairs, then we expect the OPLS-CM5 and OPLS-RESP simulations would differ from the generic group while also differing from each other. For example, compared to the sulfonate group charges in the OPLS-Std force field, the CM5 charge scheme has a significantly lower S-O bond dipole while the RESP charge scheme has a slightly larger S-O bond dipole; if differences like these explained the change in CPE, then OPLS-CM5 and OPLS-RESP should move in opposite directions relative to the OPLS-Std simulation. Instead, both the OPLS-CM5 and OPLS-RESP simulations have nearly identical CPE distributions and hence, shapes. An alternative theory posits that the overall AOT charge distribution— *i.e.*, its dipole, quadrupole, and generally the multipolar expansion— has some importance to accurately modeling the behavior of AOT reverse micelles. Currently no experiment can differentiate the comparatively minor differences in CPE between any of the generic and AOT-specific groupings we observe. Experiments struggle to differentiate the much larger differences between the CPE values we observe in simulation and a perfect sphere, so it is impossible to know which simulated shapes are more accurate. Nevertheless, the results presented here demonstrate at least some of the parameters that are important with respect to the shape of AOT reverse micelles.

Chapter 5

Examining How CPE Changes Between Surfaces: Developing and Applying a Model

Portions of the information in this chapter have been published in Refs. 1–3. Specific author contributions are provided in Appendix A.

5.1 Introduction to Changes in CPE Between Surfaces

While it is interesting to know the CPE of the AOT reverse micelles overall, it is also important to study how that CPE changes between the water pool and the AOT-isooctane interface. From the averages shown in Figure 4.2, surface 5 shows a noticeable drop in both dimensions of CPE in every simulation. This indicates that although the outer surface is still not spherical, it is relatively more spherical than the inner shell. This naturally leads to the question: how does the CPE change with size? In a simple toy-model case, if one were to take a simple rectangular prism that is significantly longer than it is tall or wide and then add, for example, 2 cm to all sides, does the CPE change or not? Or in other words, is the change in CPE between surfaces we observe the expected result due to geometry, or is there a chemical reason for this trend?

The more intricate fluctuations in CPE behavior in surfaces 2-4 may be due to our arbitrary choice in surfaces, although it is difficult to say without a broader understanding of how CPE should change throughout the reverse micelle. Other than surfaces 1 and 5, representing the water pool and entire micelle, respectively, the choices for surface 2-4 are entirely arbitrary[4]. There is no prior understanding of how shape is expected to change throughout the reverse micelle, so I chose several surfaces arbitrarily in the hopes of capturing whatever behavior is present. Surfaces 1 and 5 show consistent and well-described behavior across all simulations, in comparison to the arbitrarily chosen surfaces 2-4, suggesting that the arbitrary choice may be to blame. A more confident assessment would require testing an alternate set of surfaces, including different numbers of surfaces, has on the same simulations to test the impact of the choice of surfaces; but this quickly spirals into a large project optimizing both the number of surfaces and locations of those surfaces, which will have to be left to future work. Instead, I focus on developing a better understanding how how CPE should change to better understand if the results we see are anomalous or anticipated.

The issue of how a shell impacts the shape, or more specifically the CPE, goes beyond AOT reverse micelles, too. Core/shell motifs are ubiquitous in chemistry. They are common in nanoparticles of all kinds[107–110], as well as many types of soft materials including AOT reverse micelles[4,6,111,112], biological assemblies like organelles and even whole cells[113], battery materials[114], but also the structure of water and aqueous solutions[115,116], and the dielectric behavior of proteins and nanomaterials[117,118]. In many of these systems, the shape is very important. Oftentimes, there is a structure/function relationship meaning that shape has an impact on the behavior and usefulness of these systems[109,112,119–121]. Nanoparticles' shape, in particular, is of-

---

[4] Dr. Levinger strenuously objects to this characterization but I am exercising my prerogative as sole author of my own dissertation here. However, I believe there is interesting discussion to be had on the topic and so I want to detail the issue here. The disagreement comes from how much value one places on a chemist's intuition and how one defines arbitrary. I chose the exact atoms included in each surface based on some natural break-points in the molecule, *e.g.* a chemist's intuition, and with some attempt made to try to make the distance between surfaces roughly similar although no formal checks were made to guarantee this. Dr. Levinger believes that because I made a conscious choice for the surfaces, they cannot be arbitrary. On the other hand, I believe that I could have chosen any other set of surfaces and created compelling reasons for the choice *post hoc*, and so they must be arbitrary. I leave it to the reader to form their own opinion.

ten a highly prized synthetic target[122–127] that may lead to tunable characteristics by careful control of the shape[126,127]. In the physical sciences, the morphology of a cavity in solution has key effects on the properties of solute-solvent interactions and the behavior of the overall solution[115,116,118,128]. This is especially true for proteins, where the shape is complex and vital to function and also highly dependent on the solvent interactions[119,121].

5.2 Model

In this model, I use an arbitrary shape— *e.g.* a sphere, cylinder, rectangular prism, *etc.*— subject only to the conditions that the shape's (principal) moments of inertia can be computed analytically with a linear equation, and the shape is a topological ball meaning that it does not have a hole like a torus (see Appendix B for more details). Each shape model has its own set of measures. For example, a sphere has a single radius, a cylinder has a radius and a length, and a rectangular prism has a length, a width, and a height. Our model is general and works with all of these examples even though their measures vary. Throughout the rest of the paper we refer to all of these measures collectively as "measures of shape" to generalize the various names typically given to these measures. To study how the shape changes as a function of the shell, I increase all measures of shape by a constant, t, to create a "shell" in our model around the initially chosen shape. Figure B.1 shows a diagram representation of this model for a cylindrical shape. Here, the yellow "hairs" provide a visual representation of the constant thickness, t, added to the cylinder to produce the outer surface (purple). Although the inner and outer surfaces are related cylinders, their shape properties are not guaranteed to remain the same.

A constant increase in the measures of shape, like that shown in Figure B.1, models the typical core/shell motif observed in chemistry well. The shell is constructed by adding a layer of constant thickness, such as the layer of AOT surfactants in my

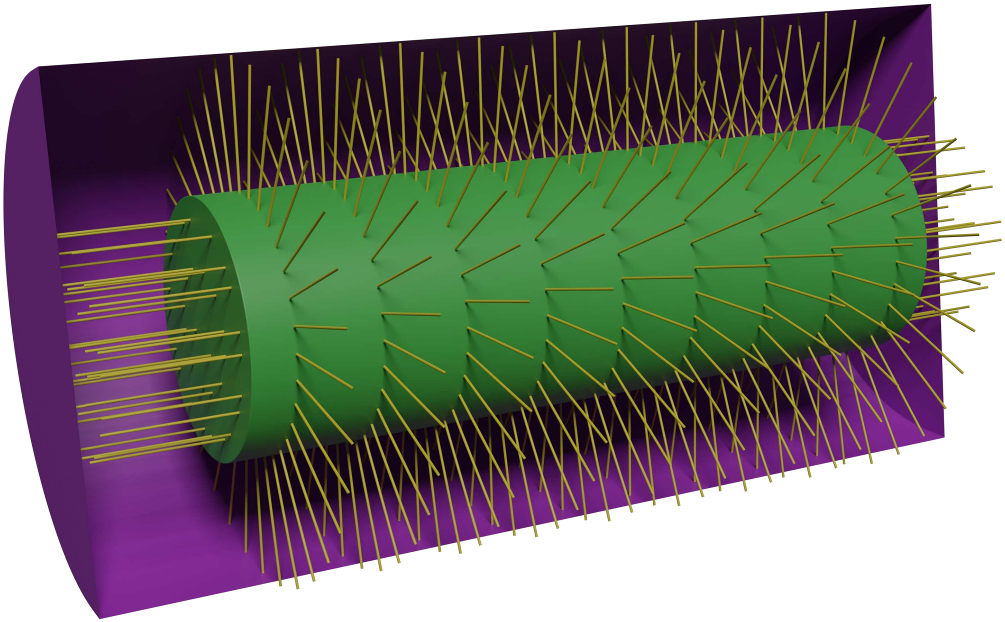

Figure 5.1: (a) The green cylinder represents the core while the purple cylinder represents the shell (shown as a cutaway). The “hairs” shown in yellow represent the additional thickness added to the measures of shape of the core cylinder to create the shell cylinder. This is why the hairs are oriented as shown: extending radial around the length to extend the radius, and normal along the flat ends to extend the length.

reverse micelles or a noble metal shell grown on a nanoparticle. Using this model, I developed a proof determining whether and how the CPE changes with the addition of a constant thickness shell. The full proof is provided in Appendix B, and also published in Ref. 2. The proof first determines whether the shape, as measured by CPE, can remain the same when all measures of shape are increased by a constant thickness. I demonstrate that the shape will change unless the shape is, generally, already perfectly spherical or a perfectly oblate ellipsoid in terms of the shape’s CPE. There is slightly more nuance to our findings, which can be found in Section B.7, however these are extremely niche cases and do not impact the general conclusion that the CPE will always change unless there is already some underlying symmetry in the shape. Considering that these cases are discrete and unique to a specific type of shape (*e.g.* a cylinder versus an ellipsoid), the infinite set of shapes for which these conditions are not met makes it exceedingly likely that the shape’s CPE will always change. The next part of the proof demonstrates that when the CPE changes, it will always fall and fall monotonically, with the shape appearing generally more spherical as the shell becomes larger and thicker.

The results of this model are more intuitive than one might expect and can be demonstrated very easily in the extreme limits with a simple thought experiment. Imagine synthesizing a core/shell type nanoparticle where the core nanoparticle is well-described as an ellipsoid with semiaxes of 1, 5, and 10 nm. The shell-forming reaction is allowed to proceed for far too long, perhaps because a researcher forgot that they had an experiment running, depositing 1 μm of material uniformly on the initial particle. The resulting semiaxes for the core/shell particle will now be 1.001, 1.005, and 1.010 μm. The particle is now spherical for all practical purposes. The initial values become effectively meaningless, and all the outer surface' s measures of shape will become equivalent as the added constant, t, grows to infinity. This argument is a chemistry-specific application of Minkowski sums and demonstrates the general idea of our proof exceptionally well[129]. A formal description of Minkowski sums and their application to this work is provided in Section B.5.

5.3 Introduction to ΔCPE

Rather than relying on general trends shown in Figure 4.2, I present a more formalized representation of how CPE changes, which I will call simple ΔCPE. It is defined as the difference in CPE between the outer and inner surface. We can write CPE as a vector comprised of e_{ab} and e_{ac}, that will be a useful way to think about the math. Then ΔCPE is formally defined by (5.1).

$$\Delta CPE = \langle \Delta e_{ab}, \Delta e_{ac} \rangle = \langle e_{ab,5}, e_{ac,5} \rangle - \langle e_{ab,1}, e_{ac,1} \rangle \tag{5.1}$$

In (5.1), the extra subscripts 1 and 5 are used to indicate the CPE values for surfaces 1 and 5, respectively. In other words, (5.1) illustrates that ΔCPE is simply the vector difference of the CPE of the outer surface and the inner surface, which allows for easy interpretation. In the following, it may be helpful to reference the examples in Figure 4.1. Movement along the CPE plot by the vector ΔCPE, starting from the inner surface's CPE value, will yield the CPE value of the outer surface. This means that if ΔCPE has $\Delta e_{ab} < 0$ and $\Delta e_{ac} < 0$, corresponding to a ΔCPE vector in the 3rd quadrant, we can be certain that the outer surface is relatively more spherical because the CPE has dropped. More likely than not, this also consitutes a slightly more oblate ellipsoid, although the curve of the oblate/prolate divider line complicates this matter somewhat. As another example, consider a ΔCPE vector given by $\langle +, 0 \rangle$. This is a vector along the x-axis, pointing straight to the right. In this case, we could state that the shape has unequivocally become both more prolate and slightly more aspherical. As demonstrated, this formulation allows for easy and convenient interpretation.

5.4 ΔCPE of AOT Reverse Micelles

The ΔCPE plots for each simulation are provided in Figure 5.2. The percent of all simulation frames that appear in each quadrant are written in the corners of each quadrant to give a quantitative measure of the distribution. As predicted by the proof in Appendix B, the vast majority of the time, ΔCPE is in the 3rd quadrant, indicating that the outer surface is relatively more spherical than the inner surface. Figure 5.2f provides a comparison with the crosses representing the median and interquartile range, just like in Figure 4.2. For the most part, all simulations are closely related, although that is to be expected if the majority of the ΔCPE distribution can be explained by geometry. However, it is interesting that among the differences that are there, the simulations do not follow the same patterns as for CPE itself; and that we do not observe a generic grouping, an AOT-specific grouping, with the CHARMM-4P simulation as the black sheep, like we found in Section 4.3. The ΔCPE distributions for the CHARMM and CHARMM-4P simulations are nearly identical, despite having wildly different CPE values; while OPLS-CM5 and OPLS-RESP bracket OPLS-Std, making the OPLS force fields generally distinct from the CHARMM force fields.

These differences between simulations are discussed in more detail in Chapter 11, but I believe the differences in ΔCPE distributions suggest that the majority of the differences observed in Figure 5.2 are the result of the intramolecular parameters of the force field, that is the stretching, bending, and dihedral interactions within a molecule. From the CHARMM simluations, it is clear that the water/AOT interactions have little if any impact on how the CPE changes between surfaces, which makes sense given that surface 1 comprises the water pool while the remaining surfaces comprise the water pool and various portions of AOT. The OPLS force fields all have major differences in the intermolecular parameters, specifically in the partial charges on each atom, creating differences that are much larger in CPE as well as other aspects of shape, as future chapters show. But the differences that are clear and significant between simulations in other metrics are absent in the ΔCPE presented here. This suggests that while the partial charges on atoms plays some role in ΔCPE, it is overall very insignificant. By process of elimination, this leaves only the parameters that are different between the OPLS and CHARMM force field: the intramolecular parameters. This is perhaps not unexpected. If the difference in CPE between surfaces is partially the result of geometry, the other portion is almost certainly a result of the orientation and configuration of AOT itself, which is predominantly governed by how the molecule is allowed to twist and bend.

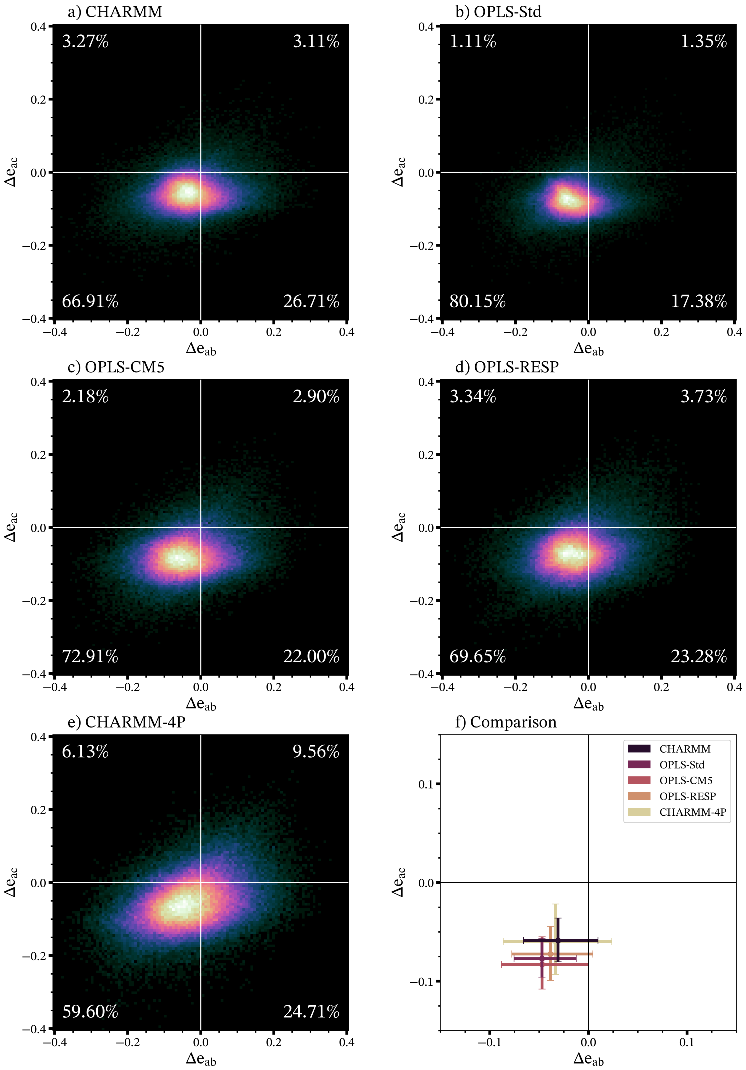

Figure 5.2: a-e) ΔCPE plots for each simulation. The difference distribution is colored so that brighter colors represent values observed more frequently. The percentage of points in each quadrant is provided as text in the respective corners of the plot. f) A comparison of the distributions. The center of the cross represents the median of the distribution and the span of the cross illustrates the interquartile range.

Not all of the ΔCPE population is in the 3^{rd} quadrant as predicted by my model, and there are at least some number of frames in each of the four quadrants. As noted in Section 5.5, the model is simple and will occasionally breakdown for a real chemical system, giving population density to quadrants 1, 2 and 4, which is discussed further in Section 5.5. However, from a purely geometric standpoint, it is just as likely for one type of breakdown to occur as another and so we would predict that the portion the ΔCPE population that is not in the 3rd quadrant should be spread evenly between quadrants 1, 2, and 4. In each simulation, Figure 5.2 demonstrates that there is a clear preference for the outer surface to move down and to the right, or for ΔCPE to be in the 4th quadrant. This unexpected preference for a ΔCPE in the 4th quadrant cannot be explained by my model, nor easily explained by any chemical reason, and so I label this phenomenon the 4th quadrant anomaly and dedicate a section (Section 5.6) to investigating this oddity.

5.5 Breakdown of the Model

My model makes numerous simplifying assumptions to predict behavior that may not be true of real systems. For example, the system must have a completely uniform thickness in its shell, adding precisely equally to each measure of shape. The shape must be one of the limited set of shapes that have analytical, linear equations to describe their moments of inertia that are also topological balls. However, real chemical systems are not perfect. A nanoparticle may be modeled as an ellipsoid to a first approximation but is never perfectly ellipsoidal, if for no other reason than it comprises a crystal lattice with discrete numbers of atoms introducing steps in places rather than a smooth surface. Additionally, while my model is predicated on the addition of constant thickness to all measures of shape, this might not be achieved in practice. In the case of a reverse micelle, the surfactant layer adds thickness to the particle, but to be perfectly equal in all directions, each surfactant molecule must be exactly oriented along a local surface normal, be exactly equally spaced across the surface, and all adopt the exact same conformation so that they are exactly the same length at all points on the surface at all times. This very strict list of conditions is virtually never attainable in real systems.

I have identified three broad classes where the assumptions of our model break down, illustrated in Figure 5.3. In Figure 5.3a, I depict a shape with sharp corners

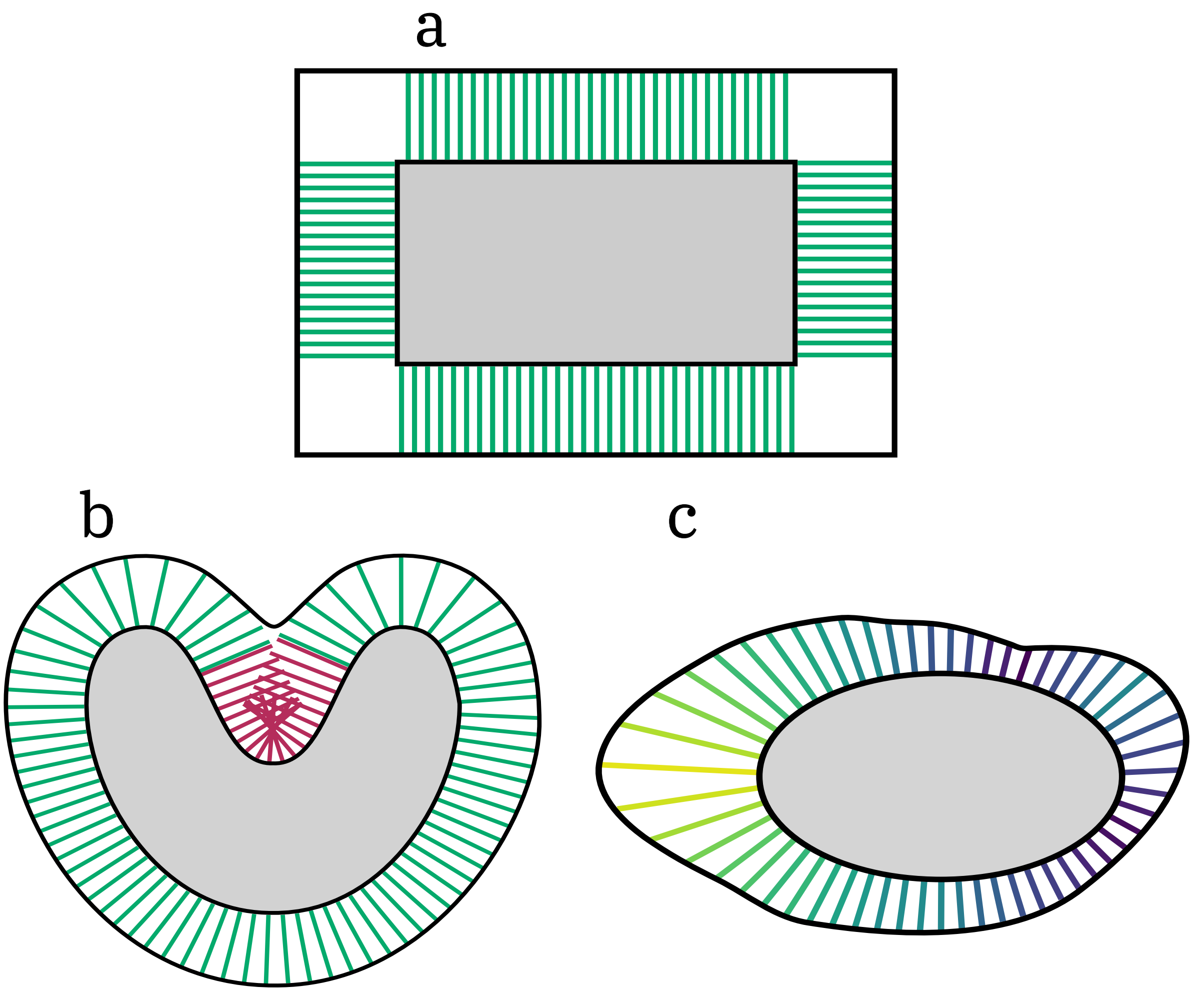

Figure 5.3: Some cartoons illustrating scenarios where our model breaks down. (a) A shape with sharp corners that a molecule will not fill effectively; (b) a deep, sharp "cut" causing the shell to have overlapping volume; (c) a generally non-uniform shell.

that are not populated by the chemical creating the shell. Most likely, this would be encountered as a relative bald spot on an object with some surfactant layer. Note that this situation only works for certain systems. For example, a noble metal shell grown on a metallic, cubic nanoparticle will probably fill the corner easily enough; but surfactants around a cubic nanoparticle might encounter this problem due to the lack of anchor points along the edges. Ultimately, this results in a non-uniform distribution of the shell that violates the construction of my model.

In Figure 5.3b I consider a shape that has a deep cut or crease into the shape, where addition of a constant thickness around the shape results in overlap in the vicinity of the crease, highlighted in red. This situation has been identified in my own simulations and is discussed in Section 6.3. Matter cannot overlap as shown in Figure 5.3b, and so the tail groups of the reverse micelle instead push against each other and “fill in” the crease. In this way, the outer surface is not increased by a constant amount so the assumptions of my model fail. More generally, if the shell overlaps with itself, then the volume can only be filled once and the shell is no longer geometrically similar to the core.

In Figure 5.3c, I illustrate the case where the shell is simply non-uniform for any number of reasons. For example, this may occur when the tail groups of a capping agent adopt varying conformations at distinct points on the surface so that the effective length of the capping agent layer is uneven. For example, if the circular cap of the cylinder in Figure B.1 were chemically distinct from the curved sides, such that a surfactant tended to extend along the circular cap but lie flat along the curved sides, the shell layer would be non-uniform. Alternatively, this situation could happen if the growth of a nanoparticle shell is simply chaotic and uneven.

Although we know that my model does not apply in these situations, this does not automatically mean that the CPE rises instead of falling. In general, I note that the moments of inertia must increase because the shell is necessarily larger than the core, but that is the only restriction. So long as the moments of inertia grow, it is equally probable for the A moment of inertia to grow the most or the least, and so on. Therefore my model is really a special subset of the possible changes in CPE. Within this subset, behavior is predictable and I can guarantee that the CPE falls; but outside of that subset, the CPE could rise, it could fall, it could remain the same, or any combination of the three between the two axes of CPE: e_{ab} and e_{ac}. For example, as drawn, Figure 5.3b shows a “U” -shaped inner surface and a heart-shaped outer surface. If we continued this pattern, the outer surface would eventually become approximately circular and so as drawn, this situation indicates a drop in the

CPE (technically, a drop in the 2D analogue of CPE: eccentricity). On the other hand, Figure 5.3c shows greater “hair” length along the long axis of the shape, while the short axis has shorter hairs, making the outer surface significantly less circular than the inner surface, a situation not unlike a bicelle assembly. Therefore, the situation as drawn would indicate a rise in the CPE. If instead I drew the longer “hairs” along the short axis and the shorter hairs along the long axis, then the CPE would fall, in the short term as the shell effectively compensates for the irregularites of the core, before rising if the pattern were continued even further.

Absent some chemical reason unique to a particular system of interest, it is equally likely for a crease or uneven “hairs” (*e.g.* surfactant molecules, metal shell thickness, *etc.*) to develop on any side of a shape, making it equally likely for these irregularities to cause either a rise or a fall in the CPE. Therefore, the change in CPE for a shape that is not well-described by our model should be expected to be uniformly distributed across all four quadrants and about the origin. This is important to interpreting the results of the difference in CPE between surfaces, examined in Chapter 5.

5.6 A ΔCPE Anomaly

To examine the ΔCPE anomaly, I examine how the CPE of these anomalous frames compare to the full trajectory to investigate whether there is a preference for the anomalous instances of the reverse micelle to have a certain type of shape. In Figure 5.4 I plot the relative probability for a micelle with a given CPE to have ΔCPE in the 4th quadrant, which is calculated from histograms as the difference in the normalized population density of the full simulation minus the normalized population density of only the frames with ΔCPE in the 4th quadrant. Practically, this means that the observation of green on the left of the CPE plots in Figure 5.4 indicates that it is significantly more likely for anomalous reverse micelles to be oblate ellipsoids, and very oblate ellipsoids at that. Conversely, the pink to the right of the plots indicates that this anomalous distribution is much less likely to occur when the reverse micelle is a prolate ellipsoid. This is, of course, somewhat expected. Remember that the ΔCPE may be interpreted as a vector and if it is in the 4th quadrant, then it is a vector moving down and to the right. If the shape is prolate ellipsoidal, there is simply not that much space available to move down and to the right. However, Figure 5.4 generally indicates that there is a clear shape preference to this anomaly with only specific shapes producing this effect, specifically relatively eccentric, highly oblate ellipsoidal shapes, which are "short" and "fat", pancake-like shapes.

I have considered and tested several hypotheses to explain the preference for oblate ellipsoids in frames with ΔCPE in the 4th quadrant. The principal moments of inertia are used to compute CPE and, taken as unit vectors, define a viable basis set for 3D space. If a twist occurs between the principal moments of inertia of surfaces 1 and 5, this could indicate a disconnect between the behavior of the surfaces. To picture this, imagine a prolate ellipsoidal, egg-shaped reverse micelle. A twist would appear as if the yolk of the egg were rotating independently of the orientation of the egg. Such a disconnect would cause our model to break down, implying that this anomaly is not anomalous at all and simply the result of a faulty model. Formally, the matrix transformation representing the rotation between each basis can be found with a change of basis from the first basis set (the MoI of the inner surface, surface 1) to the second basis set (the MoI of the outer surface, surface 5). This is accomplished with equation 5.2.

$$B_2 = B_1 B_2' \tag{5.2}$$

For all variables, in equation 5.2, B is a 3×3 matrix representing the unit MoI vectors in column-vector format, arranged consistently (for example, arranged such

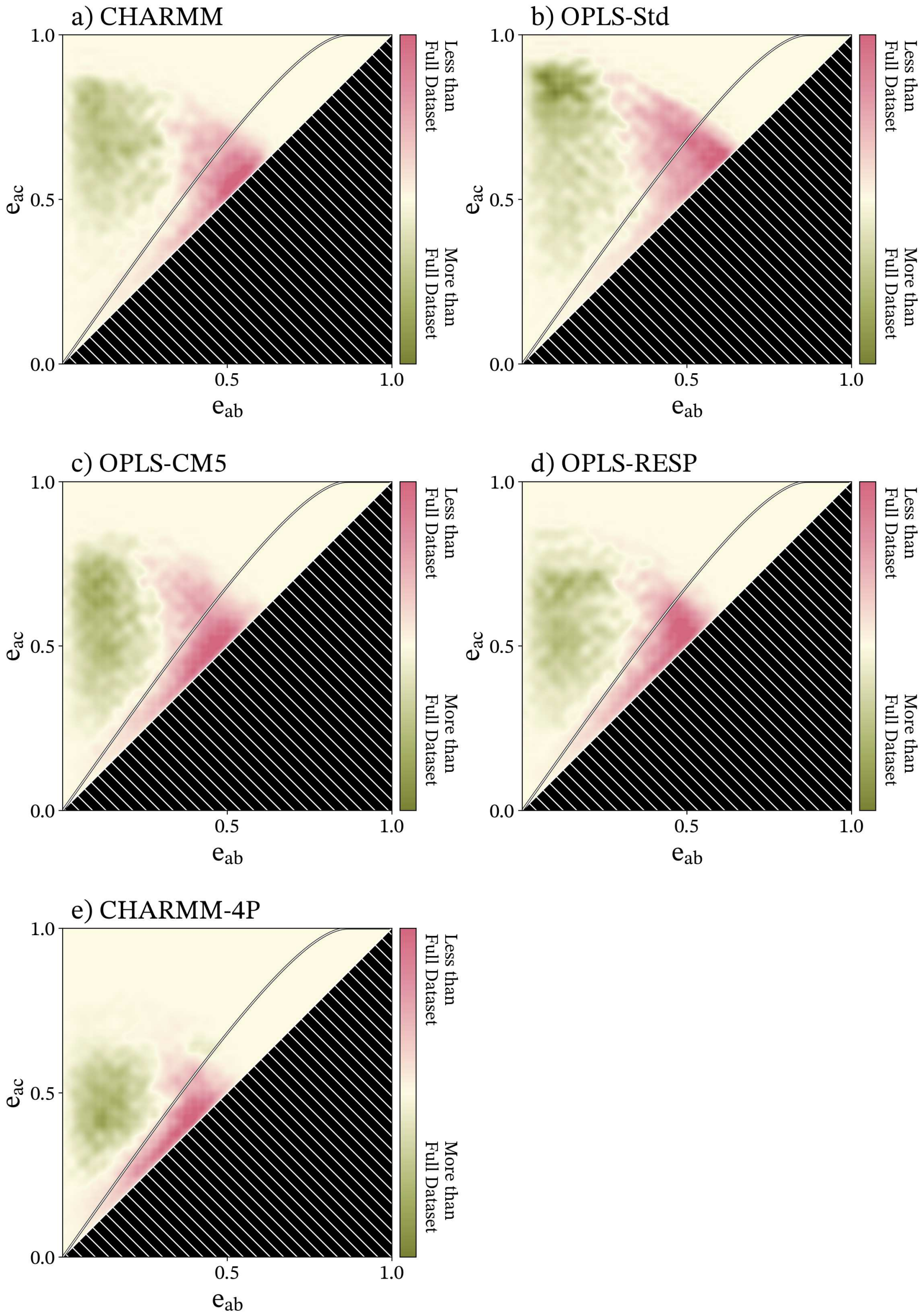

Figure 5.4: Difference in CPE density distribution for surface 1 between the full dataset at all times and only those times where there is anomalous difference in CPE betwen the inner and outer surface. Both the CPE distribution of the full dataset and only those frames where there is an anomalous difference in CPE were normalized so that they could be directly compared by the difference. Green colors indicate that it is abnormally likely to find an anomalous frame at these CPE values relative to the general likelihood of finding these CPE values over the course of the whole trajectory. Pink indicates that it is unlikely to find these CPE values.

that the unit vector associated with the smallest MoI is first, the second largest is second, and the third largest is third). B_2 represents the MoI of the outer surface, B_1 represents the MoI of the inner surface, and B_2' represents the vectors of B_2 over basis B_1 and is equivalent to the transformation matrix between the two bases.

The angle of rotation between the two basis can then be found by analyzing the transformation matrix, B_2'. Assuming that the transformation is purely a rotation, which it will be so long as only unit vectors in the direction of the MoI are used, then the angle of rotation can be found using the relation in equation 5.3.

$$tr(B_2') = 1 + 2\cos(\theta) \tag{5.3}$$

The operation, $tr(X)$, is the trace of matrix X. A histogram of this analysis over all frames in the simulation, for each simulation, is provided in Figure 5.5, and demonstrate that for all simulations, the twist between surfaces is $< 10^\circ$ most of the time[5]. Some amount of twisting is all but guaranteed to occur due to random fluctuations, like a fuzzy ball held in the waves at the ocean, where the fuzz operates as a moving and fluctuating outer surface independent of the immobile ball beneath. I therefore rule out this hypothesis as a way to explain this anomalous difference in CPE. However, this result also proves what I had previously only assumed, obvious as it may be: that the behavior of the inner and outer surfaces are closely related to each other.

---

[5] I have not done statistics to formalize this statement any further. This work was exploratory and qualitative.

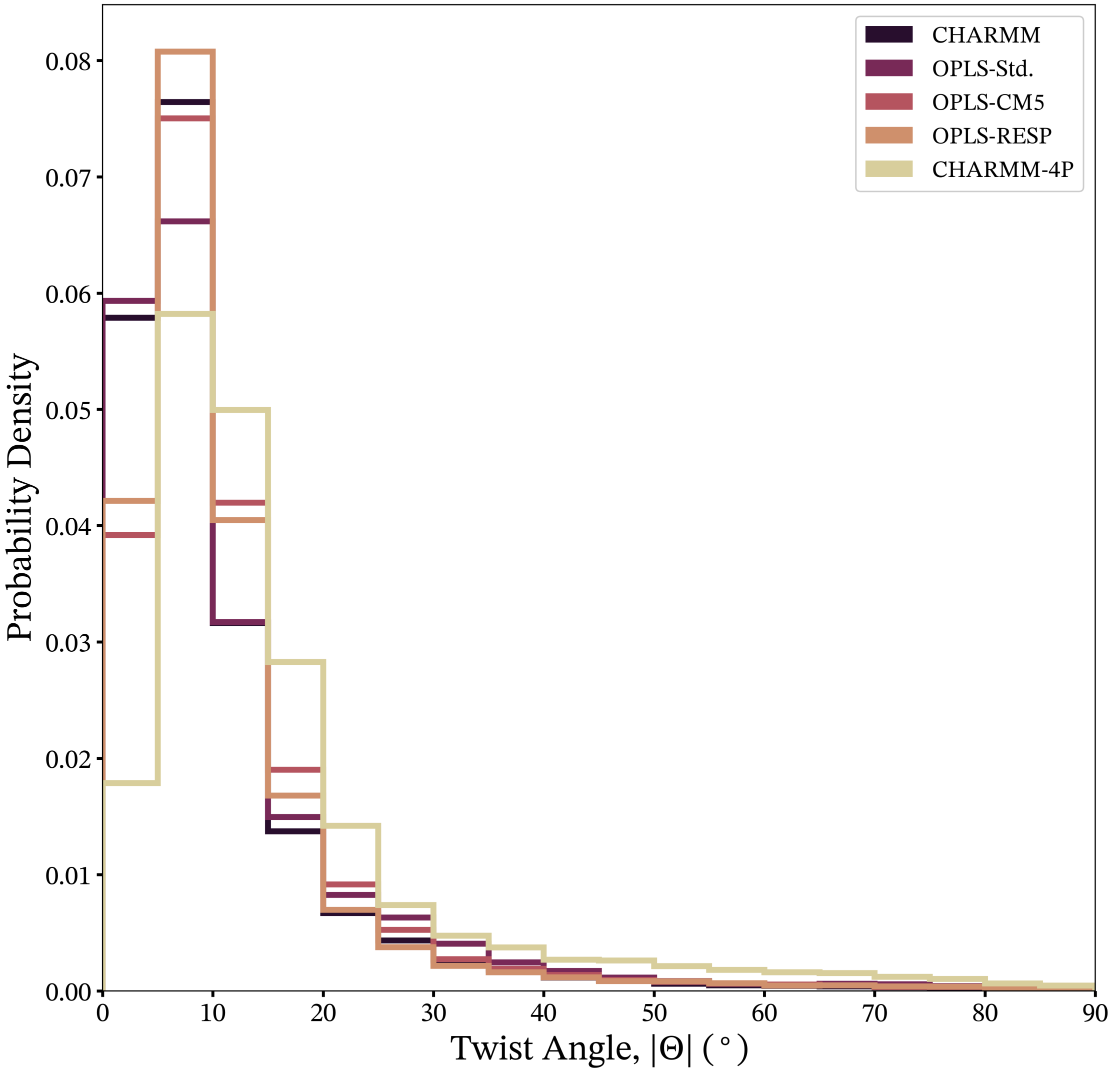

Figure 5.5: The twist angle between the inner and outer surface of the reverse micelle as a histogram over all times simulated. Colors for each simulation are the same as in Figure 4.3.

My next hypothesis is that the reverse micelle attempts to minimize the average mean curvature over the surface. It requires energy to bend an interface, per the surface tension, and so it stands to reason that a shape with regions of exceptionally high curvature might incur a significant energy penalty. Highly eccentric ellipsoids may have regions of much lower curvature, such as the flat(-ish) faces of an oblate ellipsoids, but they also have very highly curved regions along the edges, or at the poles for a prolate ellipsoid. Therefore, the hypothesis is that when the inner water pool is highly oblate ellipsoidal, there is an energy penalty to this conformation that tends to cause the outer surface to be relatively more prolate and spherical to minimize the curvature. A relatively more prolate and spherical outer surface corresponds to ΔCPE in the 4th quadrant and could therefore explain the observations in Figure 5.4. I investigated this possibility by measuring the average (median) of mean curvature of the surface as a function of the CPE, shown in Figure G.1, but found that while the mean curvature is related to the asphericity and size of the shape as expected, there is no minimum of mean curvature between highly oblate and highly prolate shapes, as this hypothesis predicted. Additionally, if this theory were true, we would expect a matching, or at least noticeable, amount of density in the 2nd quartile of the ΔCPE plot to account for extremely prolate ellipsoids having a similar penalty, which we do not see. This does not necessarily mean there is no penalty to having a region of high mean curvature. It could be that the penalty is insignificant relative to thermal energy or that the tail groups are not sufficiently flexible to change as we describe.

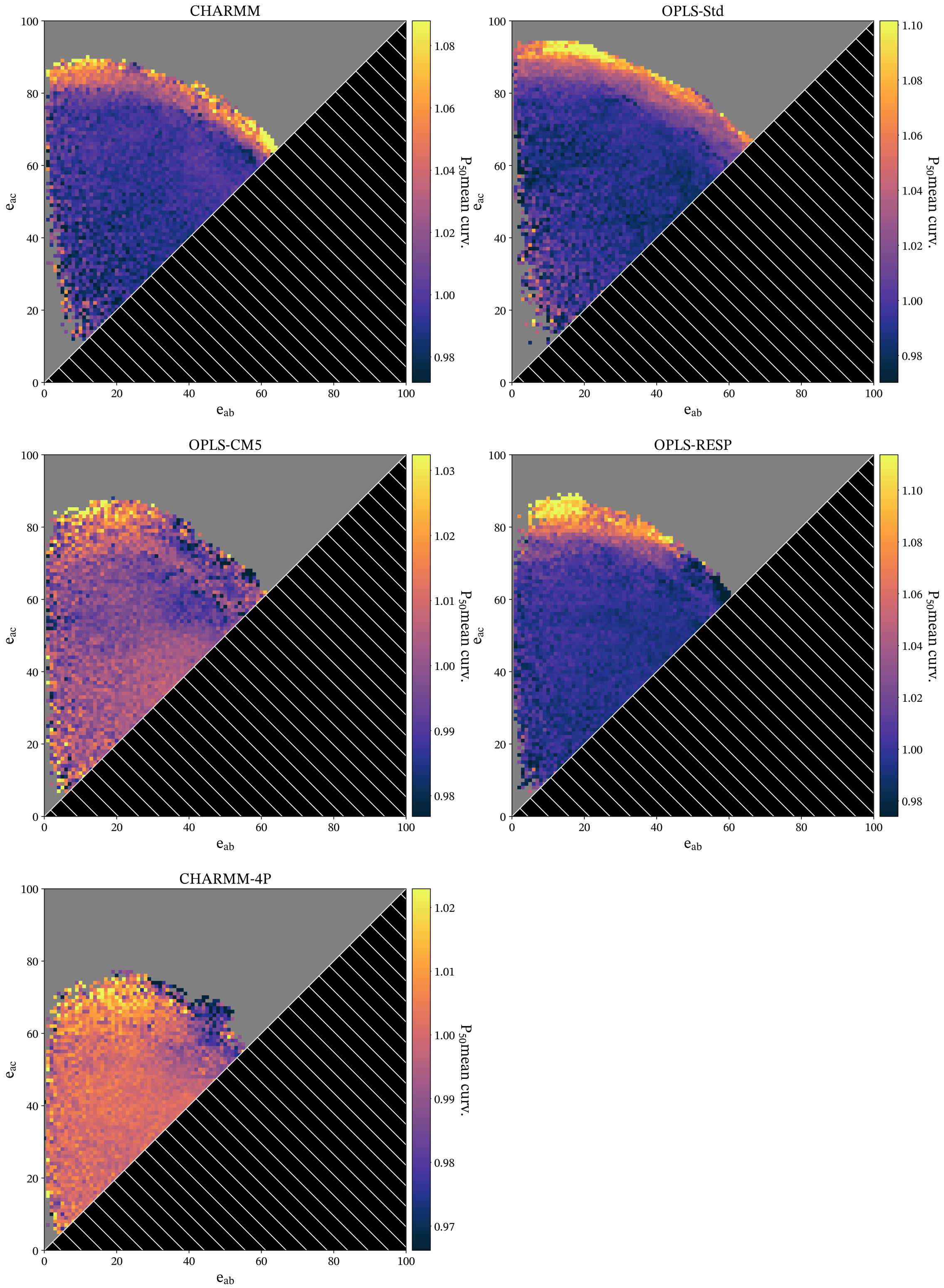

Figure 5.6: Heatmaps of CPE colored according to the median value of mean curvature at the given CPE, averaged over all surfaces, for the simulation as labeled at the top of the plot.

Therefore, I support a more probabilistic view of this phenomenon in which the outer surface adopts a relatively more prolate and spherical shape not because of a specific, shape-related energy penalty, but because it is simply a more likely shape, although that also suggests it is at least slightly more energetically favorable. Note that the median CPE values for all surfaces and all simulations, per Figure 4.2, are very near to the oblate/prolate divider line. The median values are the most likely values to observe, so I believe that at any given moment, the outer surface is simply more likely to look like the median values. This is supported by the fact that while Figure 5.4 shows that it is more likely to be oblate ellipsoidal, this is not an all or nothing, binary situation and all sorts of shapes are observed with ΔCPE values in the anomalous 4th quadrant. For highly prolate ellipsoids, a tendency to move to the most probable shape is a movement down and to the left in CPE, a vector in the 3rd quadrant of ΔCPE, where our model predicts most shapes' ΔCPE to be. Therefore, while the oblate behavior is notable and apparently anomalous, the analogous prolate behavior is likely also present and simply blends in with the expected behavior. This may not be the only possible theory for this behavior, but is plausible and supported by the data I have collected.

Chapter 6

Convexity

Portions of the information in this chapter have been published in Refs. 1 andc 3. Specific author contributions are provided in Appendix A.

6.1 Introduction to Convexity

Before I define convexity, it is useful to understand what mathematics means by convex first, which is not quite the same as a convex (as opposed to concave) mirror or lens. In geometry, convex is a binary state that a shape either has or does not have and is without opposite; so there is no such thing as a concave shape, only a shape that is non-convex. Whether a shape is convex or not is determined with a simple test. Consider every possible line one can draw between any two points on the surface of a shape, either 2D or 3D. If every possible line one can draw is inside of the shape for all portions of the line, then the shape is convex. If at least one of the lines goes outsides of the shape, then the shape is non-convex. For example, every line between any two points on the circle is either a chord or a diameter and every chord or diameter never leaves the circle. Therefore, a circle is convex. For a non-convex example consider a star shape with any number of points. If one draws a line between opposite points, the line lies inside of the star shape; but if one draws lines between adjacent points, then the line is outside of the shape, demonstrating that it is non-convex.

This binary convex/non-convex dichotomy is a useful classifier for many geometric shapes, but its usefulness is limited. Once a shape is non-convex, that is the end and the convex/non-convex classification offers nothing further. But there are a range of shapes that are non-convex and not all of these shapes share the same degree of “non-convex-ness”. For example, an optical lense may be non-convex, but surely it must be more convex than some sort of sea-urchin-type shape with numerous spikes and spaces between.

The purpose of convexity is to convert this binary, Boolean state into a quantitative and continuous range that allows us to characterize not only if an object is convex, but also compare non-convex objects to each other in a numeric way. There are several potential options to measuring the convexity[130], which generally deal with different geometric issues and possibilities that one would need to avoid. However, the basic principles of chemistry mean that geometric possibilities like infinitely long, infinitely thin spikes on a shape are impossible to observe, and so the simple definition I have elected to use, shown in (6.1) is more than sufficient[130].

$$\Xi = \frac{V(S)}{V(CH(S))} \tag{6.1}$$

where Ξ is the variable I have chosen to represent convexity, S represents some arbitrary shape, $CH()$ represents the convex hull of the argument, and $V()$ represents the volume of the argument. The convex hull of a shape is the smallest, convex shape containing the shape of interest. Practically speaking, the convex hull is like a version of the shape where every inward divot is covered by a flat surface, as if with papier-mâché. If the shape is convex according to the binary mathematical definition, then the convex hull and the shape itself are identical and have identical volumes and so $\Xi = 1$. An example illustrating how convexity changes continuously as the divots on a shape grow larger for a 2D analogue is presented in Figure 6.1.

It is important to remember that convexity does not characterize a specific shape, but is rather a property that shapes have. The difference being that there are multiple shapes that could have the same convexity value. For instance, a horseshoe or "U" shaped object could be designed to have the same convexity as a star-shaped object like the one shown in Figure 6.1. The purpose is not to characterize a shape on its

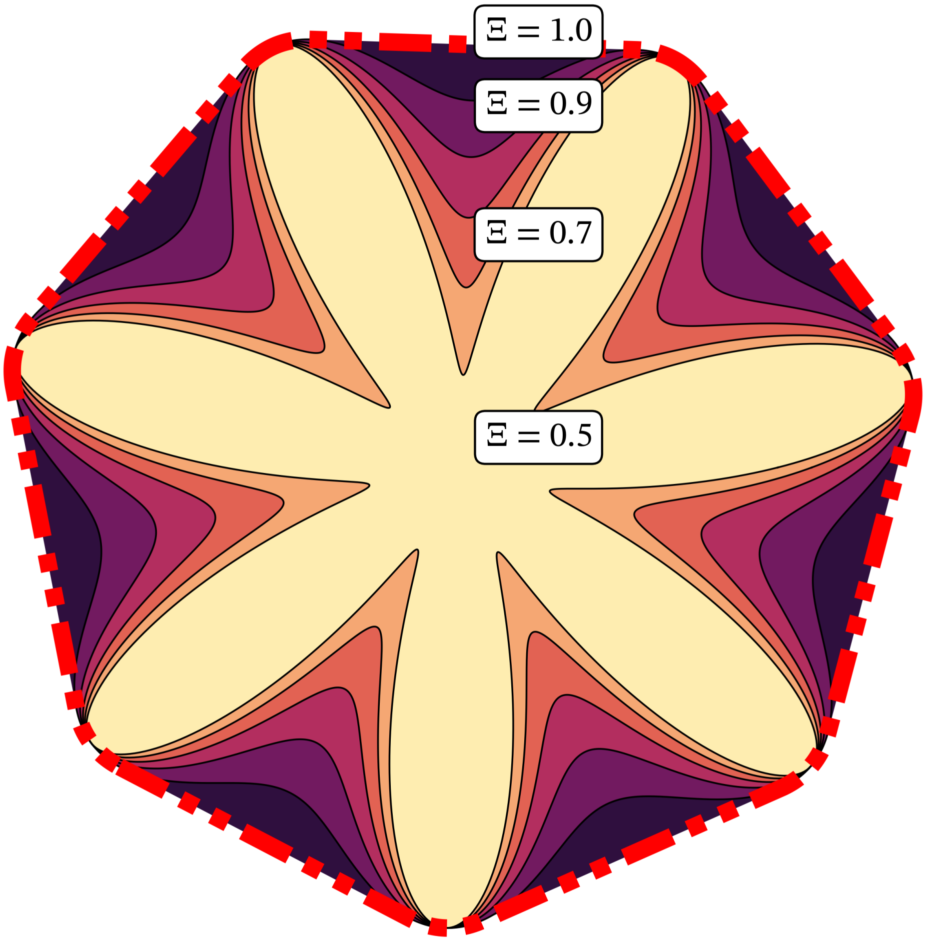

Figure 6.1: A 2D demonstration of how convexity works. Each color represents a different shape, with each lighter color representing a shape with larger divots between the "petals". The shapes were designed so that they all share the same convex hull, which is represented by the red dashed line around the outside of the figure. The convexity of several of the surfaces is provided in the textboxes.

own, though, and a lot of information could be gained by combining it with CPE. A literal ellipsoid is clearly a different shape from some amorphous blob, but CPE can not differentiate those two objects if they rotate the same way. However, the addition of convexity can easily distinguish between many of these cases where the CPE is identical.

6.2 Convexity of AOT Reverse Micelles

The convexity distribution for each AOT reverse micelle simulation at each surface (see Figure 1.1) is shown in Figure 6.2. The distributions on the left and right of each panel represent the same data but in two different ways. The left side illustrates a more natural representation of the distribution as a smoothed probability density distribution, while the right side provides quantitative representation. The time series for each simulation and surface is provided in Appendix C. We can see the same general groupings of simulations as with CPE, where, Figures 6.2a-b show that convexity varies most and has the lowest median values for the generic group simulations. Figures 6.2c-d show the AOT-specific group simulations have slightly more narrow distributions with higher median convexity values, and Figure 6.2e shows that CHARMM-4P has an exceptionally narrow convexity distribution with an exceptionally high median convexity.

Most studies of AOT reverse micelles use eccentricity as the only measure of shape[36,37,40,41], implicitly assuming that the CPE, or generally the eccentricity, is the primary indicator of shape changes, a view that I believe should be revised in the future. Consider the CHARMM-4P simulation, where we observe a highly spherical reverse micelle that is also highly convex. The CHARMM-4P simulation is both the most relatively spherical as well as the most convex reverse micelle I simulated. Presumably, the fluctuations causing the shape to change are roughly similar between simulations and therefore one begins to build a picture where the CHARMM-4P simulation represents a water pool held within a very stiff interface that is not able to deform to the same degree the other simulations are. In this view, it seems like convexity, and not eccentricity/CPE, is the primary indicator of shape, by which I mean that the CPE seems to change because the convexity changes and not vice versa. Convexity is still not a direct measurement of whatever is causing the change in shape, but it is more closely related to changes in the interface and

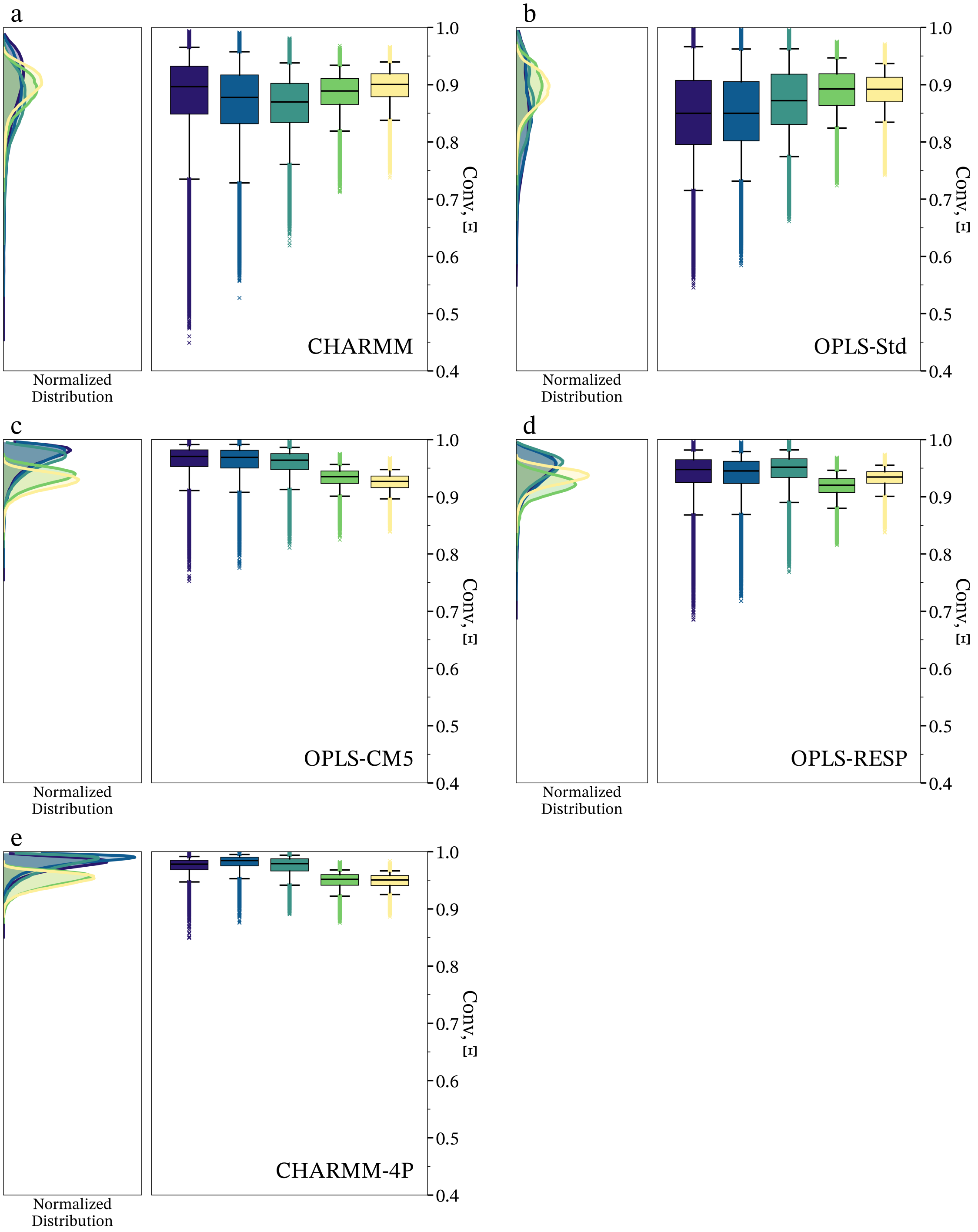

Figure 6.2: (a-e) Convexity distributions for each simulation. The left plots for each simulation show the smoothed histogram of observed convexity values; while the right plots provides a box-and-whisker representation of the convexity distribution, where the center line represents the median, the box represents the interquartile range, and the whiskers encompass 95% of the data, with the remaining 5% considered outliers and plotted as individual points.

therefore a better, single-value indicator of how the reverse micelle is responding to stimuli, if only a single value must be chosen.

From these results, it appears as though the primary difference between the CHARMM-4P simulation and the other simulations in terms of shape is the stiffness of the interface, which is measured by the surface tension. This suggests that there may be a close relationship between the convexity and the surface tension, although I have not been able to formalize this relationship thus far. For simulations, this is an attractive possibility because exact computation of the surface tension for a topological ball is a difficult process. The standard methods for calculating the surface tension from MD simulation either utilize a rectangular box and a flat interface[131], or use a known, generally spherical, geometry and apply a known force to measure the deformation[132]. Neither of these options works well for highly curved and amorphous interfaces like those found in AOT reverse micelles. By contrast, computing the convexity is relatively easy and can be performed quickly for any arbitrary surface. A direct relationship between convexity and surface tension could offer an accessible method for determining the surface tension of any topological ball.

To at least begin to formalize the relationship, I note that the surface tension is essentially the force required to deform a unit length of interface[131,132], while the rate of change in the convexity represents the rate of deformation in the interface. Therefore, one would need to relate the variation in convexity to the variation in the forces experienced by the interface. A mean-field theory formulation seems like it may be useful as it allows one to work in time averages and likely simplifies the calculation of forces, but the missing piece is still the average forces experienced by the interface. On the other hand, this also implies that convexity could be related to a force-normalized surface tension, which may still be useful even without being able to solve for the surface tension directly.

6.3 Convexity Changes Across Surfaces and the Hedgehog Hypothesis

Like CPE, convexity also varies among the five surfaces we define for each simulation. Figure 6.2 shows that the convexity of the outermost surface, surface 5, always has a tighter distribution than the inner surfaces. Both the range of the convexity as observed by both the upper and lower quartiles and the outliers decreases steadily from surface 1 to 5, across all simulations, regardless of the other details of the distribution. Additionally, surface 5 generally has a “Goldilocks” median value, neither extremely high nor extremely low.

To explain these observed differences in convexity between the surfaces, I propose the “Hedgehog Hypothesis”. Let the body of the hedgehog represent the inner surface and the hedgehog’s spikes represent the AOT surfactant molecules, as shown in Figures 6.3a-b. Let us consider two cases, one at each extreme: when the inner surface has low convexity, Figure 6.3a, and when it has high convexity, Figure 6.3b. When the hedgehog has very low convexity, a surfactant normal to the surface would overlap with other surfactant molecules on the opposite side of the divot. Because overlap is unphysical, instead the surfactants displace in the only direction available to them and fill in the volume of the divot resulting in a more minor deformation in the outer surface. The outer surface is still most likely not perfectly convex, but it is comparatively more highly convex than the inner surface. When the hedgehog is highly convex, the surfactants cannot remain closely packed along the entire length of the surfactant, even at the tips, and also cover the entire surface. Geometry dictates that radially arranged spikes around a convex surface must diverge and introduce gaps in the outer surface. Therefore, small divots develop in the outer surface that are not present on the inner surface and the convexity of the outer surface is comparatively lower.

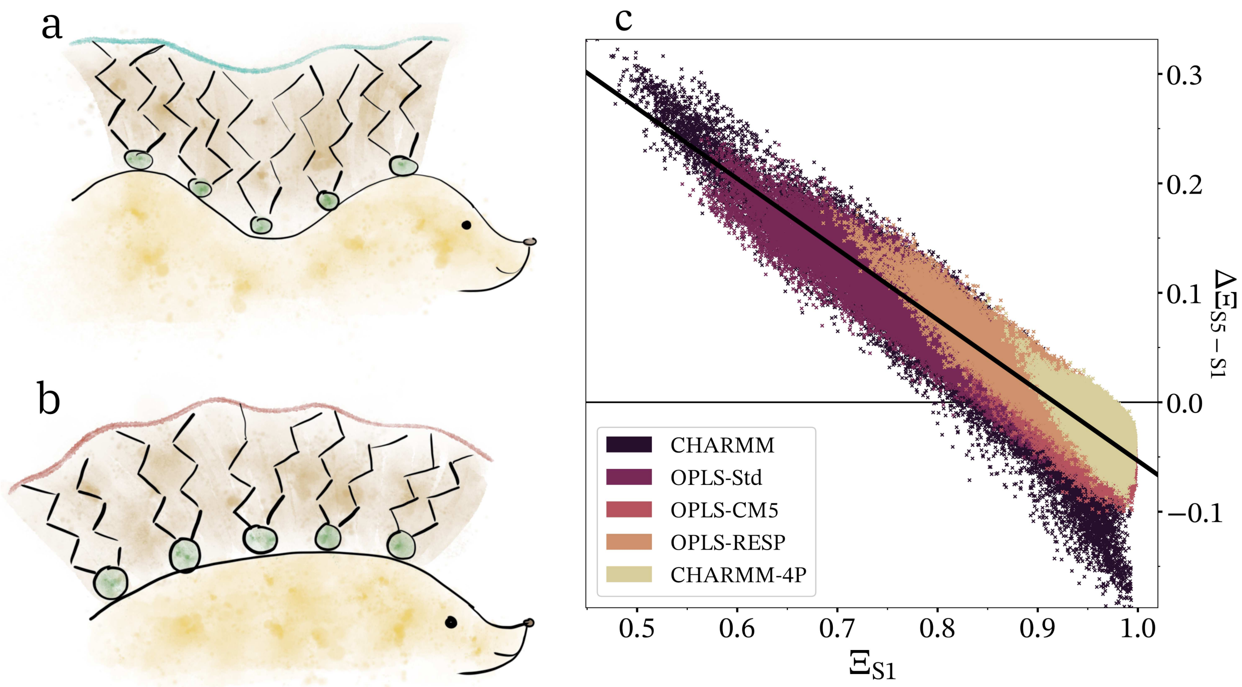

Figure 6.3: (a) Cartoon illustrating the Hedgehog Hypothesis in the low convexity case. (b) Cartoon illustrating the Hedgehog Hypothesis in the high convexity case. (c) Plot of the difference in convexity between surface 5 and surface 1 as a function of the convexity of surface 1. The black line represents the orthogonal distance regression linear fit to all simulations. (d) Cartoon illustrating how one might construct the linear trend observed in subplot c from the endpoints for several different plausible values representing different hypothetical micelles.

Figures 6.3a-b and the hypothesis described so far present a simplified picture and, based on the convexity distributions alone, the Hedgehog Hypothesis is applicable only at the extremes of convexity. We can test the Hedgehog Hypothesis by plotting the difference in convexity between the outer and inner surface against the convexity of the inner surface, shown in Figure 6.3c. We define the difference in convexity between surfaces, $\Delta\Xi$ as the outer surface minus the inner surface so that positive values indicate that the outer surface is more convex than the inner. The convexity difference between surfaces displays a consistent linear trend that is common to all simulations. Referring back to the Hedgehog Hypothesis, we find that the linear trend in Figure 6.3c matches our hypothesis exactly with the outer surface comparatively more convex when the inner surface is non-convex and comparatively less convex when the inner surface is convex. We have fit the distribution of convexity differences to a single line for all simulations. Fitting each simulation individually makes no substantial difference to the fitted line(s), making the difference in convexity between surfaces one of two pieces of data overall and the only shape-related data in which all simulations behave identically.

I discuss a potential explanation for the linear trend found in Figure 6.3c in Section 12.3. I do not have enough data to definitively state how to interpret this trend because I designed my simulations to investigate the shape of AOT reverse micelles and have only incidentally discovered I would need a new set of simulations to investigate this trend. Therefore, my explanation is speculative for now. However I have discovered a problem, have a potential hypothesis and have a method for testing that hypothesis, so it will be discussed in its own section as a possible area of future investigation. Regardless, Figure 6.3c demonstrates that Hedgehog hypothesis is not only true, but a significantly stronger relation than expected.

Chapter 7

Curvature Distribution

The information in this chapter has been published in Ref. 1.

7.1 Introduction to Curvature

As discussed in Chapter 3, the original project goal was to create a set of metrics that were both orthogonal to each other, and could differentiate between every shape we would be likely to observe. The curvature distribution was added as a metric after a simple heuristic observation: both a cube and a sphere share a CPE of $(0, 0)$ and are convex shapes so that $\Xi = 1$. Therefore, with CPE and convexity alone, one cannot differentiate between a cube and a sphere. It seems possible that there would exist similar cases of amorphous shapes that reverse micelles might adopt that share similar CPE and convexity values, and so I also collected information on the curvature distributions in order to theoretically distinguish between these possibilities.

The curvature of a 2D curve (of the form $y = f(x)$) is closely related to the second derivative of the curve and can be most intuitively defined as the inverse of the radius of an osculating circle, which is a circle that closely approximates the curve at that point[133]. Extending this idea to three dimensions complicates the matter slightly as this process can now be repeated an infinite number of times by taking a projection of the 3D manifold onto any plane and computing the curvature of the resulting 2D curve. This is avoided by using the principal curvatures, which are the maximum and minimum values of curvature, obtained by an eigenvalue operation. These principal curvatures are always along directions that are orthogonal to one another. By convention, principal curvature for a closed surface is taken to be positive if it is bending towards the center of the shape and negative otherwise; or in familiar terms, the curvature of a sphere is positive while a negative curvature would indicate bending in the opposite direction.

With these two values of principal curvature, there are historically two methods to average the values resulting in two measures of the curvature. These are the mean and Gaussian curvatures, as shown in (7.1a) and (7.1b):

$$\varkappa_m = \frac{k_1 + k_2}{2} \tag{7.1a}$$

$$\varkappa_G = k_1 k_2 \tag{7.1b}$$

where $\varkappa_m$ and $\varkappa_G$ are the mean and Gaussian curvatures, respectively, and k_1 and k_2 are the principal curvatures. As the arithmetic mean, the mean curvature provides the intuitive measure of curvature as a description of generally how the surfaces is bending at a point[134]. The Gaussian mean is the square of the geometric mean and is a good method for determining if the surface is elliptic or hyperbolic[134]. An elliptic surface is the type of surface typically envisioned, in which both directions bend the same way, like a bowl or a sphere. Whether the curvature in an elliptic region is positive or negative, because the Gaussian curvature is the product of principal curvatures and an elliptic surface shares the same sign for both values of principle curvature, the Gaussian curvature will be positive. A hyperbolic surface is one in which the two directions bend in opposite directions, creating a saddle point. In this case, each direction will have a different sign and so the Gaussian curvature is negative. Perhaps the most common example of this type of Gaussian curvature is a torus, or donut shape, where the interior of the torus is is hyperbolic while the exterior is elliptic.

Both the mean and Gaussian curvature are extensive properties that depend on the absolute size of the object, in contrast to both CPE and convexity, which are intensive. Additionally, the curvature is not a single value describing the entire surface. Curvature is something that can be computed for every point on the surface of the reverse micelle, and so it is actually a distribution. Figure 7.1 displays several mean curvature distributions for a set of ellipsoids to help illustrate what the curvature distribution of real shapes look like. Note that these distributions were computed numerically, causing small amounts of noise due to using discrete points rather than a continuous function. Figure 7.1 illustrates the extensive nature of the curvature distribution as the volume was not kept constant, causing the entire distribution to shift slightly between each ellipsoid.

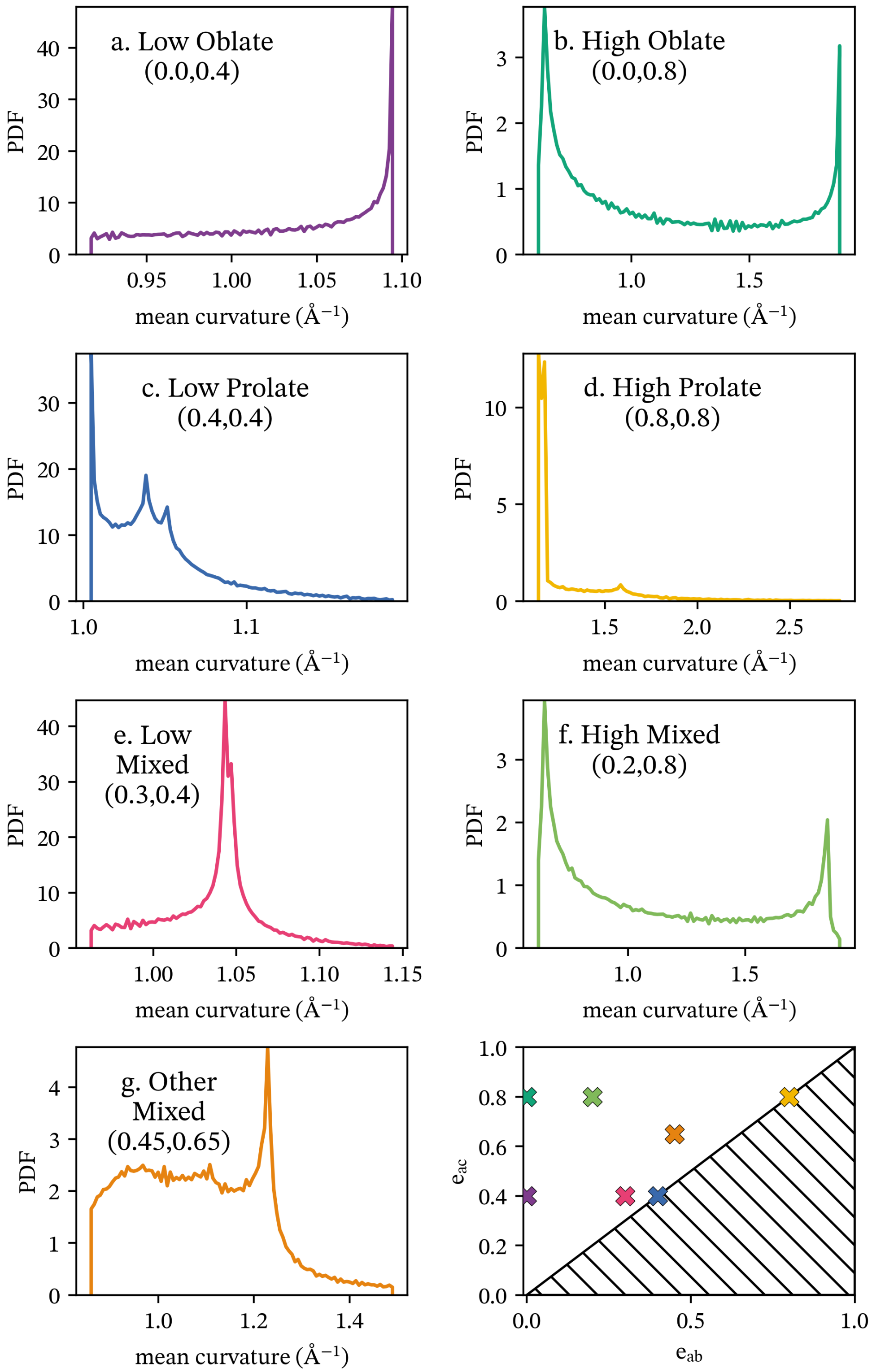

Figure 7.1: a-g) The mean curvature distribution of a selection of different ellipsoids. For each ellipsoid, semiaxis $a = 1$ while semiaxes b and c were varied. The exact values are given as a coordinate-pair in the plot as (b, c). h) A CPE plot for each of the ellipsoids whose mean curvature distribution is plotted above.

7.2 Curvature Distribution of the CHARMM Simulation

I only computed the curvature distribution for the first 100 ns of the CHARMM simulation for reasons that will be shown shortly. Due to the large amount of data involved in the curvature distribution, it is helpful to start by looking at small selections. Figure 7.2 presents the mean curvature distribution for two random frames as well as a visual depictions of the surfaces of the reverse micelle at each frame. Figure 7.2 also provides several comparisons to guide its interpretation. The mean curvature distribution fits well to the sum of two Lorentzians, which we compare to the curvature distribution of an ideal ellipsoid with the same CPE and dimensions as the micelle at the selected time points. Because curvature is an extrinsic value, the curvature of a sphere of the same size as the micelle is provided for size-independent comparisons.

As Figure 7.2 shows, the peak maxima of each fitted Lorentzian appears near a peak in the curvature distribution of the ideal ellipsoid. This suggests that the fitted Lorentzians represent the two peaks from the ideal ellipsoid curvature distribution, albeit with significant broadening. There are several sources of broadening relative to an ideal ellipsoid. First, with bumps and divots on its surface, the reverse micelle is not a true ellipsoid. If we assume that the observed shape is an ellipsoid that has been subsequently distorted, then creating a divot on the surface removes some population from the curvature value at that place and creates population on the left side of the distribution— at negative values. Since the most likely curvature values for a randomly chosen portion of the surface are the peak values of the distribution, the creation of divots has a “Robin Hood” effect that will tend to decrease the peak intensities and raise the low intensity, left side of the distribution. The boundary points between a divot’ s negative curvature and rest of the surface creates flat regions of zero curvature at the interface that further broaden the distribution— the divot removes a curved portion to create the flat interfacial region— and smooth the

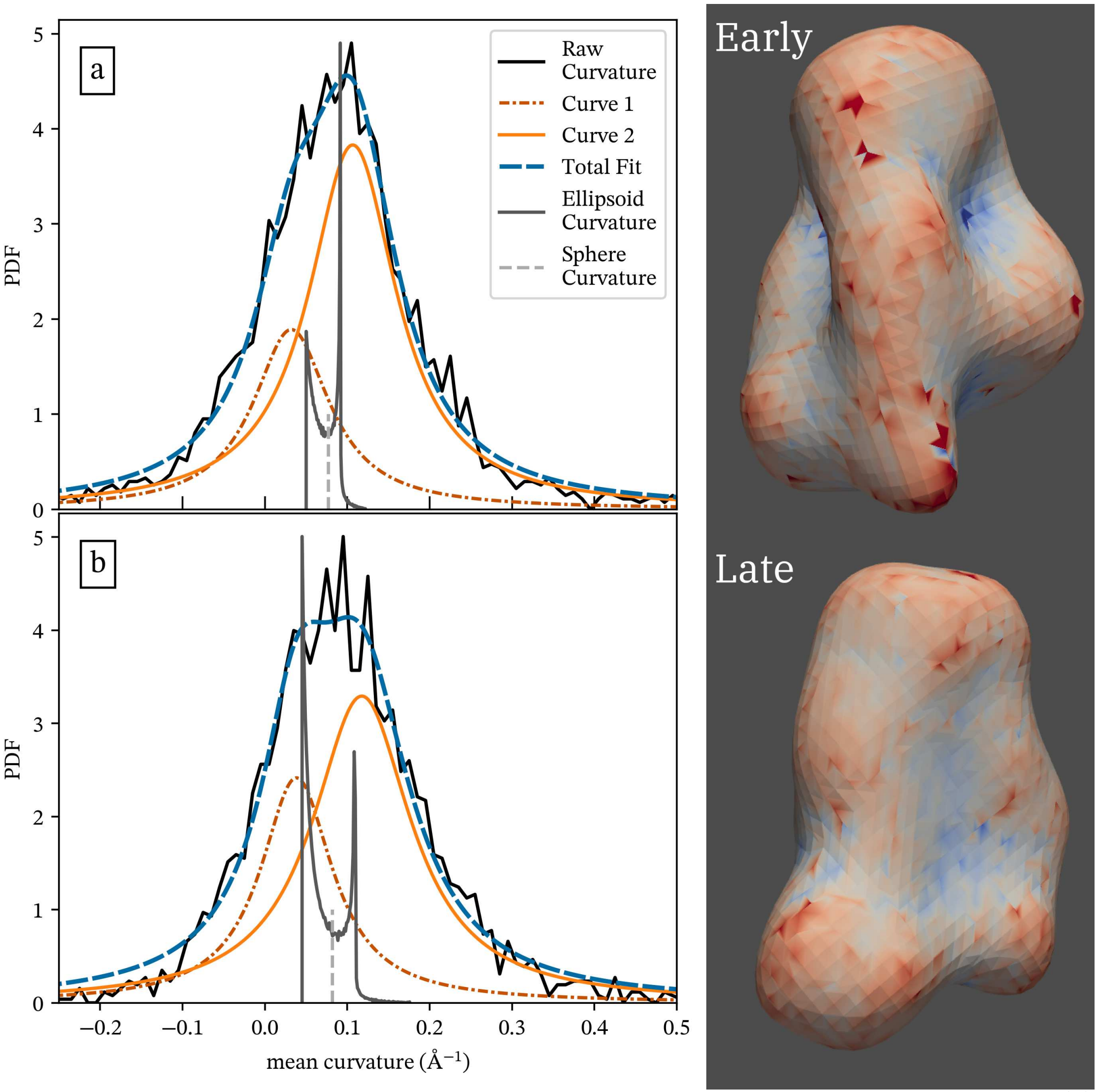

Figure 7.2: The curvature distribution of two random frames from the beginning (a) and end (b) of the trajectory (Legend: Raw Curvature). Each curvature distribution is fitted to the sum of two Lorentzians (Legend: Curves 1/2, and Total Fit). The distribution for the ellipsoid computed from the moments of inertia is also plotted, renormalized so it fits on the graph (Legend: Ellipsoid Curvature). The expected distribution for a sphere of this size is shown to provide a reference for an object this size (Legend: Sphere Curvature). Images on the right show the micelle at these times, colored by curvature with positive values in red.

distribution between the left side and the peak values. An analogous process occurs for bumps on the surface, operating on the right side of the distribution, removing population density from the peaks, increasing, and smoothing the high curvature population on the right wing of the distribution.

The bump-and-divot broadening described here does not act symmetrically on the peak in the same way that common sources of broadening, such as homo- or heterogeneous spectroscopic broadening, do. Rather than modifying a well-defined spectroscopic transition, the broadening mechanism described here quite literally erases the values of the imaginary ellipsoid from which the observed shape is "created", and replaces them with other values. This literal substitution, rather than modification, of values can explain why the fitted Lorentzians bracket the peaks of the curvature distributions of the ideal ellipsoids. That is, moving values from the peak areas to the left- and right-sides of the distribution shifts the means of each peak, causing the Lorentzian fits to be slightly to the side of the corresponding peaks of an ideal ellipsoid.

A second broadening mechanism arises because the curvature is computed numerically. For a well-defined function, the curvature can be calculated analytically and is exact. However, on a Delauney triangulated surface, there is no real curve[135]. There are only points connected by straight lines approximating a curved surface, and an algorithm must be used to estimate this curvature. The algorithm we use to calculate curvature (a part of the PyVista package[87]) sometimes creates erroneously large values that shift population from the peak areas and move it toward the extreme tails of the distribution. A more advanced algorithm may reduce this error, but will not eliminate it entirely. This has the effect of broadening the distribution symmetrically. These overestimated values appear as the deeply colored spots on the representative micelle surfaces shown in Figure 7.2 that are clearly out of place with the surrounding values.

Having described, in Figure 7.2, the curvature distributions for two select times, Figure 7.3 presents the mean and Gaussian curvature distributions over the full simulation. The mean curvature shows a relatively broad peak that is roughly symmetric and centered on a positive value. In contrast, the Gaussian curvature, shows a sharp, asymmetric peak with significantly more positive Gaussian curvature than negative, but the median value is almost exactly zero, skewing only slightly positive. The micelle is a topological ball, so even with its various irregularities, the most likely shape should have more elliptic than hyperbolic points, which readily explains the asymmetry.

The most striking feature of Figure 7.3, is how little it changes over time. Over the course of the simulation, there is no evidence of a significant broadening, narrowing, or shift in peak position of the overall distribution. This consistency in curvature is in contrast to the walking behavior observed in the CPE in Figure 4.2. The simulation ensures that volume of the micelle is constant, which can explain the lack of variation in the curvature distribution. Constant volume implies that the curvature must revolve around some similar set of values because curvature is an extrinsic value. Drift toward either larger or smaller curvature values would indicate a change in size, which is impossible for a system of set stoichiometry such as the simulated reverse micelle. In contrast, CPE is an intrinsic value, so it can exhibit walking behavior not mirrored by the curvature distribution. A constant volume also means that any deformation to one side of the shape must move the displaced volume somewhere else, creating an endless supply of roughly similar bumps and divots.

Overall, Figure 7.2 implies that the curvature distribution for AOT reverse micelles is a sort of convolution of the CPE and the convexity since it can be modelled as the curvature distribution for the corresponding ellipsoid measured by CPE, which has been broadened according to the deformations measured by convexity. And so while the curvature distribution may be important for some amorphous shapes, it does not appear to be important for AOT reverse micelles and was subsequently dropped without analyzing the full trajectory or every simulation.

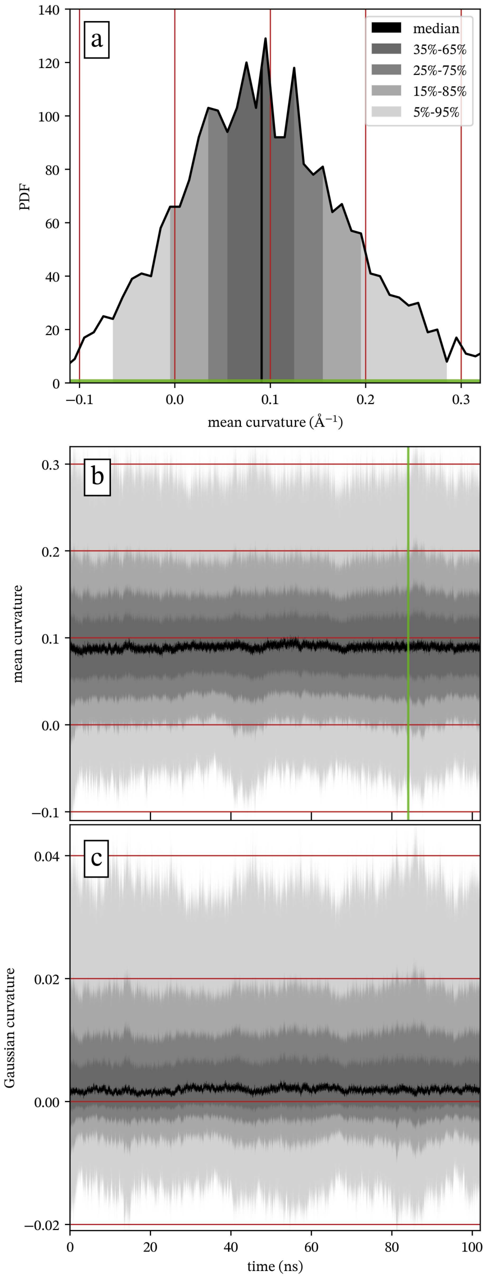

Figure 7.3: (a) Mean curvature distribution from the early frame of Figure 7.2. The black vertical line is the median of the distribution. The other shades of gray represent percentile ranges encompassing a given % of the data around the median: from darkest to lightest, 30%, 50%, 70%, 90%. (b) Mean curvature distribution over all times. The example in part (a) represents a single slice of the data presented here, shown as a green line. (c) Gaussian curvature distribution over all times.

Chapter 8

Shape Dynamics

The information in this chapter has been published in Ref. 3.

8.1 Introduction to Shape Dynamics

Beyond a description of what shapes the AOT reverse micelles adopt, we also explore how the reverse micelle shapes change. The autocorrelations of both CPE and convexity measure how the shape changes with time according to each metric. Because CPE is a pair of values, *e.g.* a vector, it requires a vector autocorrelation, while the convexity autocorrelation is computed as a scalar autocorrelation. The typical autocorrelation is written as:

$$ACF(t_{lag}) = \langle A(t)A(t + t_{lag})\rangle \tag{8.1}$$

where $A(t)$ represents some time-dependent signal at time t, and $\langle\rangle$ denotes the ensemble average. There is really no difference between the vector and scalar autocorrelation once one realizes that the product of $A(t)$ and $A(t + t_{lag})$ can be generalized to higher dimensions with the inner product. In this case, a scalar product, like the typical autocorrelation of a single-valued function such as my convexity data, can be thought of as the product of vectors of dimension one. The inner product is then equivalent to scalar multiplication. In higher-dimension vectors, such as my CPE data, the inner product is equivalent to the dot product. Both autocorrelations are normalized to 1 at $t_{lag} = 0$ and subtracted the mean value from the time series dataset before calculation of the autocorrelation.

I fit the autocorrelations to the sum of two exponential decays, as shown in (8.2).

$$ACF^i(t_{lag}) = A_s^i e^{-t_{lag}/\tau_s^i} + A_\ell^i e^{-t_{lag}/\tau_\ell^i} \quad , \quad A_s^i + A_\ell^i = 1 \qquad (8.2)$$

In (8.2), A_ℓ and A_s are the amplitudes for the long and short time components respectively and were assumed to sum to 1 because of the normalization, thus removing one fitting parameter. The independent variable, t_{lag}, is the lag time, and τ_ℓ and τ_s are the long and short time constants, respectively. The superscript, i, represents either CPE or convexity (Ξ).

8.2 Shape Dynamics of AOT Reverse Micelles

Figure 8.1 summarizes the autocorrelations of the CPE and convexity, with Figure 8.1a and b showing values for the time constants, τ_ℓ and τ_s, respectively, and Figure 8.1c presenting the amplitudes for each component. Plots of the raw and fitted autocorrelations and the residuals of the fit for each simulation and shape metric are provided in Appendix C. I attribute the long time decays, τ_ℓ^i, shown in Figure 8.1a, to those larger amplitude, concerted changes in shape and the short time response, τ_s^i, shown in Figure 8.1b, to small, fast, random fluctuations resulting from thermal motion. Thermal motion can create random changes in shape. For example, random twisting of the AOT tail groups can change the CPE and convexity by at least some small amount, but overall should represent a minor and fast change to the shape because such motion is random and therefore just as likely to increase as decrease the CPE and convexity for a given configuration.

It appears generally true that τ_ℓ^Ξ is greater than τ_ℓ^{CPE}, but the magnitude of this difference varies quite a bit. This makes sense in terms of what CPE and convexity measure. The convexity represents the behavior of the entire surface and will not change significantly unless the arrangement of the entire reverse micelle changes.

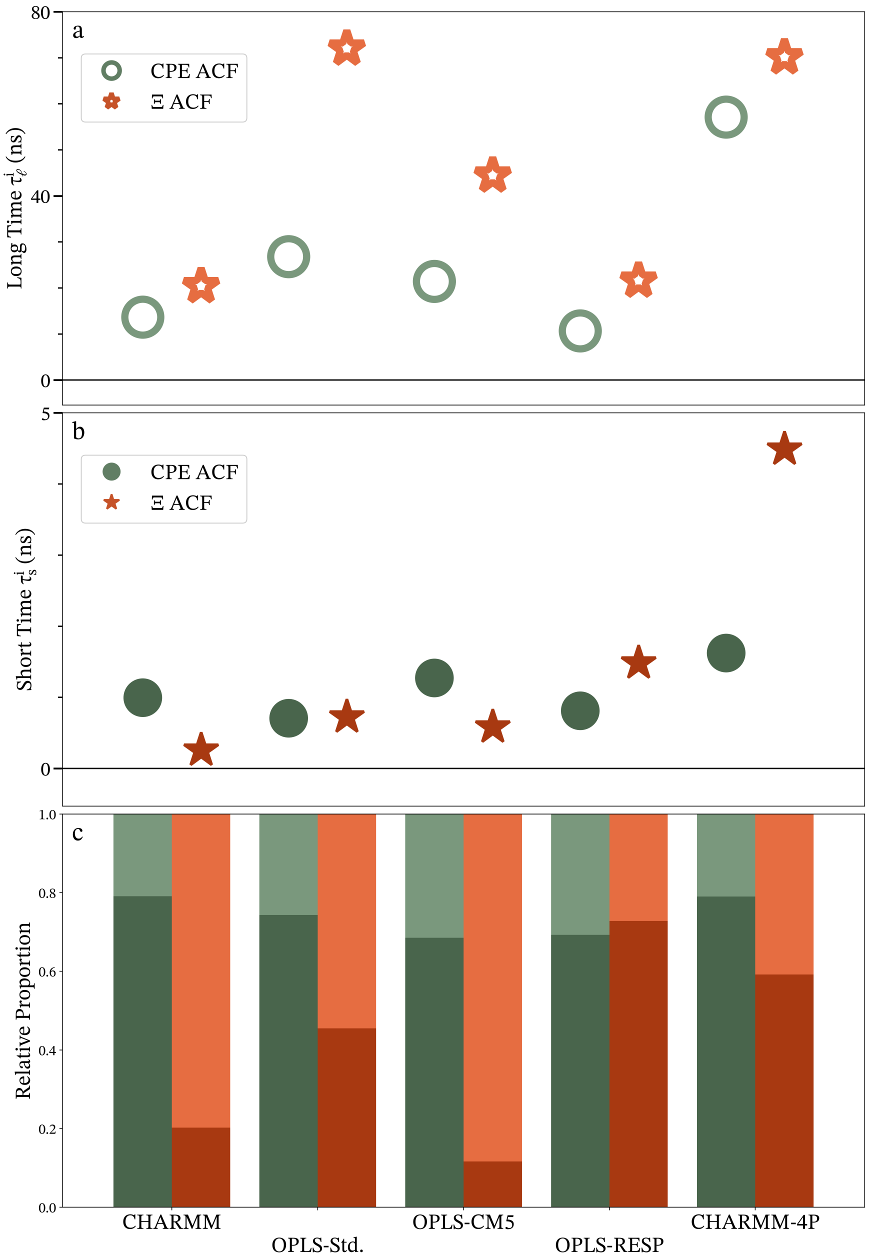

Figure 8.1: Fit parameters from biexponential fits to the CPE and convexity autocorrelations: (a) τ^i_{long}, long time constant, (b) τ^i_{short}, the short time constant, (c) bar graph representation showing how the amplitude is split between the short and long time component. The shades of each color match their corresponding time constant; the bottom, darker colored bar corresponds to A^i_s and the top, lighter colored bar corresponds to A^i_ℓ.

By contrast, the CPE will change if just one of the semiaxes of the rotationally equivalent ellipsoid changes, *e.g.* it is possible to have a situation where $\delta a = \delta c = 0$ but $\delta b > 0$, which causes $\delta e_{ac} = 0$ but $\delta e_{ab} > 0$, where δ is used to denote the change of the given value between two points in time. So CPE can change if only a portion of the reverse micelle changes while the convexity, as a measure of the entire surface, requires a larger and more concerted change in shape, which implies that convexity should exhibit a slower autocorrelation decay due to having greater "inertia". I also note that the variations in reverse micelle shape observed in the CHARMM-4P simulations are significantly slower than almost all of the other simulations; only τ_{ℓ}^{Ξ} for the OPLS-Std simulation is similar. This is consistent with the hypothesis that the CHARMM-4P reverse micelle has a higher surface tension that damps the shape changes more vigorously and therefore maintains its shape coherence significantly longer.

Based on these autocorrelation results, I note that the reverse micelle shape varies on the timescale of tens of nanoseconds, anywhere from 10 to 70 ns depending on the shape metric considered and the model employed. This result places constraints on the experiments and metrics that shape could reasonably impact. For example, consider water's rotational diffusion, which occurs on the order of 1 ps[6,16,40,136,137], and the fluorescent lifetime of a typical fluorescent probe, which is on the order of ≈1 ns[138]. Based on the timescales of each of these processes, I can rule out shape as an important factor in water's rotational diffusion based on the four orders of magnitude difference between these two timescales, but I cannot *a priori* rule out shape as a factor influencing the fluorescent lifetime of a probe molecule placed inside of a reverse micelle. It is still possible that shape has no impact on the fluorescent lifetime of a probe molecule inside of the reverse micelles, but I cannot guarantee that shape does not play a role in the fluorescent lifetime.

This observation could serve as a useful razor[6] to rule out shape as a factor where appropriate, and narrow the focus of work to only processes shape could reasonably be expected to impact.

---

[6] A philosophical razor like Occam's razor, *i.e.* a deductive reasoning heuristic for eliminating unlikely possibilities.

Chapter 9

Water Rotational Anisotropy Decay

The information in this chapter has been published in Ref. 3.

9.1 Introduction to Water Rotational Anisotropy Decay

The rotational anisotropy decay of water is a measure of how long it takes water to lose rotational coherence, or the average rotational lifetime of water molecules[139,140]. This serves two purposes for this work. First, it is an interesting property to study in its own right. It has previously been shown that nanoconfinement has a major impact on water dynamics of all kinds, including the rotational dynamics[6,16,40,136,137]. Therefore, it is important to see what impacts, if any, the different force fields used in my simulations have on the water rotational dynamics. The water model is expected to play the dominant role in determining the dynamics, but the core/shell hypothesis for the water populations within nanoconfinement implies that the water/AOT interactions may also play a major role[6,16,40,136,137]. As the first work to study the impact of force field on AOT reverse micelles in detail, this work is in a unique position to study the role AOT interactions play on water dynamics.

The second reason to measure the rotational anisotropy decay of water is that it is an experimentally accessible value[6]. While this work is as complete as possible, it remains firmly in a computational realm. Finding ways to relate my work back to experiment to verify the results is extremely important. While the water rotational anisotropy decay is unlikely to bear significant relation to the shape— see Section 8.2 and the razor given by relative timescales— the relation to experiment provides a connection to experiment nonetheless. Therefore, water's rotational dynamics can serve as both a measure of how water is impacted by the reverse micelle as well as a useful connection between experiment and simulation that can be used to benchmark at least a portion of simulation against both experiment[6] and past simulations[40].

The rotational anisotropy decay is generally equivalent to the time correlation function in most scenarios, including here[139], and is defined by (9.1):

$$C_2(t_{lag}) = \langle P_2\left(\hat{u}(t + t_{lag}) \cdot \hat{u}(t)\right)\rangle \tag{9.1}$$

where C_2 is the time correlation function, or equivalently the rotational anisotropy decay, t_{lag} is the lag time, $\langle\rangle$ indicates the ensemble average, $P_2()$ is the second Legendre polynomial, and $\hat{u}$ is any vector representing water's orientation, usually the unit vector along the OH bond[139,140].

Experimentally, the rotational anisotropy decay is accessed via heterodyned pump-probe IR experiments. It is constructed from the signal detected at parallel and perpendicular polarizations to the incoming beams, and a term Piletic,*et al.* refer to as the "growth term" resulting from heating effects following vibrational relaxation[6]. The relation is given by (9.2):

$$r(t) = 0.4C_2(t) = \frac{S_{\parallel} - S_{\perp}}{S_{\parallel} + 2S_{\perp}(t) - 3G(t)} \tag{9.2}$$

where $r(t)$ is the rotational anisotropy decay measured experimentally, $S_{\parallel}$ is the signal detected parallel to excitation, $S_{\perp}$ is the signal detected perpendicular to excitation, and $G(t)$ is the growth factor accounting for thermal heating. Notice that the measured value is a scaled version of the rotational anisotropy decay accessible by simulation, which simply requires the correct scaling factor (5/2) to allow comparisons between simulation and experiment directly. The other experimental consideration is that signal is lost after the vibrational lifetime while simulations can average over any arbitrary length of time, provided only that a long enough trajectory was performed. Practically, this means that experiment can only measure water rotational dynamics out to a few picoseconds while simulations will often measure the dynamics to several hundred picoseconds.

9.2 Water's Rotational Anisotropy Decay in AOT Reverse Micelles

Figure 9.1 shows the rotational anisotropy function computed for each of my simulations on a log-log plot, as well as several fits reported in literature. Because I calculate the water dynamics from a 100 ps run (see Chapter 2) there are 1000 instances to average at $t = 0$ ps, there is only one instance at $t = 100$ ps and so the increasing noise observed at longer times is expected. In each of my simulations, the rotational anisotropy exhibits the expected, loosely exponential decay, and confirm that water rotational dynamics are significantly faster than shape dynamics, as predicted.

Factors known to affect the water rotational anisotropy decay include confinement[6,40,136,137], as well as the water model employed[141,142]. Although bulk water and water in large reverse micelles ($w_0 > 20$) generally exhibit a single exponential decay, water in smaller reverse micelles exhibit a more complex and slower decay[6]. Previous works found that water in confinement fits well to either a stretched or triexponential decay at shorter times ($t <\sim 20$ ps)[40,136,137], while long time dynamics exhibit a power law decay[40,143–145]. It is also well known that the dynamics of TIP4P/2005 water, including rotational dynamics, are significantly slower than TIP3P water dynamics[141,142]. This water model difference may explain the difference between the CHARMM simulation, the only simulation using TIP3P water, and the remaining simulations, all using the TIP4P/2005 water model, shown in Figure 9.1.

The solid black lines in Figure 9.1 denote fits to the rotational anisotropy decay of water in my simulations of AOT reverse micelles. Despite previous works finding

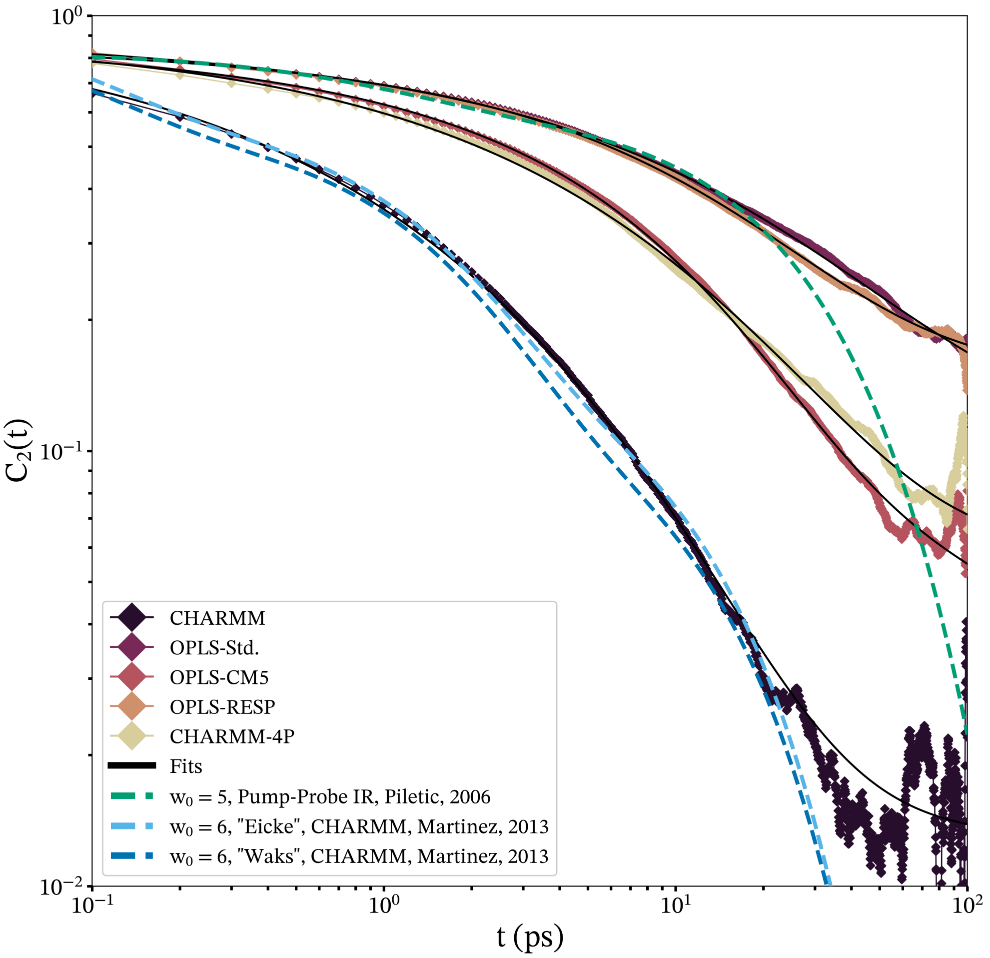

Figure 9.1: The rotational anisotropy decay for each simulation on a log-log plot. Each simulation is fitted to the sum of two stretched exponentials, shown as black lines. The dashed lines represent the fits for rotational anisotropy decay reported in literature[6,40]. Note that Piletic, *et al.* report time-resolved anisotropy, $r(t)$, which is related to rotational anisotropy, $C_2(t)$ by $r(t) = 2/5C_2(t)$; we multiply their fit by 2.5 to adjust for the difference[6].

more complex fits with some form of exponential decay at short times and a power law decay at long times, the water in all of my reverse micelle simulations fit best to a sum of two stretched exponential decays at all times. The fitted parameters for each of our simulations is provided in Appendix H. I only fit to the first 10 ps of the decay, yet the double stretched exponential fit matches very well with the rotational anisotropy decay for each simulation's entire dataset, out to 100 ps, demonstrating unexpected predictive capabilities. For comparison, Figure 9.1 also presents the fits reported from molecular dynamics simulations by Martinez, *et al.*, as well as the IR pump-probe spectroscopy results of Piletic, *et al*[6,40]. as colored, dashed lines. As already noted, experiment is limited to times less than approximately 5.5 ps; but there is no significant divergence between experimental and computational works until ~20 ps, which explains why experimental works employ simpler fits.

$$f(t) = A_1 e^{(-t/\tau_1)^{\beta_1}} + A_2 e^{(-t/\tau_2)^{\beta_2}} \tag{9.3}$$

All of the fits to rotational anisotropy decay of water attempt to find a function that both models the data well and provides a useful interpretation of the phenomena, and while the double stretched exponential model I use is somewhat more complex than previous fits, it is no less useful in providing a potential mechanism. The double stretched exponential fit is readily explained by a core and a shell population, which is a heterogeneous form of kinetics broadening and agrees with previous interpretations[6]. The stretched exponentials, as opposed to simple exponentials, introduce the additional caveat that both populations are also subject to homogenous broadening. While this is new, it is well supported by the quality of our fits in comparison with the quality of past work's fits[6,40]. The types of kinetics exemplified by the double stretched exponential, containing both homogeneous and heterogeneous dispersion, represent a special and slightly simplified case of the Slow Heterogeneity model proposed by Berg and Darvin to describe situations like the one here, suggesting that there is precedent for this style of kinetics[146,147]. Because this finding supports the core/shell model of water within AOT reverse micelles, it is worth mentioning that our shape findings for AOT reverse micelles suggest that the thickness of the shell layer is less than previously predicted. A sphere, like the one assumed in Piletic, *et al.*'s calculation of the thickness of the shell layer of interfacial water[6], minimizes the surface-area-to-volume ratio. Because these calculation were based on the relative concentration of each water population, proportional to the volume, our results for CPE and convexity would indicate that the real surface area is larger than previously predicted and therefore the shell is thinner than previously predicted.

The water rotational anisotropy decays presented here and the fits reported in literature show that my work reproduces others' computational and experimental results, given the appropriate parameters. Although the CHARMM simulation and the simulation presented by Martinez, *et al.*, use the same force field, slight differences exist between them. Specifically, Martinez, *et al.* simulated $w_0 = 6$, a slightly larger value than our $w_0 = 5$, and they used two different aggregation numbers; these details can account for differences between our work and theirs[40]. It is difficult to determine if our work exactly reproduces past work without directly applying our shape metrics to past simulations, but the similarity in water dynamics confirms that our CHARMM simulation reproduce other aspects of past simulations well, and therefore suggest that our work is likely reasonably similar to past work[36,38–43,70]. This suggests that although different aggregation numbers and w_0 values may impact the shape, our general observations about shape likely apply not just to our own simulations, but to past simulations on reverse micelles, as well.

For times shorter than ~20 ps, our OPLS-Std and OPLS-RESP simulations are remarkably similar to the experimental results reported by Piletic, *et al.*, particularly given that these force fields were not parameterized to any experimental quantity. Limitations of pump-probe spectroscopy lead our simulations and the experimental pump-probe IR spectroscopy results to diverge at times longer than ~20 ps[6], as previously noted. It is probable that if experiment could measure the rotational anisotropy decay at longer times, the divergence between our work and experiment would disappear. The OPLS-CM5 and CHARMM-4P simulations are better than the CHARMM simulation at reproducing experiment, as is to be expected for moving from a 3-site to 4-site water model, but do not reproduce experiment nearly as well as the OPLS-Std and OPLS-RESP models. The similarity of the OPLS-Std and OPLS-RESP simulations to experiment does not mean that all aspects of these simulations match experiment, but it does verify that the water dynamics inside of these simulations are a faithful representation of the behavior of water inside of AOT reverse micelles. It is clear that future work aimed at studying water dynamics within reverse micelles would be well advised to use either our OPLS-RESP or OPLS-Std parameters with the TIP4P/2005 water model.

Chapter 10

Radial Distribution Functions

Portions of the information in this chapter have been published in Ref. 3. Specific author contributions are provided in Appendix A.

I have computed the radial distribution functions (RDFs) for several key AOT-water interactions. The most common form of the radial distribution function, and the one I computed here, is given by (10.1):

$$g_{ab}(r) = \frac{1}{N_a \rho_b} \sum_{i}^{N_a} \sum_{j}^{N_b} \frac{\delta(r - r_{ij})}{4\pi r^2 dr} \tag{10.1}$$

where g_{ab} is the RDF between atoms a and b, N_b is the number of atoms b over which the summation has be computed, ρ_b is the local number density of atom b and practically for the simulation is measured as the total number of atoms b in the simulation divided by the volume of the simulation box, r_{ij} is the distance between the i^{th} atom of a and the j^{th} atom of b, δ is the Dirac delta function[148,149]. The way I have written this function, with the Dirac delta, follows naturally from the underlying math which starts from an integral over a continuous distribution converted to a summation over a discrete distribution[149], but would be all but impossible to implement. This is why I have also written in the infinitesimal dr, because practically, the function is evaluated as a histogram, counting the number of atoms b within a thin spherical shell between r and $r + dr$ of each atom a, and the normalizing volume for this sum must include the thickness of that shell.

In a typical, liquid phase RDF, the function is normalized (see (10.1)) such that it decays to a value of 1, that is $\lim_{r\to\infty} g(r) = 1$. This is because the function is normalized by the number density and therefore, in the large r limit, as the number density of a thin shell stabilizes on the bulk number density of atom *b*, yielding a fraction equal to 1. However, in a reverse micelle, the atoms are not uniformly distributed and so this is no longer true. In a finite simulation box, there should instead be a slow decay to zero as the thin shell over which atoms are counted grows large enough to no longer include the reverse micelle itself and the number of atoms counted drops to zero.

I have computed the RDFs between several sets of atoms focused on the water/AOT interface, mostly because these are the most "interesting" RDFs to examine. That is, most of the work studying AOT reverse micelles is focused on the chemistry happening in the water pool inside of the reverse micelle and so the water and how it interacts with the AOT surfactant are of key interest. I have tabulated the RDFs for AOT sulfonate oxygens and the sodium counterions, the AOT sulfonate oxygens and water oxygens, the AOT sulfonate sulfurs and water oxygens, and the sodium counterions and water oxygens in Figure 10.1. All of the RDFs computed here were averaged every five frames from the 1 μs total trajectory, for a total of 25,000 frames averaged. The distances were computed from 0 to 35 Å, which is about the side length of the simulation box without running into errors as pressure fluctuates, in 0.0875 Å wide bins. Since the long distance portions of the RDFs are mostly featureless decays to zero, Figure 10.1 only displays distances out to 10 Å. The full-range RDFs are provided in Appendix I.

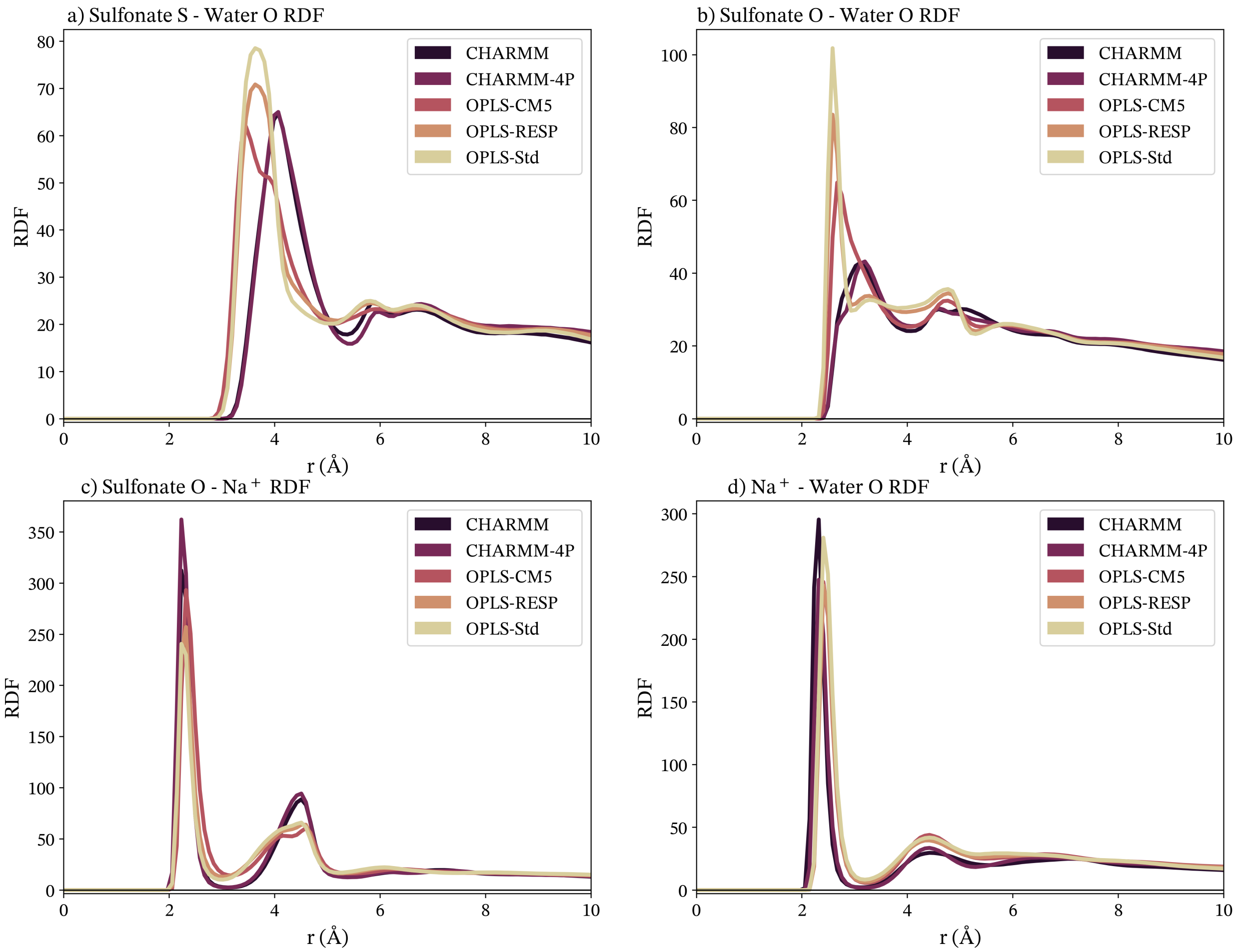

Figure 10.1: RDFs for some key atoms in the AOT reverse micelles, labeled above the plots. This figure focuses on the initial few peaks in the RDF, out to 10 angstroms.

Figure 10.1 shows a clear split between force field families. The CHARMM and CHARMM-4P simulations are nearly identical between all atom pairs. There is more variety between OPLS force fields, but they still all follow the same general patterns. For example, the sulfonate S-water O RDF shows that each OPLS force field has slightly different peak heights for the first solvation shell peak just short of 4 Å, and the OPLS-CM5 simulation shows a distinct shoulder around 4 Å that is not seen in any of the other OPLS force fields, but generally, each of the OPLS force field's first solvent shell is centered on the same distance, and has roughly the same peak width and shape, which is distinct from the location, width and shape of the first solvation peak for the CHARMM simulations.

The CHARMM simulations indicate that the water model has very little impact on the atomic pairwise interactions between AOT and water; but at the same time, the OPLS simulations appear to indicate that the partial atomic charges do impact the pairwise interactions somewhat. These are somewhat paradoxical results, on the one hand suggesting that the RDFs are insensitive to the parameters of their neighbors, and on the other suggesting that they are. I believe these data may indicate that the sulfonate parameters dominate the interactions with water, making the RDFs insensitive to water model but much more sensitive to the partial charges of the sulfonate group. This might mean that water's preferred orientation and interaction with the sulfonate group is fairly independent of exact parameters. In other words, either because the hydrogen bond network is too rigid or just because water only has one real way of interacting with an anion, its geometry is more or less set and the only question is where that geometry is centered. As Figure 10.1 shows, switching from an OPLS to a CHARMM-based force field results in a slightly greater distance between sulfonate and water in the first solvation shell.

The RDF also offers an interesting possible view into shape. In the typical RDF, one averages over all atoms available in a simulation and over all frames, or at least enough frames to obtain a good average. But with all the shape information available in the simulations, I can test the specific impact that shape has on the RDF by only averaging over atoms or frames that satisfy certain conditions. I have named these as the "discriminated RDFs", since they discriminate between atoms or frames meeting a condition and those atoms or frames that do not. Figure 10.2 presents the mean curvature discriminated RDFs for the AOT sulfonate sulfurs- water oxygens atom pair. In Figure 10.2, the black line shows the regular RDF, the same as those shown in Figure 10.1. The yellow and blue lines, though, present the RDF only over

AOT molecules whose local mean curvature value is in either the highest (blue) or lowest (yellow) 2.5% of all mean curvature values in the entire simulation. Note that this severely limits the averaging of the RDFs, using just 2.5% of the averaging of the full data set. For these calculations, the RDF was only calculated for the range 0-15 Å, in bins 0.1 Å wide.

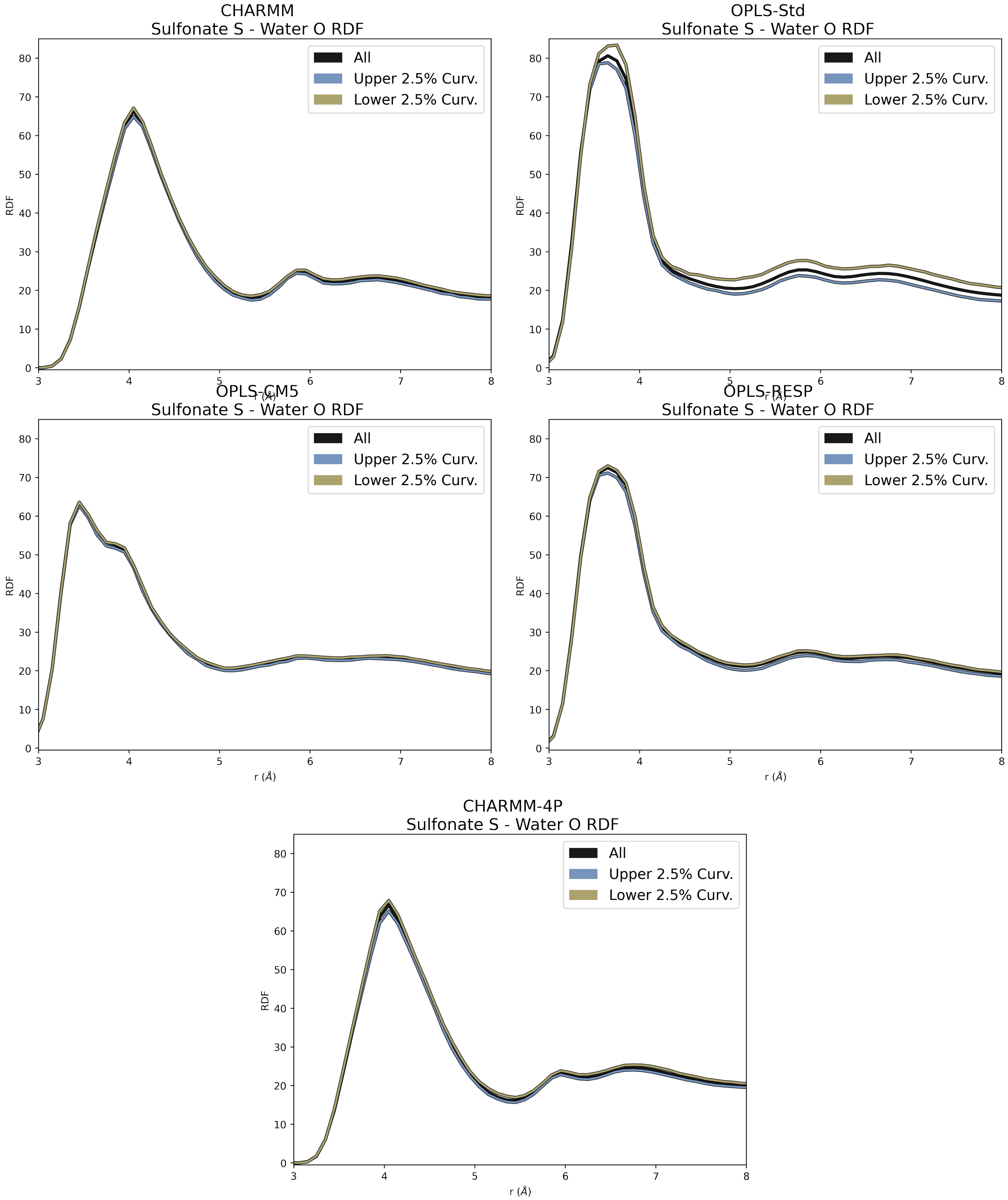

Figure 10.2: The curvature-discriminated RDFs for each simulation.

The curvature discriminated RDFs in Figure 10.2 illustrate that there is a very slight increase in the probability of finding water around the AOT headgroup when the curvature is very low, bending away from the AOT molecule and therefore theoretically allowing more water molecules to arrange themselves around the sides.

Conversely, there is very slightly less probability of finding water around the AOT headgroup when the curvature is very low, bending towards the water interface and therefore theoretically pushing water away from the AOT molecule. In Figure 10.2 I have pushed the mean curvature to the absolute extremes and observed very little difference between the discriminated and non-discriminated RDFS. And so while one could repeat a similar process between different atom pairs or using convexity instead of the curvature, I stopped these efforts at this point as the shape of the reverse micelle appears to have very little impact on the molecular-level organization of the reverse micelle.

Extensive time and effort could be made to dissect every minor difference between each of the simulations and slight changes to the various peaks in the RDFs, but it is not clear how informative or useful this effort would be. Immediately, it is clear that the RDFs do not follow the same pattern between force fields that is observed in any other data I have collected; which I discuss in much greater detail in Chapter 11. On its face, this discrepancy suggests that the pairwise interactions between specific atoms have very little impact on the collective behavior of the reverse micelle and vice versa. It is not clear that the RDF is an appropriate measure for a self-assembled particle like a reverse micelle, especially if it is amorphous. The obvious proof is in the large distance limit of $g(r)$ for a reverse micelle. The radial distribution function was specifically designed on the assumption of a uniform solution and not a two phase system like a reverse micelle. Additionally, the decay to zero holds some information on the shape, capturing the probability that atoms on opposite sides of the reverse micelle will be a certain distance apart. But that shape information includes some “rotations” in the form of averaging over particles from all over the particle as well as every fluctuation of shape possible. This makes it a convoluted method for obtaining shape information that is only useful in very specific situations; but more importantly, it means that it is not strictly the indicator of atomic interactions that is usually assumed, being tainted by shape. At short distances, the shape almost certainly has little to no effect, as Figure 10.2 demonstrates, but at larger distances, it will. There will be a gradual change between the two and it is unclear how one would attribute a specific difference in the RDF to either pairwise effects or shape effects, or what relative weights one would give to each contribution. This complexity makes it Quixotic and temerarious to attempt to dive further into minute differences in the RDF.

Chapter 11

Force Field Parameters, Patterns and Groupings

Portions of the information in this chapter have been published in Ref. 3. Specific author contributions are provided in Appendix A.

I created the series of simulations presented here intending to correlate specific simulation parameters and interactions with specific shape effects, but the various results reported present conflicting stories about these parameters. Depending on the simulation parameter, I find different natural groupings, as summarized in Figure 11.1. For example, the generic and AOT-specific groups are consistent between both CPE and convexity, as shown in Figure 4.3 and Figure 6.2, but have no relation to the shape dynamics shown in Figure 8.1 or to the water dynamics shown in Figure 9.1. And although it is somewhat expected that the force field that governs intermolecular interactions would lead to similar molecular organizations as shown in the RDFs in Figure 10.1, patterns among the RDFs also do not correlate well with any of the patterns seen in the other metrics studied in this work.

Reverse micelles are difficult to parameterize as they involve numerous and complicated intermolecular interactions: those between water and AOT, AOT with itself, as well as AOT with the non-polar phase. Parameterization involves altering the simulation parameters to recreate one or more experimentally observed quantities on the assumption that reproducing one quantity will reproduce many, if not all, other quantities. However, the fact that the simulations do not fall into consistent groups between the various metrics indicates that the metrics involved are largely independent of one another. This makes it hard to find metrics that fully capture all the myriad interactions present in a reverse micelle and all the diverse behaviors we observe

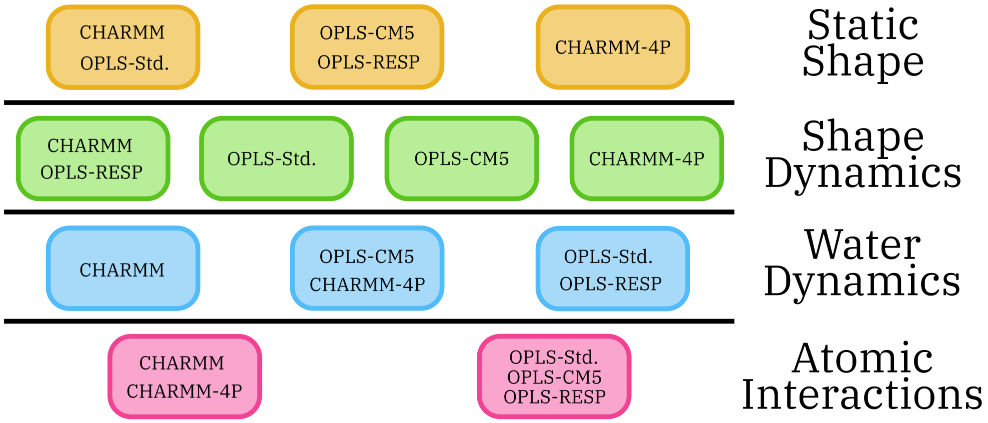

Figure 11.1: A summary of the approximate similarities between simulations across each data type presented in this paper. Static shape refers to both CPE and convexity distributions. Shape dynamics refers to the autocorrelations of CPE and convexity. Water dynamics refers to the rotational anisotropy autocorrelation. Atomic interactions refers to the RDFs, provided in Chapter 10.

in them. It seems that reverse micelle parameterization is only truly accurate for the narrow aspect on which the system was parameterized. For example, if one could parameterize AOT so that the reverse micelles exactly reproduced an experimentally-derived RDF, they could not expect simulations using these parameters would reproduce other metrics such as shape, shape dynamics or water dynamics any more accurately than any other force field. Such a theoretical force field would be guaranteed to reproduce the RDF and only the RDF of an experimental AOT reverse micelle.

This greatly complicates any attempt to benchmark AOT reverse micelle simulations, but while it may be difficult to parameterize a force field or find the best force field, my results also generally show that most aspects of the reverse micelle are decently robust. While there are differences in CPE and convexity, the general findings of a non-spherical, non-convex reverse micelle are consistent. While the shape dynamics vary greatly between simulations, they are generally all of the same order of magnitude, and so on for the water dynamics and radial distribution functions. Therefore, while it may be exceedingly difficult to find a perfect set of force field parameters, it is likely acceptable to use any reasonable force field for most purposes.

Along with parameterization, it is worth commenting on the validity of the force fields I partially parameterized by updating the partial charges on all AOT atoms. A more rigorous parameterization would involve repeating the DFT calculations and charge partitioning calculations multiple times for multiple different configurations of AOT. This would effectively average out configuration-dependent artifacts in the partial charges. Additionally, multiple calculations in different configurations can be used to help equalize the partial charges on chemically-equivalent atoms, such as the three equivalent hydrogens on a methyl group. As can be seen in Table D.2, RESP forces equivalent atoms to have identical charges but the CM5 method does not. However, I believe our results indicate that this is not a significant issue for the simulation of AOT reverse micelles. The shapes of both simulations are nearly identical. The difference in the dynamics, both the shape dynamics and water rotational dynamics, between the OPLS-CM5 and OPLS-RESP simulations, may be caused by these small differences in charge, but many other factors could explain these differences as well. Therefore, I believe that the results presented here indicate that both force fields are valid force fields for use in the simulation of AOT reverse micelles.

Beyond parameterization, it is surprising that several of these metrics do not overlap more closely. This may have implications for at least some of the mechanisms governing the behavior within reverse micelles. The observation that the shape and shape dynamics exhibit different groupings suggests that the parameters and interactions leading to a particular shape are completely independent of the parameters and interactions that determine how that shape changes, even though the shape and its dynamics seem intimately related. In Section 6.2, I postulated that the convexity is related to the surface tension and the shape is largely a result of random deformations of a loosely-bound interface. But because the convexity itself and the autocorrelation of convexity have different patterns between simulations, it seems that the surface tension is independent of the random fluctuations that lead to changes in shape. Unfortunately, it is still unclear whether these random fluctuations are internal or external to the reverse micelle, but the disconnect between the shape and its dynamics implies that the origin of these fluctuations is likely complex. For example, if the fluctuations originate in the fluctuations of the water pool, then the CHARMM-4P simulation should show a closer relationship between the convexity— and therefore surface tension— of such a tightly-bound water pool and the dynamics of those fluctuations. The most probable way to explain the disconnect is to suggest that multiple factors are involved, making the pattern much more complex than what we are able to discern with the metrics and simulations presented.

Consider, also, the relationship between the RDFs, a representative metric measuring atomic-level interactions, and the shape metrics, which measure collective behavior directly. Although RDFs are extremely helpful, they do not appear to have any particular relation to other aspects of the reverse micelles. The RDFs, shown in Figure 10.1, fall along force field lines, *i.e.* CHARMM simulations are similar, regardless of water model and OPLS simulations are similar, regardless of partial charges. On one hand, this is not entirely surprising. The process of parameterization is complex and generally leads to entirely unique pairwise interaction potentials between atoms, which are what the RDFs measure. In a typical parameterization scheme for a force field family's intermolecular forces[63,65], the partial charges for each atom type are based on a quantum mechanical calculation of various examples of a particular atom type, which are then used to compute partial charges, in the same way I obtained AOT's partial charges for the OPLS-CM5 and OPLS-RESP simulations (see Chapter 2). Then the Lennard-Jones parameters are iteratively altered until a test simulation reproduces some experimental target value of choice within an acceptable limit. This makes the intermolecular forces somewhat colinear. One could theoretically overestimate the charges on all of the atoms and simply adjust the Lennard-

Jones parameters to account for this and end up with a reasonable force field according to some metric; while the pairwise interactions between atoms is vastly different from a force field that did not overestimate the charges. Therefore, the differences in the RDFs between the CHARMM and OPLS force fields are not surprising.

But the RDFs split along force field lines while no other metric studied here shares this pattern, which bears thinking about. In chemistry, we often approach the complex, multi-tiered organization of materials by utilizing either a bottom-up perspective, deriving macroscopic understanding from microscopic behavior, or from a top-down perspective, working backward from macroscopic observables to obtain microscopic understanding. These approaches have been incredibly successful throughout chemistry, taking for example statistical mechanics, a bottom-up approach, and thermodynamics, a top-down approach. However, the disparities between our reverse micelle RDFs, shape, shape dynamics, and water dynamics indicate that a bottom-up microscopic approach is not sufficient to explain the mesoscopic behavior of reverse micelles. In our reverse micelles, there are only three components—water, AOT and isooctane— making this one of the simplest possible examples of a mesoscopic assembly. But even within this simple system, there are 95 unique atoms leading to 8930 unique two-body interactions, of which an RDF only examines one pair at a time. This number expands exponentially when considering three or more body interactions, that are known to be important to accurately modeling chemical systems as simple as pure water[150,151]. So even our relatively small and simple system has far too many interactions to completely parameterize with RDFs alone. RDFs may be helpful as a bellwether, but it is important to remember the limitations of such a narrow, microscopic parameter. Therefore, my results appear to emphasize a divide between the microscopic, atomic and molecular level, and the mesoscopic, self-assembled level. Even in the limit of one of the smallest possible self-assembled particles, the collective behavior of the reverse micelle appears distinct from the individual, microscopic interactions which build the assembly.

Chapter 12

Selected Directions for Future Work with Shape Metrics

12.1 Scope and Theory

The analysis of the shape of soft, amorphous materials is not quite new, but undeniably far from a mature field. While I have endeavored to make this work as complete and rigorous as possible to provide a solid foundation for future work, there is still much to be done. Of course, the framework developed here could be extended in many different directions, but I am going to focus here on just a few of these directions in this section. Specifically, these are areas I have noticed where improvements or further insight could be gained with slightly more work, and although I did not have the time or resources to finish this work myself, I did make some progress. I am including these ideas here in the hopes that they will be helpful to an interested party in the future.

12.2 An Hypothetical Future for CPE

Although I believe there are clear benefits to using CPE over the other similar metrics available (see Appendix F), CPE is not a perfect metric either. An ideal moments-of-inertia-based metric would comprise two variables that are completely orthogonal to each other. In such a system, one variable would report the sphericity of the shape while the other object would report on the oblate/prolate nature of the shape. With CPE, the aphericity must be a function of both e_{ab} and e_{ac}, a point that is proven just by looking at the oblate/prolate divider line (see Section 4.2), which also implies that the oblate/prolate nature is also a function of both e_{ab} and e_{ac}. Therefore, I believe that there exists a better metric, although I was unable to uncover it so far in my work.

But I also believe I know where to start looking for such a metric. When looking at the oblate/prolate divider line, it seems like there is a polar coordinate version of CPE that is very close to this ideal, fully orthogonal set of values describing the shape via the moments of inertia. Moving along the oblate/prolate divider line, by definition, does not change the oblate-versus-prolate nature of the shape and so it must be changing the sphericity and only the sphericity, making this line act very much like the radial component of a polar coordinate system. The issues from there, however, are two-fold. First, although the oblate/prolate divider line is similar to a radial component of a polar coordinate system, it is a curve and not a straight line. Second, if we accept this polar coordinate vision of the ideal metric, then we need something analogous to the angular component that will sweep the oblate/prolate divider across the graph, so the oblate/prolate divider line only provides half of the needed information.

One could theoretically address the first issue by parameterizing the oblate/prolate divider line, as is done in (4.6), in which n would act as the radial component of this ideal metric. To create the angular component, there is some difficulty in making the metric continuous, but a stop-gap solution would be to simply re-solve (4.5) for another constant value of oblate/prolate-ishness and then continue the same workflow given in equations 4.6-4.8 to obtain a new line, now representing some constant value of either oblate-ish or prolate-ishness. That is, consider that the following is equivalent to the left-hand side of (4.5):

$$(a-b)-(b-c)=0 \tag{12.1}$$

that now presents the previous logic in terms of a root-finding problem. To generalize this, consider that this difference of differences does not have to be equal to zero, so I will introduce some parameter, η, that will represent an arbitrary value of oblate- or prolate-ishness as opposed to the dividing line between the regions. Then making the same generalizing substitutions as in (4.5), we can find a more useful representation of η.

$$\begin{aligned} (a-b)-(b-c) &= \eta \\ [d(1+m_1)-d]-[d-d(1-m_2)] &= \eta \\ d\,[m_1-m_2] &= \eta \end{aligned} \tag{12.2}$$

Notice that I am no longer using n because now $|a-b| \neq |b-c|$, so I have introduce $m_1 = a-b$ and $m_2 = b-c$. With (12.2), there is now a method and parameterization for measuring the oblate-ish/prolate-ishness of a shape in a continuous fashion via η. Examining η, we find that it can vary on the interval $[-\infty, \infty]$. If the shape is perfectly prolate ellipsoid, $a > b = c$, then $m_1 > 0$ and $m_2 = 0$, so $\eta > 0$ and $\lim_{d\to\infty} \eta = \infty$. On the other hand, for a perfectly oblate ellipsoid, $a = b > c$, then $m_1 = 0$ and $m_2 > 0$, so $\eta < 0$ and $\lim_{d\to\infty} \eta = -\infty$. The only remaining issues are to generalize and reparameterize the work for the asphericity since the parameterization in (4.6), n, is only defined for the case where $\eta = 0$; and to refine η slightly to ensure that it is an intensive value, *e.g.* so that $-1 \leq \eta \leq 1$.

There are several advantages to such a theoretical metric of shape. First and foremost, the orthogonality of the component variables means that the changes in shape are clearly observed and interpreted. A change in one variable is clearly assigned to a change in the sphericity while maintaining a constant oblate-ish/prolate-ishness and vice versa. This is in contrast to CPE where each of these changes can be approximately determined but are inexact, especially with the non-linear curvature and asymmetry of the oblate/prolate divider line. The other advantage is that this hypothetical metric would be based, from the inception, on shape. By first converting the moments of inertia to semiaxis lengths, the metric is built on a solid and reliable foundation in terms of the metric's interpretation. It is not clear that the other, similar shape metrics would be able to clearly identify where the divider line between oblate and prolate is or extend to a similar, orthogonal shape relation like CPE can. But for this hypothetical metric, being based on the shape, not only is it possible to identify the oblate/prolate divider, but it is intuitively placed, and conveniently centered— the oblate/prolate divider line is defined when $\eta = 0$, placing it exactly center in a radial plot. Finally, this metric has the advantage of working in discrete ranges. Assuming that η can be properly normalized so as to make it intensive, then infinity does not appear in the ranges for either of the theoretical variables. This is relatively cosmetic, but nevertheless a useful property for both interpretation and comparison.

12.3 Speculation on the Hedgehog Hypothesis

Figure 6.3 illustrated a striking and consistent pattern, demonstrating that the Hedgehog Hypothesis was indeed true; the next logical step is to wonder why the Hypothesis created this particular linear fit and not another one? The fact that I found such a consistent pattern despite the many other differences between simulations is also the reason that I cannot actually answer this question. To truly determine what factors impact how the convexity changes as a function of the surfaces, one would need to design experiments that alter the pattern so that changes between experiments can be correlated with changes in the linear fit. But it is an interesting question concerned with fundamental shape behavior and this work would be incomplete without at least some speculation on the observed relation.

The consistency of the pattern in $\Delta\Xi$ is striking and implies a universal mechanism independent of the simulation parameters tested in this work. Between CHARMM and CHARMM-4P, I changed the water model, between CHARMM and the three OPLS simulations I changed the force field family, including all of the inter- and intramolecular parameters, and between the three OPLS simulations, I changed the partial charges, dramatically altering the intermolecular interactions. These were all generally seen to have some impact on the simulation, whether that was the shape, shape dynamics, the RDFs, or the water dynamics, and yet these simulations had identical patterns in $\Delta\Xi$. And so by deductive reasoning, the identity of the reverse micelle seem like one of the few parameters left that I did not test, although this idea has some merit on its own. The pattern in $\Delta\Xi$ and the Hedgehog Hypothesis itself deals with how the reverse micelle can respond to deformations. In the specific examples discussed in Section 6.3 and shown in Figure 6.3a and b, the pattern is effectively the result of how large a divot needs to be before overlap and therefore changes to the convexity occur on one end, and how much radially-arranged surfactant "spikes" alter the convexity on the other end. Both of these values seem to be related to the surfactant identity, supporting the deductive reasoning point. Work testing this hypothesis and pattern should try modelling reverse micelles using another surfactant, such as cetyltrimethylammonium bromide (CTAB) or one of the many surfactants tested by Nave, *et al.*[34,105,106,152].

The low convexity case must have a large divot somewhere, as illustrated in Figure 6.3a. To remind the reader, the Hedgehog Hypothesis states that in this case, the surfactant "spikes" cannot arrange themselves roughly normal to the surface without overlapping, and therefore displace and fill in the divot, resulting in a more convex outer surface and $\Delta\Xi > 0$. Note that the magnitude of this effect is directly related to the volume of overlap that would occur if the surfactants were arranged normal to the surface— or more generally, if they kept the same configuration as before the hypothetical deformation creating the divot in question. I will unimaginatively term this volume as the "overlap volume". If the divot is made deeper or sharper for a given surfactant, that is if there is less average distance between interior, water-pool surfaces across the divot, then the overlap volume increases. If the surfactant is longer for a constant divot size and shape, then the overlap volume increases. As the overlap volume increases, more volume will be filled in and $\Delta\Xi$ increases. The situation may be slightly more complicated than just the length of the surfactant. It is possible that a surfactant like CTAB, which has a linear alkyl tail group, does not tend to extend the full length of the alkyl tail in a real reverse micelle system, which would mean that we likely should be using the effective length of the tail group and not the literal theoretical maximum length of the tail group. Additionally, density or packing may play some role, meaning that the multiple tail groups of AOT or similar surfactants might play a key role. It is too complex to completely predict without studying this behavior in detail, but my argument would go something like this: it seems probable that not all surfactants will pack with the same density, meaning that there are different densities in the tail group regions of different surfactant's reverse micelles. In a divot with some amount of overlap volume, less dense surfactants may be able to compensate not by moving the overlap volume somewhere else and changing the outer surface's convexity, but by adjusting the density to have temporarily a higher density within the divot. This would mean that a less dense packing may lead to decreases in $\Delta\Xi$.

In the other case, illustrated in Figure 6.3b, the inner surface has a very high convexity. The Hedgehog Hypothesis predicts that in this case, the surfactant cannot maintain inter-surfactant spacing as the tail groups extend radially from the inner surface, causing gaps to develop in the outer surface that are not present on the inner surface. For a constant number of radially arranged spikes given by the surfactant tail groups, it is easy to see that the distance between spikes, and therefore the drop in convexity at the outer surface, is proportional to the length of the surfactant tail groups. This is proven mathematically with the arc length. The surfactant tails occupy a specific coordinate on the solid angle and therefore the angle between two such surfactant tails is set at some angle, θ. The distance between the tail groups at a given surfactant tail length is then approximated well by the arc length, given by the formula $L = \theta r$. And so it can be seen that the length increases as the radius, *i.e.* the surfactant tail length, increases. There is just one complicating factor. So far I have assumed that there are a constant number of spikes per unit area, *e.g.* a constant surface area per surfactant headgroup. This is, of course, liable to change between different surfactants, especially different surfactants with different headgroups. If, for example, CTAB can be packed more tightly than AOT at the water/surfactant interface, then it can create more spikes and introduce fewer divots at the oil/surfactant interface. Therefore, one would generally expect two relations to be true. First, a longer surfactant tail group would lead to larger $\Delta\Xi$, for a given head group. Second, that a smaller surface area per headgroup will lead to a smaller $\Delta\Xi$ measured at the same locations.

The next issue to address, though, is how to work with these predictions that operate only at endpoints. If I am right and the relationships I have outlined exist as I have described between surfactant identity and the pattern observed in $\Delta\Xi$, then both the slope and y-intercept, the m and b terms in the standard equation of a line, are dependent on the same basic properties of the surfactant identity. Instead of working in terms that cannot be clearly separated, it makes sense to work in endpoints at either extreme. Two points define a line and the data I have shown in Figure 6.3 demonstrate a linear trend. So we only need to understand the behavior at the endpoints and draw a line between them. Last, in the preceding two paragraphs, I have outlined how I believe that the surfactant identity will impact $\Delta\Xi$, but if the linear trend is explained by endpoints, then this is only half of the equation, *i.e.* I have predicted the

y-value of the endpoints, but not the x-value. Unfortunately, it is not clear how one would go about predicting this given the information we have now. The extreme values for convexity observed during the simulation changed between simulations and I never tested any other surfactant other than AOT, so I have no way to predict the convexity behavior of other reverse micelles. Assuming there is a relationship between convexity and the surface tension like I hypothesized in Chapter 6, then the surface tension could be used to predict the x-value of the endpoints. This shouldn't be too great of an issue, in any case. The exact value of $\Delta\Xi$ is dependent on the convexity value observed. That is, even though the CHARMM-4P simulation had a significantly higher median convexity and much smaller distribution of convexity values than all of the other simulations, it still falls along the same pattern because while the convexity values were higher, this simply lead to smaller differences in $\Delta\Xi$. Therefore, appropriately scaled predictions for some constant convexity value should be sufficient to predict the $\Delta\Xi$ behavior of a given surfactant's reverse micelles.

So while I cannot test this theory more explicitly with the data I have available, I do have an interesting observation and problem, a method of testing the problem, and a framework for evaluating the results. I hope that someone will be able to follow up on this work at some point in the future.

Chapter 13

On the Requirements for Experimental Verification

13.1 Defining What we Want to Know

While I have a great amount of information about the shape of AOT reverse micelles, and have done everything I could to avoid biasing the simulations, testing for errors based on force fields by testing multiple force fields, and comparing against experiment as much as possible, all of this work remains theoretical. The obvious question remains: does any of the work presented here have any bearing on real life? Do these simulated micelles reflect the behavior of real reverse micelles in solution? The only definitive way to answer that is to directly, experimentally measure the shape of reverse micelles.

It is worth it to start by considering what one actually wants to get out of experimental verification. It is one thing to be able to experimentally verify that AOT reverse micelles are not spherical and another thing entirely to obtain the kind of detailed information on shape— *e.g.* the CPE and convexity— that we are able to obtain through simulation. I believe there are basically three questions that one could attempt to answer experimentally. Each has varying degrees of impact on how we understand AOT reverse micelles as well as my simulations, and I will go over each one in order from the simplest and easiest to prove to the most complex and most difficult.

The easiest question is simply, “are AOT reverse micelles spherical or not?” One needs to start by clarifying on what time scale and what level of imperfection they are referring to when they ask this, of course. My simulations illustrate AOT reverse micelles that may appear spherical on a long enough time scale but are definitely not spherical on a sub-nanosecond time scale, and so defining the period over which you consider spherical is critical. Additionally, thermal fluctuations and discrete molecules guarantee that nothing can ever be truly spherical. For example, spherical metallic nanoparticle has divots at some point because it is composed of discrete atoms in a lattice and not a continuously defined curve on an infinitely small length scale. And so one should also determine what level of imperfections they consider acceptable in classifying something as either "spherical" or not. Conveniently, the CPE and convexity provide a helpful and quantitative measure of doing this, *e.g.* by stating something like "convexity must be between 0.995 and 1", although this may not be easy to translate into acceptable tolerance levels for an instrumental measurement. Answering this question of sphericity would not define a shape unless the answer is returned in the positive, that it is spherical. However, it would support my findings so that one can presume to use my results with more confidence. Additionally, it would provide a basis for doing the extra work to determine shape experimentally knowing that there is something to find. Finally, it is simply a far easier question to answer experimentally, making it a good first step.

The next question one could attempt to answer experimentally is an intermediate one. This question could be formulated many ways depending on the exact method one chooses to use to measure it, but would go something like "what is the average distance to the interface that a probe at some known position experiences?" That is, the experiment would attempt to simplify shape down to a 1D distance between two fixed reference points. Perhaps one measures the average distance across the reverse micelle via a method sensitive to Na^+. Or perhaps one measures the distance between a probe in the center of the water pool to a probe buried in the interface, measuring a pseudo-radius. This is a much harder question to answer than whether or not the particle is spherical. The first question was a binary state that would need nothing more than a model result expected if the particle were spherical and a comparison determining if this model fits the results or not. This question is similar but builds on that slightly to shift from a binary answer to a quantitative one. Even if this experiment were successful, one would still not know the exact shape, but they would be able to demonstrate that it is not spherical, generally give some idea of how non-spherical it is and provide a way to compare against other systems, simulated or experimental. It is therefore a significant advancement over the first question in determining and qualifying what the shape of a reverse micelle is.

The last question one could ask is to fully characterize the shape of AOT reverse micelles. This may not be in the same manner as I do in simulations, *e.g.* with CPE and convexity, but would measure some analogous. Presumably, the results of such an experiment could be directly compared or calculated from simulation so that one could accurately say that either the reverse micelles in my simulations are or are not a good representation of reality. However, this experiment is extremely stringent and nearly impossible to perform, as I will show.

13.2 Potential Experiments to Address Each Question

Having considered what exactly we would like to see out of experiment, is there an experiment that could answer these questions and what would the requirements of such an experiment be? I will start with the simplest question, whether AOT reverse micelles are spherical on a sub-nanosecond timescale. As already noted, this is essentially a binary question. It is either true or it is false. Therefore, we only need a model that can be measured experimentally, and the appropriate statistical test for the model. The most natural experiment to answer this question is some form of small-angle scattering experiment or experiments, either small-angle neutron scattering (SANS) or small-angle X-ray scattering (SAXS), or perhaps even a similar method such as static light scattering (SLS). While all of these instruments measure the ensemble average, averaging over times long enough to sample many millions of unique shape configurations per reverse micelle in the illuminated volume, which likely averages over the scattering of many million reverse micelles, depending on the instrument itself, the average of a non-spherical shape should have a different profile of scattering across the radius of the averaged sphere compared to a true sphere. The only question is whether we can predict the scattering of a non-spherical particle with enough accuracy and measure with enough precision to build a statistically significant experimental test. There is a way to potentially build up a very accurate model for the predicted scattering of a simulated reverse micelle and that is with a neural net, specifically a Generative Adversarial Network (GAN). In this model, one network is trained on molecular dynamics simulation data to generate potential configurations while the other network is trained on molecular dynamics simulation data to determine if a given configuration is realistic. The two networks are pitted against each other, each attempting to fool the other one, creating a situation where steel sharpens steel and both neural networks benefit. Using this method, one could create many thousands, perhaps millions, of times more configurations than are possible with MD simulation alone; generating a significantly more precise scattering curve prediction for a simulated reverse micelle. It would then be up to the experimentalists to collect a scattering curve of sufficient resolution and precision to differentiate between the possible models. Given that different force fields produce different shapes in MD simulations, one could use this method to evaluate whether experiment could differentiate between the results, find the most accurate force field, *etc*. This is not a simple project, however. Although there are several "levels of theory" that could be employed, ranging from a solid, uniform scattering length density, to a gradient or custom profile of scattering length density, to exact atomic coordinates, even the simplest project would be a fairly large undertaking involving multiple MD simulations and extensive work with neural nets. In the most complicated case with exact atomic coordinates, a custom Monte Carlo code may need to be written and used as well.

An alternative approach to answering the question of whether the AOT reverse micelles are spherical could utilize the concept of a core/shell assembly of water, as hypothesized by Piletic, *et al.*[6]. They found two distinct populations of water in AOT reverse micelles based on pump-probe IR spectroscopy, which they explained by supposing that the water was comprised of a core of bulk-like water in the core of the reverse micelle surrounded by a shell of tightly-bound and restricted interfacial water, forming a shell. Piletic, *et al.* calculated a theoretical thickness to this shell based on the assumption of a spherical shell. Because a sphere minimizes the surface-area-to-volume ratio, my results of a non-spherical and amorphous reverse micelle would suggest that they likely over-estimated the thickness of this shell. Therefore, if one could experimentally measure the thickness of the shell, one could then calculate the surface-area-to-volume ratio. Like all of the experiments answering this basic question, the results would be relatively rudimentary, but this result could serve as a useful discriminator that disqualifies shapes which do not fit experimental results. The challenge in this approach is a careful and exact determination of the aggregation number, and related to that concept, the polydispersity of the reverse micelles. Piletic, *et al.* based their work on the relative populations of each spectroscopic signature. However, the volume of the shell, and therefore the relative populations of water in the core and shell, is highly dependent on the reverse micelle size. Therefore, with sufficient polydispersity, it may be impossible to build up a stastically significant test one way or another using this method as the "smearing" due to polydispersity overshadows any differences caused by shape. Still, if it is possible, it presents perhaps the simplest measurement available to answer this question.

The second question provided some hints as to its measurement in the formulation of the question, namely that it will likely involve some sort of probe molecule.

There are numerous experiments that may potentially fit this bill, but there are some stringent requirements to being able to obtain useful information from the results. The probe must be small enough to not significantly perturb the system. The probe must be in some way sensitive to the environment; and not just generally sensitive, but have a quantitative, hopefully precise, distance-dependent sensitivity to its environment. For this experiment to work, it must also be possible to accurately determine the position of the probe within the reverse micelle. It is of little use knowing how far the probe is from, for example, the Na^+ counterions if one does not know where the probe resides. Lastly, and perhaps most importantly, in order to provide any information not available from the previous question and a theoretical small-angle scattering experiment, the probe has to be able to provide signal on a very fast timescale. If the experiment can only measure the ensemble average distance, then it does not provide any useful advantage over small-angle scattering experiments, which also measure the ensemble average. My work would suggest that a sub-10 ns timescale would be optimal, but incremental improvements are likely the pragmatic solution. That is, if there were a method and probe molecule that had a 1 μs resolution, that may be 2 orders of magnitude too high, but that is still far less averaging than a multi-hour experiment and therefore offers significantly more information with less averaging than established work. One would need to perform an analysis to determine how much averaging there can be before a reverse micelle appears spherical, which will depend largely on the specific experiment (*e.g.* how similar are the spherical and non-spherical signals for the method, what is the resolution of the method, etc). I would like to point out the work of Miller, *et al.*, who used ^{19}F NMR to study the location of sodium ions in AOT reverse micelles[26]. As an NMR experiment, the timescale was on the order of ms at best, and the exact location of both the F^- and the Na^+ was somewhat speculative, but illustrates well how this type of experiment would work. With a little more work characterizing the location of F^- and Na^+

in solution, the experiment could serve as the ms-timescale starting point for this line of experiments. This was not the purpose of the work of Miller, *et al.*, so it is not a surprise that their work does not perfectly fit the requirements I have outlined, but it is remarkably close to the type of experiment I am proposing by pure serendipity. Overall, these are more difficult experiments to do compared to determining if the reverse micelle is spherical, but also provides significantly more information and seems like something that could potentially be accomplished with modern methods and instrumentation.

The last question, measuring the shape of AOT reverse micelles directly, is the most difficult one. Unlike the previous question, a probe molecule experiment is not sufficient to characterize the entire shape. This leaves either scattering or imaging experiments. At between 1 and 10 nm in size, imaging at that size would require very high energy X-rays before the resolution at the diffraction limit would have enough pixels to resolve the shape. This is impractical for so many reasons as to be comedic. Electron microscopy presents a method with the needed resolution, but many additional challenges. The thin film required could introduce additional interfacial effects not representative of behavior in solution and it is not clear how nanoconfined water would behave under cryogenic temperatures. Perhaps it would vitrify just like bulk water does and it works perfectly, but it also might not, which could mean that the reverse micelles observed are not representative of their behavior in solution. The only other real option is a scattering experiment. However, the requirements for such an experiment to measure the shape of an AOT reverse micelle are extreme. Such a system would have to have light focused down almost to the diffraction limit so as to illuminate one and only one AOT reverse micelle and remove spatial averaging. And to obtain the time-dependent shape rather than the average, apparently spherical shape, the light source would not only have to have a pulse width lower than ~10 ns, but would need to be bright enough to obtain a complete scattering curve from a single pulse. If it takes multiple pulses to obtain the signal, then the shape will have changed and the experiment would only measure the same ensemble average that typical small-angle scattering experiments on AOT reverse micelles have measured for years[27–30,34,35,105,106,152]. A pulse that bright would almost certainly eviscerate the reverse micelle in short order, not to mention the fact that it is not guaranteed that a reverse micelle would be within the illuminated volume when the pulse hit. Therefore, measuring the shape of AOT reverse micelles directly would likely have to turn to new and exotic methods. For example, perhaps an electron scattering based method could obtain the necessary resolution in both time and space without destroying the sample. Very cold neutrons have a longer wavelength and thus lose spatial resolution, but could offer a way to create very high intensities without destroying the sample and a carefully designed experiment might be able to work on this principle, although this also implies that there exists an instrument capable of producing extremely short pulses of neutrons, with intensities rivaling or exceeding spallation neutron sources, producing only extremely cold neutrons, which may well be a physical impossibility. And so while this may be a viable experiment in the future, for the time being it seems as if this experiment could only exist in science-fiction.

13.3 Indirect Evidence of the Shape

Despite the challenges of directly studying or characterizing even a part of the shape of AOT reverse micelles noted above, there are certain lines of data that likely contain some amount of shape information. There is a common line of reasoning in the field that goes like this: the aggregation number represents the number of AOT molecules on the surface of the micelle and is therefore a proxy for the surface area of the reverse micelle. The w_0 parameter is a measure of the number of water molecules contained within the reverse micelle, for a given aggregation number at

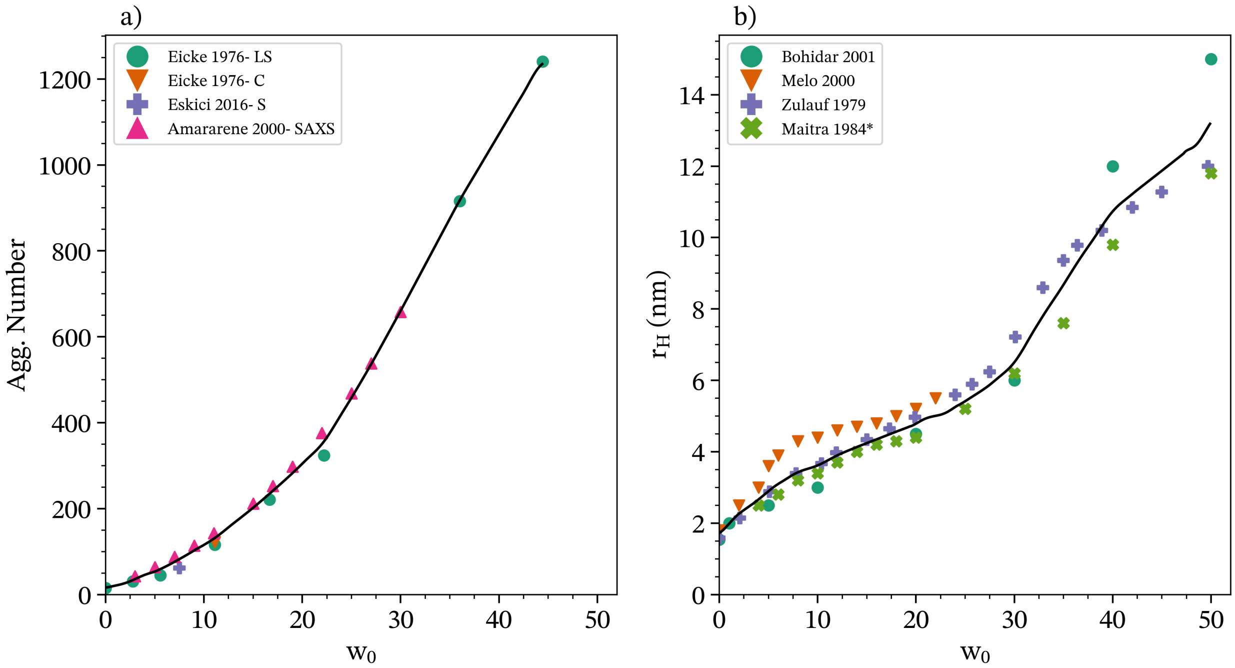

Figure 13.1: a) Plot w_0 versus aggregation number from several literature sources[42,45,46]. Letters after the hyphen denote the method used to measure the aggregation number. LS- light scattering, C- centrifugation sedimentation, S- simulation, SAXS- small angle X-ray scattering. b) A plot of the measured hydrodynamic radius versus w_0 from several literature sources[44,49,153,154]. The black line depicts the average of all datasets which was interpolated onto a common, regular grid. Maitra 1984 is starred because he reports that he used the data from Ref. 153, but his results do not coincide with their results, also plotted. However, Maitra's work is highly influential in the field so I leave it in for completeness.

least, and is therefore a proxy of the volume of the reverse micelle. Therefore, several relations should be approximately true. The aggregation number as a function of w_0 should scale to the power of 2/3. This follows from the fact that for a spherical reverse micelle, a unit increase in w_0 according to the simple rule above predicts an increase in the radius of $\sqrt[3]{r}$, while the aggregation number should scale with the square of the change in radius, giving an overall relation of aggregation number scaling to the 2/3 power compared to w_0. However, Figure 13.1a plots every reliable literature value available, to the best of my knowledge, measuring the aggregation number of AOT reverse micelles as a function of w_0 and it is clear that the relation appears roughly quadratic[42,45,46].

Similarly, the measured size as a function of the w_0 should be well approximated by a cube root function, but as shown in Figure 13.1b, this is clearly not the case[44,49,153,154]. A rough visual interpretation would suggest that there are at least two, likely three, distinct regimes where the behavior changes. However, the approximation of the w_0 as a proxy for the volume and the aggregation number as a proxy for the surface area seem reasonable, leading me to conclude that information on the shape of the reverse micelles is stored within these data. Note that this would also imply that the shape of AOT reverse micelles changes with several distinct regimes sharing similar shapes. All literature values for the size of the reverse micelles reported in Figure 13.1b report the results of dynamic light scattering (DLS) measurements[44,49,153,154]. DLS measures the diffusion of the particles and then applies the Stokes-Einstein equation to calculate the radius a spherical particle would need in order to diffuse like the observed particle, which implies that different shapes should scale differently in terms of the hydrodynamic radius because, as Appendix B shows, different shapes should have different hydrodynamic radii for a given size but should share the same endpoint at infinite size where they all appear spherical. This in turn implies that there must be different slopes for each shape. Additionally, different shapes have different surface-area-to-volume ratios and therefore require a different number of water and AOT molecules to change the reverse micelle's size, which also demonstrates that different shapes should exhibit different trends as the size of the reverse micelle changes. Future work examining the shape of simulated reverse micelles of different w_0 values would be tremendously helpful in studying this data further.

Chapter 14

Conclusion

I have performed a series of five simulations of $w_0 = 5$ AOT reverse micelles in which I varied the force fields to test the impact of the various simulation parameters on the reverse micelle itself. I checked that the equilibration procedure was sufficient and not biased by the starting configuration by creating two simulations using alternative configurations and found that after sufficiently long equilibration, they become indistinguishable from the other simulations. I then characterized the shape of the AOT reverse micelles with the CPE, convexity, curvature distribution, as well as the shape dynamics with the autocorrelations of CPE and convexity. I generally found that the reverse micelles are aspherical and non-convex shapes and that this finding was robust against the simulation parameters employed. However, there are clear differences. In particular, the manner in which the force field was created had a greater impact on the shape than the force field itself, producing the general and AOT-specific groups, while the water model had the greatest impact on shape causing the CHARMM-4P simulation to have the most dramatic departure from the other simulations and being the most relatively spherical and convex reverse micelle.

I also tested several other values to better understand the reverse micelles. I ran a series of additional simulations of AOT in cyclohexane well below the critical micelle concentration to test whether the various AOT force fields could reproduce the experimentally measured dipole moment and found that experiment likely measured a dimer configuration and that each simulation reproduced their results reasonably well. I then measured water's rotational anisotropy decay and determined that, as predicted, TIP4P exhibited slower rotational dynamics, that our CHARMM simulation reproduces past work well, and that the OPLS-Std and OPLS-RESP simulations reproduced experiment very well. Past works have found the rotational dynamics of water in nanoconfinement to be complex, but my fits demonstrated low residuals and high predictive capabilities with the sum of two stretched exponentials. This suggests that the water inside of nanoconfinement really is well-described by a core/shell model, but with the additional caveat of homogeneous broadening being present. I also computed the radial distribution function of several key AOT/water interactions, which showed a clear split along force field lines: CHARMM versus OPLS.

Taken together, my results indicate surprising findings on AOT reverse micelles and their simulations. I confirmed as definitively as possible for a purely theoretical work that AOT reverse micelles are non-spherical. The comparison between simulations also indicate that there may be a relationship between the convexity distribution and surface tension, offering a highly attractive alternative to computing the surface tension if the exact relationship can be found. However, I also found that many properties of the simulations were completely unrelated to each other. There was no clear pattern that would indicate one force field as more or less accurate than another. Instead, it appears as though the various properties of AOT reverse micelles are largely unrelated and that parameterization of one property does not guarantee the rest of the simulation is any more or less accurate.

This work can be said to revolve around studying an old question concerning emergent behavior. If studying the individual components and interactions are insufficient to understand the behavior of the collective, then how do we study this behavior? I have observed clear differences between force fields in the shape and shape dynamics that were not visible to the RDFs or rotational dynamics of water, both of which are classic, atomic- and molecular-level evaluations, demonstrating that shape measures properties not available with classic techniques. I have also presented some evidence suggesting that the convexity of a shape is closely related to the surface tension and that the dynamics of shape are unrelated to the shape itself. All of these points provide key information regarding the ensemble, not the individual molecule; and therefore I believe that I have demonstrated that it is possible to study the behavior of a self-assembled particle via shape in a way that is inaccessible by studying individual atomic pairs or molecular level behavior. Shape offers a mesoscopic series of metrics for studying mesoscopic behavior, which seems to be the only reliable way to study such behavior.

Bibliography

[1] Gale, C. D.; Derakhshani-Molayousefi, M.; Levinger, N. E. How to Characterize Amorphous Shapes: The Tale of a Reverse Micelle. *J. Phys. Chem. B* **2022**, *126*, 953–963.

[2] Gale, C. D.; Levinger, N. E. Predicting the Geometry of Core-Shell Structures: How a Shape Changes with Constant Added Thickness. *J. Phys. Chem. B* **2024**, *128*, 1317–1324.

[3] Gale, C. D.; Derakhshani-Molayousefi, M.; Levinger, N. E. Shape of AOT Reverse Micelles: The Mesoscopic Assembly is More Than the Sum of the Parts. *J. Phys. Chem. B* **2024**,

[4] Levinger, N. E. Water in confinement. *Science* **2002**, *298*, 1722–1723.

[5] Harpham, M. R.; Ladanyi, B. M.; Levinger, N. E. The effect of the counterion on water mobility in reverse micelles studied by molecular dynamics simulations. *J. Phys. Chem. B* **2005**, *109*, 16891–16900.

[6] Piletic, I. R.; Moilanen, D. E.; Spry, D. B.; Levinger, N. E.; Payer, M. D. Testing the core/shell model of nanoconfined water in reverse micelles using linear and nonlinear IR spectroscopy. *J. Phys. Chem. A* **2006**, *110*, 4985–4999.

[7] Park, S.; Moilanen, D. E.; Fayer, M. D. Water dynamics- The effects of ions and nanoconfinement. *J. Phys. Chem. B* **2008**, *112*, 5279–5290.

[8] Wiebenga-Sanford, B. P.; Washington, J. B.; Cosgrove, B.; Palomares, E. F.; Vasquez, D. A.; Rithner, C. D.; Levinger, N. E. Sweet confinement: Glucose and carbohydrate osmolytes in reverse micelles. *J. Phys. Chem. B* **2018**, *122*, 9555–9566.

[9] Miller, S. L.; Wiebenga-Sanford, B. P.; Rithner, C. D.; Levinger, N. E. Nanoconfinement raises the energy barrier to hydrogen atom exchange between water and glucose. *J. Phys. Chem. B* **2021**, *125*, 3364–3373.

[10] Luisi, P. L.; Giomini, M.; Pileni, M. P.; Robinson, B. H. Reverse micelles as hosts for proteins and small molecules. *Biochim. Biophys. Acta* **1988**, *947*, 209–246.

[11] Lye, G. J.; Asenjo, J. A.; Pyle, D. L. Extraction of lysozyme and ribonuclease-a using reverse micelles: Limits to protein solubilization. *Biotechnol. Bioeng.* **1995**, *47*, 509–519.

[12] Melo, E. P.; Aires-Barros, M. R.; Cabral, J. M. *Biotechnol. Annu.*; 2001; Vol. 7; pp 87–129.

[13] Bagwe, R. P.; Khilar, K. C. Effects of the intermicellar exchange rate and cations on the size of silver chloride nanoparticles formed in reverse micelles of AOT. *Langmuir* **1997**, *13*, 6432–6438.

[14] Cason, J. P.; Roberts, C. B. Metallic copper nanoparticle synthesis in AOT reverse micelles in compressed propane and supercritical ethane solutions. *J. Phys. Chem. B* **2000**, *104*, 1217–1221.

[15] Qian, Y.; Wen, W.; Adcock, P. A.; Jiang, Z.; Hakim, N.; Saha, M. S.; Mukerjee, S. PtM/C catalyst prepared using reverse micelle method for oxygen reduction reaction in PEM fuel cells. *J. Phys. Chem. C* **2008**, *112*, 1146–1157.

[16] Harpham, M. R.; Ladanyi, B. M.; Levinger, N. E.; Herwig, K. W. Water motion in reverse micelles studied by quasielastic neutron scattering and molecular dynamics simulations. *J. Chem. Phys.* **2004**, *121*, 7855–7868.

[17] Wiebenga-Sanford, B. P.; Diverdi, J.; Rithner, C. D.; Levinger, N. E. Nanoconfinement's Dramatic Impact on Proton Exchange between Glucose and Water. *J. Phys. Chem. Lett.* **2016**, *7*, 4597–4601.

[18] Boyd, J. E.; Briskman, A.; Colvin, V. L.; Mittleman, D. M. Direct observation of terahertz surface modes in nanometer-sized liquid water pools. *Phys. Rev. Lett.* **2001**, *87*, 1–4.

[19] Venables, D. S.; Huang, K.; Schmuttenmaer, C. A. Effect of reverse micelle size on the librational band of confined water and methanol. *J. Phys. Chem. B* **2001**, *105*, 9132–9138.

[20] Boyd, J. E.; Briskman, A.; Sayes, C. M.; Mittleman, D.; Colvin, V. Terahertz vibrational modes of inverse micelles. *J. Phys. Chem. B* **2002**, *106*, 6346–6353.

[21] Zhong, Q.; Steinhurst, D.; Carpenter, E.; Owrutsky, J. Fourier transform infrared spectroscopy of azide and cyanate ion pairs in AOT reverse micelles. *Langmuir* **2002**, *18*, 7401–7408.

[22] Moilanen, D. E.; Levinger, N. E.; Spry, D. B.; Fayer, M. D. Confinement or the nature of the interface? Dynamics of nanoscopic water. *J. Am. Chem. Soc.* **2007**, *129*, 14311–14318.

[23] Fenn, E. E.; Wong, D. B.; Giammanco, C. H.; Fayer, M. D. Dynamics of water at the interface in reverse micelles: Measurements of spectral diffusion with two-dimensional infrared vibrational echoes. *J. Phys. Chem. B* **2011**, *115*, 11658–11670.

[24] Baruah, B.; Roden, J. M.; Sedgwick, M.; Correa, N. M.; Crans, D. C.; Levinger, N. E. When is water not water? Exploring water confined in large reverse micelles using a highly charged inorganic molecular probe. *J. Am. Chem. Soc.* **2006**, *128*, 12758–12765.

[25] Miller, S. L.; Levinger, N. E. Urea Disrupts the AOT Reverse Micelle Structure at Low Temperatures. *Langmuir* **2022**, *38*, 7413–7421.

[26] Miller, S. L.; Gaidamauskas, E.; Altaf, A. A.; Crans, D. C.; Levinger, N. E. Where Are Sodium Ions in AOT Reverse Micelles? Fluoride Anion Probes Nanoconfined Ions by 19F Nuclear Magnetic Resonance Spectroscopy. *Langmuir* **2023**, *39*, 7811–7819.

[27] Assih, T.; Larché, F.; Delord, P. Evolution of the radius of the inverse micelles at high dilution in the aerosol-OT/water/n-decane system. *J. Colloid Interface Sci.* **1982**, *89*, 35–39.

[28] Pileni, M. P.; Zemb, T.; Petit, C. Solubilization by reverse micelles: Solute localization and structure perturbation. *Chem. Phys. Lett.* **1985**, *118*, 414–420.

[29] Kotlarchyk, M.; Huang, J. S.; Chen, S.-H. Structure of AOT reversed micelles determined by small-angle neutron scattering. *J. Phys. Chem.* **1985**, *89*, 4382–4386.

[30] Quist, P. O.; Halle, B. Water dynamics and aggregate structure in reversed micelles at sub-zero temperatures. A deuteron spin relaxation study. *J. Chem. Soc. Faraday Trans. 1* **1988**, *84*, 1033–1046.

[31] Onori, G.; Santucci, A. Viscosity studies of water-containing reversed AOT micelles. *J. Colloid Interface Sci.* **1992**, *150*, 195–199.

[32] Tomić, M.; Kallay, N. Effect of charge distribution within a droplet on the electrical conductivity of water-in-oil microemulsions. *J. Phys. Chem.* **1992**, *96*, 3874–3882.

[33] Faeder, J.; Ladanyi, B. M. Molecular dynamics simulations of the interior of aqueous reverse micelles. *J. Phys. Chem. B* **2000**, *104*, 1033–1046.

[34] Nave, S.; Eastoe, J.; Penfold, J. What is so special about aerosol-OT? Part I. Aqueous systems. *Langmuir* **2000**, *16*, 8733–8740.

[35] Balakrishnan, S.; Javid, N.; Weingärtner, H.; Winter, R. Small-angle X-ray scattering and near-infrared vibrational spectroscopy of water confined in aerosol-OT reverse micelles. *ChemPhysChem* **2008**, *9*, 2794–2801.

[36] Abel, S.; Sterpone, F.; Bandyopadhyay, S.; Marchi, M. Molecular modeling and simulations of AOT-water reverse micelles in isooctane: Structural and dynamic properties. *J. Phys. Chem. B* **2004**, *108*, 19458–19466.

[37] Chowdhary, J.; Ladanyi, B. M. Molecular dynamics simulation of aerosol-OT reverse micelles. *J. Phys. Chem. B* **2009**, *113*, 15029–15039.

[38] Nevidimov, A. V.; Razumov, V. F. Molecular dynamics simulations of AOT reverse micelles' self-assembly. *Mol. Phys.* **2009**, *107*, 2169–2180.

[39] Vasquez, V. R.; Williams, B. C.; Graeve, O. A. Stability and comparative analysis of AOT/water/isooctane reverse micelle system using dynamic light scattering and molecular dynamics. *J. Phys. Chem. B* **2011**, *115*, 2979–2987.

[40] Martinez, A. V.; Dominguez, L.; Małolepsza, E.; Moser, A.; Ziegler, Z.; Straub, J. E. Probing the structure and dynamics of confined water in AOT reverse micelles. *J. Phys. Chem. B* **2013**, *117*, 7345–7351.

[41] Marchi, M.; Abel, S. Modeling the self-aggregation of small AOT reverse micelles from first-principles. *J. Phys. Chem. Lett.* **2015**, *6*, 170–174.

[42] Eskici, G.; Axelsen, P. H. The size of AOT reverse micelles. *J. Phys. Chem. B* **2016**, *120*, 11337–11347.

[43] Urano, R.; Pantelopulos, G. A.; Song, S.; Straub, J. E. Characterization of dynamics and mechanism in the self-assembly of AOT reverse micelles. *J. Chem. Phys.* **2018**, *149*.

[44] Maitra, A. Determination of size parameters of water-aerosol OT-oil reverse micelles from their nuclear magnetic resonance data. *J. Phys. Chem.* **1984**, *88*, 5122–5125.

[45] Eicke, H.-F.; Rehak, J. On the formation of water/oil-microemulsions. *Helv. Chim. Acta* **1976**, *59*, 2883–2891.

[46] Amararene, A.; Gindre, M.; Le Huérou, J. Y.; Urbach, W.; Valdez, D.; Waks, M. Adiabatic compressibility of AOT [sodium bis(2-ethylhexyl)sulfosuccinate] reverse micelles: Analysis of a simple model based on micellar size and volumetric measurements. *Phys. Rev. E* **2000**, *61*, 682–689.

[47] Sheu, E. Y.; Chen, S.-H. Structure and growth of bis(2-ethylhexyl) sulfosucclnate micelles. *J. Phys. Chem.* **1987**, *91*, 3306–3310.

[48] Giordano, R.; Migliardo, P.; Wanderlingh, U.; Bardez, E.; Vasi, C. Structural properties of micellar solutions. *J. Mol. Struct.* **1993**, *296*, 265–269.

[49] Bohidar, H. B.; Behboudnia, M. Characterization of reverse micelles by dynamic light scattering. *Colloids Surf. A Physicochem. Eng. Asp.* **2001**, *178*, 313–323.

[50] Deák, J. C. Volumetric determination of reverse micelle structural properties and the validity of commonplace approximations. *J. Mol. Liq.* **2022**, *368*, 120680.

[51] Hollingsworth, S. A.; Dror, R. O. Molecular Dynamics Simulation for All. *Neuron* **2018**, *99*, 1129–1143.

[52] Derakhshani-Molayousefi, M.; McCullagh, M. Deterring effect of resins on the aggregation of asphaltenes in n - heptane. *Energy Fuels* **2020**, *34*, 16081–16088.

[53] Tempra, C.; Chamorro, V. C.; Jungwirth, P. Effects of Water Deuteration on Thermodynamic and Structural Properties of Proteins and Biomembranes. *J. Phys. Chem. B* **2023**, *127*, 1138–1143.

[54] Yesylevskyy, S.; Martinez-Seara, H.; Jungwirth, P. Curvature Matters: Modeling Calcium Binding to Neutral and Anionic Phospholipid Bilayers. *J. Phys. Chem. B* **2023**, *127*, 4523–4531.

[55] Berendsen, H. J.; van der Spoel, D.; van Drunen, R. GROMACS: A message-passing parallel molecular dynamics implementation. *Comp. Phys. Comm.* **1995**, *91*, 43–56.

[56] Van Der Spoel, D.; Lindahl, E.; Hess, B.; Groenhof, G.; Mark, A. E.; Berendsen, H. J. GROMACS: Fast, flexible, and free. *J. Comp. Chem.* **2005**, *26*, 1701–1718.

[57] Nosé, S.; Klein, M. Constant pressure molecular dynamics for molecular systems. *Mol. Phys.* **1983**, *50*, 1055–1076.

[58] Berendsen, H. J.; Postma, J. P.; Van Gunsteren, W. F.; Dinola, A.; Haak, J. R. Molecular dynamics with coupling to an external bath. *J. Chem. Phys.* **1984**, *81*, 3684–3690.

[59] Hoover, W. G. Canonical dynamics: Equilibrium phase-space distribution. *Phys. Rev. A* **1985**, *31*, 1695–1697.

[60] Nosé, S. A molecular dynamics method for simulations in the canonical ensemble. *Mol. Phys.* **2002**, *100*, 191–198.

[61] Bussi, G.; Donadio, D.; Parrinello, M. Canonical sampling through velocity rescaling. *J. Chem. Phys.* **2007**, *126*.

[62] Parrinello, M.; Rahman, A. Polymorphic transitions in single crystals: a new molecular dynamics method. *J. Appl. Phys.* **1981**, *52*, 7182–7190.

[63] MacKerell, A. D. et al. All-atom empirical potential for molecular modeling and dynamics studies of proteins. *J. Phys. Chem. B* **1998**, *102*, 3586–3616.

[64] Lu, T.; Chen, F. Multiwfn: A multifunctional wavefunction analyzer. *J. Comput. Chem.* **2012**, *33*, 580–592.

[65] Jorgensen, W. L.; Tirado-Rives, J. The OPLS potential functions for proteins. Energy minimizations for crystals of cyclic peptides and crambin. *J. Am. Chem. Soc.* **1988**, *110*, 1657–1666.

[66] Kaminski, G.; Duffy, E. M.; Matsui, T.; Jorgensen, W. L. Free energies of hydration and pure liquid properties of hydrocarbons from the OPLS all-atom model. *J. Phys. Chem.* **1994**, *98*, 13077–13802.

[67] Klauda, J. B.; Venable, R. M.; Freites, J. A.; O'Connor, J. W.; Tobias, D. J.; Mondragon-Ramirez, C.; Vorobyov, I.; MacKerell, A. D.; Pastor, R. W. Update of the CHARMM all-atom additive force field for lipids: Validation on six lipid types. *J. Phys. Chem. B* **2010**, *114*, 7830–7843.

[68] Pastor, R. W.; MacKerell, A. D. Development of the CHARMM force field for lipids. *J. Phys. Chem. Lett.* **2011**, *2*, 1526–1532.

[69] Jorgensen, W. L.; Chandrasekhar, J.; Madura, J. D.; Impey, R. W.; Klein, M. L. Comparison of simple potential functions for simulating liquid water. *J. Chem. Phys.* **1983**, *79*, 926–935.

[70] Abel, S. Stéphane Abel's homepage, downloads, equilibrated AOT reverse micelle. 2011; http://st-abel.com/downloads.htm.

[71] Abascal, J. L.; Vega, C. A general purpose model for the condensed phases of water: TIP4P/2005. *J. Chem. Phys.* **2005**, *123*.

[72] Jorgensen, W. L.; Maxwell, D. S.; Tirado-Rives, J. Development and testing of the OPLS all-atom force field on conformational energetics and properties of organic liquids. *J. Am. Chem. Soc.* **1996**, *118*, 11225–11236.

[73] Canongia Lopes, J. N.; Pádua, A. A.; Shimizu, K. Molecular force field for ionic liquids IV: Trialkylimidazolium and alkoxycarbonyl-imidazolium cations; alkylsulfonate and alkylsulfate anions. *J. Phys. Chem. B* **2008**, *112*, 5039–5046.

[74] Ríos-López, M.; Mendez-Bermúdez, J. G.; Domínguez, H. New force field parameters for the sodium dodecyl sulfate and alpha olefin sulfonate anionic surfactants. *J. Phys. Chem. B* **2018**, *122*, 4558–4565.

[75] Borioni, J. L.; Puiatti, M.; Vera, D. M. A.; Pierini, A. B. In search of the best DFT functional for dealing with organic anionic species. *Phys. Chem. Chem. Phys.* **2017**, *19*, 9189–9198.

[76] Schmidt, M. W.; Baldridge, K. K.; Boatz, J. A.; Elbert, S. T.; Gordon, M. S.; Jensen, J. H.; Koseki, S.; Matsunaga, N.; Nguyen, K. A.; Su, S.; Windus, T. L.; Dupuis, M.; Montgomery Jr., J. A. General atomic and molecular electronic structure system. *J. Comput. Chem.* **1993**, *14*, 1347–1363.

[77] Gordon, M. S.; Schmidt, M. W. In *Theory and Applications of Computational Chemistry: the First Forty Years*; Dykstra, C. E., Frenking, G., Kim, K. S., Scuseria, G. E., Eds.; Elsevier, 2005; pp 1167–1189.

[78] Marenich, A. V.; Jerome, S. V.; Cramer, C. J.; Truhlar, D. G. Charge model 5: An extension of Hirshfeld population analysis for the accurate description of molecular interactions in gaseous and condensed phases. *J. Chem. Theory Comput.* **2012**, *8*, 527–541.

[79] Bayly, C. I.; Cieplak, P.; Cornell, W. D.; Kollman, P. A. A well-behaved electrostatic potential based method using charge restraints for deriving atomic charges: The RESP model. *J. Phys. Chem.* **1993**, *97*, 10269–10280.

[80] Martínez, L.; Andrade, R.; Birgin, E. G.; Martínez, J. M. PACKMOL: A package for building initial configurations for molecular dynamics simulations. *J. Comput. Chem.* **2009**, *30*, 2157–2164.

[81] Abraham, M. J.; Murtola, T.; Schulz, R.; Páll, S.; Smith, J. C.; Hess, B.; Lindah, E. GROMACS: High performance molecular simulations through multi-level parallelism from laptops to supercomputers. *SoftwareX* **2015**, *1-2*, 19–25.

[82] Darden, T.; York, D.; Pedersen, L. Particle mesh Ewald: An $N \cdot log(N)$ method for Ewald Sums in large systems. *J. Chem. Phys.* **1993**, *98*, 10089–10092.

[83] Willard, A. P.; Chandler, D. Instantaneous liquid interfaces. *J. Phys. Chem. B* **2010**, *114*, 1954–1958.

[84] Michaud-Agrawal, N.; Denning, E. J.; Woolf, T. B.; Beckstein, O. MDAnalysis: A toolkit for the analysis of molecular dynamics simulations. *J. Comput. Chem.* **2011**, *32*, 2319–2327.

[85] Gowers, R. J.; Linke, M.; Barnoud, J.; Reddy, T. J.; Melo, M. N.; Seyler, S. L.; Domański, J.; Dotson, D. L.; Buchoux, S.; Kenney, I. M.; Beckstein, O. MDAnalysis: A Python package for the rapid analysis of molecular dynamics simulations. Proceedings of the 15th Python in Science Conference. 2016; pp 98–105.

[86] Sega, M.; Hantal, G.; Fábián, B.; Jedlovszky, P. Pytim: A python package for the interfacial analysis of molecular simulations. *J. Comput. Chem.* **2018**, *39*, 2118–2125.

[87] Sullivan, C.; Kaszynski, A. PyVista: 3D plotting and mesh analysis through a streamlined interface for the Visualization Toolkit (VTK). *J. Open Source Softw.* **2019**, *4*, 1450.

[88] Gale, C. D.; Derakhshani-Molayousefi, M.; Levinger, N. E. How to think about Shape. https://github.com/Levinger-Group/How-to-think-about-Shape, 2022.

[89] Tanaka, R.; Okazaki, K. Apparent dipole moments of aerosol OT reversed micelles in cyclohexane determined at a frequency of 1 MHz and at a temperature of 298.15 K. *JOURNAL OF COLLOID AND INTERFACE SCIENCE* **1996**, *184*, 601–606.

[90] Historical profile: August Kekulé and Archibald Scott Couper. 2017; https://www.sciencehistory.org/historical-profile/august-kekule-and-archibald-scott-couper.

[91] Robinson, A. Chemistry's visual origins. *Nature* **2010**, *465*, 36.

[92] Rocke, A. J. *Image and reality: Kekule, Kopp, and the scientific imagination*; University of Chicago Press, 2010; p 416.

[93] Ferry, G. History: Women in crystallography. *Nature* **2014**, *505*, 609–611.

[94] Watson, J.; Crick, F. Molecular Structure of Nucleic Acids: A Structure for Deoxyribose Nucleic Acid. *Nature* **1953**, *171*, 737–738.

[95] Hodgkin, D. C. The X-ray analysis of the structure of penicillin. *Adv. Sci.* **1949**, *6*, 85–89.

[96] Slabinski, L.; Jaroszewski, L.; Rodrigues, A. P.; Rychlewski, L.; Wilson, I. A.; Lesley, S. A.; Godzik, A. The challenge of protein structure determination—lessons from structural genomics. *Prot. Sci.* **2007**, *16*, 2472–2482.

[97] Moraes, I.; Evans, G.; Sanchez-Weatherby, J.; Newstead, S.; Stewart, P. D. Membrane protein structure determination - The next generation. *Biochim. Biophys. Acta, Biomembr.* **2014**, *1838*, 78–87.

[98] Nogales, E.; Mahamid, J. Bridging structural and cell biology with cryo-electron microscopy. *Nature* **2024**, *628*, 47–56.

[99] Cotton, F. A. *Chemical Applications of Group Theory*, 3rd ed.; Wiley-Interscience, 1990.

[100] Zhou, B.; Wang, J.; Zhao, B. Micromorphology characterization and reconstruction of sand particles using micro X-ray tomography and spherical harmonics. *Eng. Geol.* **2015**, *184*, 126–137.

[101] Garboczi, E. J.; Bullard, J. W. 3D analytical mathematical models of random star-shape particles via a combination of X-ray computed microtomography and spherical harmonic analysis. *Adv. Powder Technol.* **2017**, *28*, 325–339.

[102] Ayoub, A. B. The eccentricity of a conic section. *Coll. Math. J.* **2003**, *34*, 116–121.

[103] Kepler, J. *Astronomia Nova*; 1609.

[104] Rawat, N.; Biswas, P. Size, shape, and flexibility of proteins and DNA. *J. Chem. Phys.* **2009**, *131*, 165104–165113.

[105] Nave, S.; Eastoe, J.; Heenan, R. K.; Steytler, D.; Grillo, I. What is so special about aerosol-OT? Part II. Microemulsion systems. *Langmuir* **2000**, *16*, 8741–8748.

[106] Nave, S.; Eastoe, J.; Heenan, R. K.; Steytler, D.; Grillo, I. What is so special about aerosol-OT? Part III. Glutaconate versus sulfosuccinate headgroups and oil-water interfacial tensions. *Langmuir* **2002**, *18*, 1505–1510.

[107] Chatterjee, K.; Sarkar, S.; Rao, K. J.; Paria, S. Core/shell nanoparticles in biomedical applications. *Adv. Colloid Interface Sci.* **2014**, *209*, 8–39.

[108] Gawande, M. B.; Goswami, A.; Asefa, T.; Guo, H.; Biradar, A. V.; Peng, D. L.; Zboril, R.; Varma, R. S. Core-shell nanoparticles: synthesis and applications in catalysis and electrocatalysis. *Chem. Soc. Rev.* **2015**, *44*, 7540–7590.

[109] Chen, X.; Peng, D.; Ju, Q.; Wang, F. Photon upconversion in core-shell nanoparticles. *Chem. Soc. Rev.* **2015**, *44*, 1318–1330.

[110] Ferrando, R. Symmetry breaking and morphological instabilities in core-shell metallic nanoparticles. *J. Condens. Matter Phys.* **2015**, *27*.

[111] Haag, R. Supramolecular Drug-Delivery Systems Based on Polymeric Core-Shell Architectures. *Angew. Chem., Int. Ed. Engl.* **2004**, *43*, 278–282.

[112] Chu, Z.; Dreiss, C. A.; Feng, Y. Smart wormlike micelles. *Chem. Soc. Rev.* **2013**, *42*, 7174–7203.

[113] Wubshet, N. H.; Liu, A. P. Methods to mechanically perturb and characterize GUV-based minimal cell models. *Comput. Struct. Biotechnol. J.* **2023**, *21*, 550–562.

[114] Lu, W.; Guo, X.; Luo, Y.; Li, Q.; Zhu, R.; Pang, H. Core-shell materials for advanced batteries. *Chem. Eng. J.* **2019**, *355*, 208–237.

[115] Ansari, N.; Laio, A.; Hassanali, A. Spontaneously Forming Dendritic Voids in Liquid Water Can Host Small Polymers. *J. Phys. Chem. Lett.* **2019**, *10*, 5585–5591.

[116] Basilevsky, M. V.; Parsons, D. F. An advanced continuum medium model for treating solvation effects: Nonlocal electrostatics with a cavity. *J. Chem. Phys.* **1996**, *105*, 3734–3746.

[117] Li, L.; Li, C.; Zhang, Z.; Alexov, E. On the dielectric ”constant” of proteins: Smooth dielectric function for macromolecular modeling and its implementation in DelPhi. *J. Chem. Theory Comput.* **2013**, *9*, 2126–2136.

[118] Lake, P. T.; Mattson, M. A.; McCullagh, M. Implicit Solvation Using the Superposition Approximation (IS-SPA): Extension to Peptides in a Polar Solvent. *J. Chem. Theory Comput.* **2021**, *17*, 703–713.

[119] Hvidsten, T. R.; Lægreid, A.; Kryshtafovych, A.; Anderson, G.; Fidelis, K.; Komorowski, J. A comprehensive analysis of the structure-function relationship in proteins based on local structure similarity. *PLoS One* **2009**, *4*.

[120] Mabrouk, M.; Hammad, S. F.; Abdella, A. A.; Mansour, F. R. Tips and tricks for successful preparation of molecularly imprinted polymers for analytical applications: A critical review. *Microchem. J.* **2023**, *193*, 109152.

[121] Resina, L.; Alemán, C.; Ferreira, F. C.; Esteves, T. Protein-imprinted polymers: How far have "plastic antibodies" come? *Biotechnol. Adv.* **2023**, *68*, 108220.

[122] Klein, W. P.; Schmidt, C. N.; Rapp, B.; Takabayashi, S.; Knowlton, W. B.; Lee, J.; Yurke, B.; Hughes, W. L.; Graugnard, E.; Kuang, W. Multiscaffold DNA origami nanoparticle waveguides. *Nano Lett.* **2013**, *13*, 3850–3856.

[123] Parsons, M. F.; Allan, M. F.; Li, S.; Shepherd, T. R.; Ratanalert, S.; Zhang, K.; Pullen, K. M.; Chiu, W.; Rouskin, S.; Bathe, M. 3D RNA-scaffolded wireframe origami. *Nat. Commun.* **2023**, *14*, 382–396.

[124] Flor, B.; Zeman, C. J.; Ma, X.; Schatz, G. C. Wavelength-Dependent Spin Excitation with Circularly Polarized Light in CdSe Nanoplatelets. *J. Phys. Chem. C* **2023**, *127*, 14317–14325.

[125] Vargas-Consuelos, C. I.; Camacho-López, M. A.; Ramos-Sanchez, V. H.; Graeve, O. A. Phase and Morphology Control of Hexagonal MoO3 Crystals via Na+ Interactions: A Raman Spectroscopy Study. *J. Phys. Chem. C* **2023**, *127*, 13136–13148.

[126] Qiao, S.; Novitskaya, E.; Ren, T.; Pena, G.; Graeve, O. A. Phase and Morphology Control of Magnesium Nanoparticles via Lithium Doping. *Cryst. Growth Des.* **2019**, *19*, 3626–3632.

[127] Ren, T.; Tran, R.; Lee, S.; Bandera, A.; Herrera, M.; Li, X. G.; Ong, S. P.; Graeve, O. A. Morphology Control of Tantalum Carbide Nanoparticles through Dopant Additions. *J. Phys. Chem. C* **2021**, *125*, 10665–10675.

[128] Schönfeldová, T.; Dupertuis, N.; Chen, Y.; Ansari, N.; Poli, E.; Wilkins, D. M.; Hassanali, A.; Roke, S. Charge Gradients around Dendritic Voids Cause Nanoscale Inhomogeneities in Liquid Water. *J. Phys. Chem. Lett* **2022**, *13*, 7462–7468.

[129] Skiena, S. S. *The Algorithm Design Manual*; Springer-Vrlag: New York, 1997; Chapter 8.6.16, pp 395–396.

[130] Žunić, J.; Rosin, P. A convexity measurement for polygons. Proceedings of the British Machine Vision Conference. 2002; pp 173–182.

[131] Braga, C.; Smith, E. R.; Nold, A.; Sibley, D. N.; Kalliadasis, S. The pressure tensor across a liquid-vapour interface. *J. Chem. Phys.* **2018**, *149*.

[132] Sodt, A. J.; Pastor, R. W. The tension of a curved surface from simulation. *J. Chem. Phys.* **2012**, *137*.

[133] Kreyszig, E. *Differential Geometry*; Dover Publications: New York, 1991; Chapter Chapter II, pp 34–36.

[134] Gray, A. *Modern Differential Geometry of Curves and Surfaces with Mathematica*, 2nd ed.; CRC Press: Boca Raton, 1997; Chapter The Gaussian and mean curvatures, pp 373–380.

[135] Barber, C. B.; Dobkin, D. P.; Huhdanpaa, H. The quickhull algorithm for convex hulls. *ACM Trans. Math. Softw.* **1996**, *22*, 469–483.

[136] Pieniazek, P. A.; Lin, Y. S.; Chowdhary, J.; Ladanyi, B. M.; Skinner, J. L. Vibrational spectroscopy and dynamics of water confined inside reverse micelles. *Journal of Physical Chemistry B* **2009**, *113*, 15017–15028.

[137] Biswas, R.; Chakraborti, T.; Bagchi, B.; Ayappa, K. G. Non-monotonic, distance-dependent relaxation of water in reverse micelles: Propagation of surface induced frustration along hydrogen bond networks. *J. Chem. Phys.* **2012**, *137*.

[138] Berezin, M. Y.; Achilefu, S. Fluorescence lifetime measurements and biological imaging. *Chem. Rev.* **2010**, *110*, 2641–2684.

[139] Piskulich, Z. A.; Thompson, W. H. The activation energy for water reorientation differs between IR pump-probe and NMR measurements. *J. Chem. Phys.* **2018**, *149*, 164504.

[140] Piskulich, Z. A.; Laage, D.; Thompson, W. H. Activation energies and the extended jump model: How temperature affects reorientation and hydrogen-bond exchange dynamics in water. *J. Chem. Phys.* **2020**, *153*, 74110.

[141] Mark, P.; Nilsson, L. Structure and dynamics of the TIP3P, SPC, and SPC/E water models at 298 K. *J. Phys. Chem. A* **2001**, *105*, 9954–9960.

[142] Vega, C.; Abascal, J. L. Simulating water with rigid non-polarizable models: A general perspective. *Phys. Chem. Chem. Phys.* **2011**, *13*, 19663–19688.

[143] Scodinu, A.; Fourkas, J. T. Comparison of the orientational dynamics of water confined in hydrophobic and hydrophilic nanopores. *J. Phys. Chem. B* **2002**, *106*, 10292–10295.

[144] Farrer, R. A.; Fourkas, J. T. Orientational dynamics of liquids confined in nanoporous sol-gel glasses studied by optical Kerr effect spectroscopy. *Acc. Chem. Res.* **2003**, *36*, 605–612.

[145] Laage, D.; Thompson, W. H. Reorientation dynamics of nanoconfined water: Power-law decay, hydrogen-bond jumps, and test of a two-state model. *Journal of Chemical Physics* **2012**, *136*.

[146] Berg, M. A.; Darvin, J. R. Measuring a hidden coordinate: Rate-exchange kinetics from 3D correlation functions. *J. Chem. Phys.* **2016**, *145*.

[147] Berg, M. A.; Kaur, H. Nonparametric analysis of nonexponential and multidimensional kinetics. I. Quantifying rate dispersion, rate heterogeneity, and exchange dynamics. *J. Chem. Phys.* **2017**, *146*.

[148] Allen, M.; Tildesley, D. *Computer Simulation of Liquids*, 1st ed.; Oxford University Press: New York, NY, 1987.

[149] Ben-Naim, A. *Statistical Thermodynamics for Chemists and Biochemists*; Springer: New York, NY, 1992; p 697.

[150] Babin, V.; Medders, G. R.; Paesani, F. Development of a ”first principles” water potential with flexible monomers. II: Trimer potential energy surface, third virial coefficient, and small clusters. *J. Chem. Theory Comput.* **2014**, *10*, 1599–1607.

[151] Reddy, S. K.; Straight, S. C.; Bajaj, P.; Huy Pham, C.; Riera, M.; Moberg, D. R.; Morales, M. A.; Knight, C.; Götz, A. W.; Paesani, F. On the accuracy of the MB-pol many-body potential for water: Interaction energies, vibrational frequencies, and classical thermodynamic and dynamical properties from clusters to liquid water and ice. *J. Chem. Phys.* **2016**, *145*.

[152] Nave, S.; Paul, A.; Eastoe, J.; Pitt, A. R.; Heenan, R. K. What is so special about aerosol-OT? Part IV. Phenyl-tipped surfactants. *Langmuir* **2005**, *21*, 10021–10027.

[153] Zulauf, M.; Eicke, H. F. Inverted micelles and microemulsions in the ternary system H2O/aerosol-OT/isooctane as studied by photon correlation spectroscopy. *J. Phys. Chem.* **1979**, *83*, 480–486.

[154] Melo, E. P.; Fojan, P.; Cabral, J. M.; Petersen, S. B. Dynamic light scattering of cutinase in AOT reverse micelles. *Chem. Phys. Lipids* **2000**, *106*, 181–189.

[155] Stover, C. Invertible Matrix Theorem. 2023; https://mathworld.wolfram.com/InvertibleMatrixTheorem.html.

[156] Tzioumis, K. K. Data Descriptor: Demographic aspects of first names. *Nature: Scientific Data* **2018**, 1–9.

Appendix A

Author Contributions for Published Work

For Ref. 1, author contributions were:

Conceptualization, C.D.G.; Methodology, C.D.G., M.D-M.; Software, C.D.G.; Formal Analysis, C.D.G.; Investigation, C.D.G.; Resources, N.E.L.; Data Curation, C.D.G.; Writing- Original Draft, C.D.G.; Writing- Review and Editing, N.E.L., C.D.G., M.D-M.; Visualization, C.D.G.; Supervision, N.E.L., Funding Acquisition, N.E.L.

For Ref. 2, author contributions were:

Conceptualization, C.D.G.; Methodology, C.D.G.; Software, C.D.G.; Formal Analysis, C.D.G.; Investigation, C.D.G.; Resources, N.E.L.; Data Curation, C.D.G.; Writing- Original Draft, C.D.G.; Writing- Review and Editing, N.E.L., C.D.G.; Visualization, C.D.G.; Supervision, N.E.L., Funding Acquisition, N.E.L.

For Ref. 3, author contributions were:

Conceptualization, C.D.G.; Methodology, C.D.G., M.D-M.; Software, C.D.G.; Formal Analysis, C.D.G.; Investigation, C.D.G.; Resources, N.E.L.; Data Curation, C.D.G.; Writing- Original Draft, C.D.G.; Writing- Review and Editing, N.E.L., C.D.G., M.D-M.; Visualization, C.D.G.; Supervision, N.E.L., Funding Acquisition, N.E.L.

Appendix B

Model and Proof for the Change in CPE as a Shell is Grown

B.1 Introductory Notes

In this appendix, I develop the mathematics underlying my model for a core/shell type shape and then developing a proof in two parts examining if and when the CPE will change within this model and when it does change, whether it will rise or fall. There is also a brief overture for this proof provided, which while not rigorous, provides a quick and elegant view of the problem and solution that I provide in the hopes of helping to provide readers with an intuitive view of the problem. The rigorous proof adopts a different approach in order to determine under what conditions the CPE will change (or rather the discrete number of conditions under which it will not change) as well as to provide a method for determining the monotonicity of the change.

Note that the proof has been written in the format that it is following peer-review. In general it was found that while many people already had a good understanding of several of the concepts presented in this work, this was not universal. Because this is written for a broad audience and because certain topics like set theory are not part of the standard chemistry curriculum, I have provided several notes and definitions for those who are unfamiliar with the topics. I hope that experienced and knowledgeable readers will understand that a balance had to be struck between an economy of words and equations and accessibility to a broader audience.

B.2 Math Notation

- Set notation: curly brackets {} indicate a set, which is just a collection of things. The symbol $\in$ is read as "in" and indicates that the variable on the left is a part of the set on the right. For example, we use $x \in \{b, c\}$, which is read as "x in the set: b, c". This means that x can be either b or c.

- The real numbers are indicated by the symbol $\mathbb{R}$. A plus sign indicates the positive reals, $\mathbb{R}^+$.

- The symbol $\iff$ indicates "if and only if". So that the statement on the left is true if and only if the statement on the right is also true, and vice versa.

- The notation $\boldsymbol{u} \,||\, \boldsymbol{v}$ indicates that the vector $\boldsymbol{u}$ is parallel to the vector $\boldsymbol{v}$.

B.3 Language

- Moments of Inertia - For simplicity, we use "moments of inertia" to refer to the principal moments of inertia of an object.

- Coordinate-Pair Eccentricity (CPE) - While the CPE is composed of two values with an infinite set of solutions in 2D space, we refer to them as a singular value for simplicity. Due to the symmetry of the CPE's construction, the same logic that applies to one value applies to the other so everything that happens to one must also happen to the other.

- Measures of Shape - The language surrounding shape is slightly confusing. We are working with a generalized model of shape, *e.g.* an ellipsoidal shape, or a rod shape, *etc*. All of these models substantially differ in how many measures of shape are required to describe them. Although a solid sphere has one radius, a rod has both a radius and a length, *etc*. To unify the language, we refer to these collectively as "measures of shape".

- Prolate/Oblate/Spherical - We use the CPE to characterize an arbitrary shape into the categories of “mostly-prolate”, “mostly-oblate”, and “mostly-spherical”. Because we are working in loose approximations that are better described by a pair of numbers (CPE) rather than a qualitative name, it is convenient to simply state that these shapes are prolate, oblate, or spherical and omit the “mostly” modifier. To distinguish a shape that is only “mostly” prolate ($a > b \approx c$) from a formally, mathematically defined prolate ellipsoid ($a > b = c$), we define the latter as “perfectly prolate”.
- Apparent Semiaxes - Our CPE metric relies on finding an ellipsoid that rotates identically to the shape of interest by equating the moments of inertia we measure to the moments of inertia of an ellipsoid. Therefore, there is a hypothetical ellipsoid that represents other shape and that is used to compute CPE. We refer to the semiaxes of this hypothetical ellipsoid as the “apparent semiaxes” for clarity. That is, if an ellipsoid is used as the basis shape for this model, then there would be both the semiaxes of the real ellipsoid, and the apparent semiaxes of the hypothetical ellipsoid.
- Inner/Outer Surface - This work examines how the properties of a shape change as the shape grows and implicitly implies an original shape and a larger resulting shape after this “growth”. The “inner” surface is the original surface of the shape, and the “outer” surface is the surface after the addition of some constant to all measures of shape.

B.4 Model

We construct a model of shape as follows. First, we assume an arbitrary shape whose moments of inertia can be computed with a linear function of the form:

$$\boldsymbol{M} = \overleftrightarrow{\boldsymbol{C}}\boldsymbol{S} \tag{B.1}$$

where $\boldsymbol{M}$ is a vector representation of the principal moments of inertia, $\boldsymbol{S}$ is a vector representation of the measures of shape, and $\overleftrightarrow{\boldsymbol{C}}$ is a tensor derived from the system of equations used to compute the moments of inertia. Note that this tensor will always include the mass of the object and usually some scalar as well. As scalars, these quantities can be factored out of the tensor as needed because this is a linear transformation. This shape is considered the "inner" shape.

We then construct an outer surface by adding a constant, t, to all measures of shape, thus creating an "outer" shape, larger than the initial inner shape. We are then concerned with measuring the CPE of both the inner and outer shapes, determining if the CPE changes, and if so, how the CPE changes. We assume that the shape is such that adding a constant to all measures of shape results in an object that is larger by the constant, t along all points normal to the inner surface if the two surfaces are arranged to share the same center of mass. This requirement limits the possible shapes to include only those shapes that are topological balls and does not include shapes like a torus, because a torus would only fit this construction if the constant t were added to only one of the two measures of shape, the minor radius.

Broadly, the model creates a constant thickness (t) around the inner shape and is a good approximation of how shape changes when something like a surfactant layer is added. However, the assumption of a constant thickness everywhere is not strictly true, particularly around corners. A truly constant thickness everywhere would require rounding around corners, which adding a constant to the measures of shape does not do. This is because the inner and outer surface around a right angle corner, for example, creates right triangles so that the distance from the inner corner to outer corner is actually $\sqrt{2}t$. However, there is no surface normal at the corner

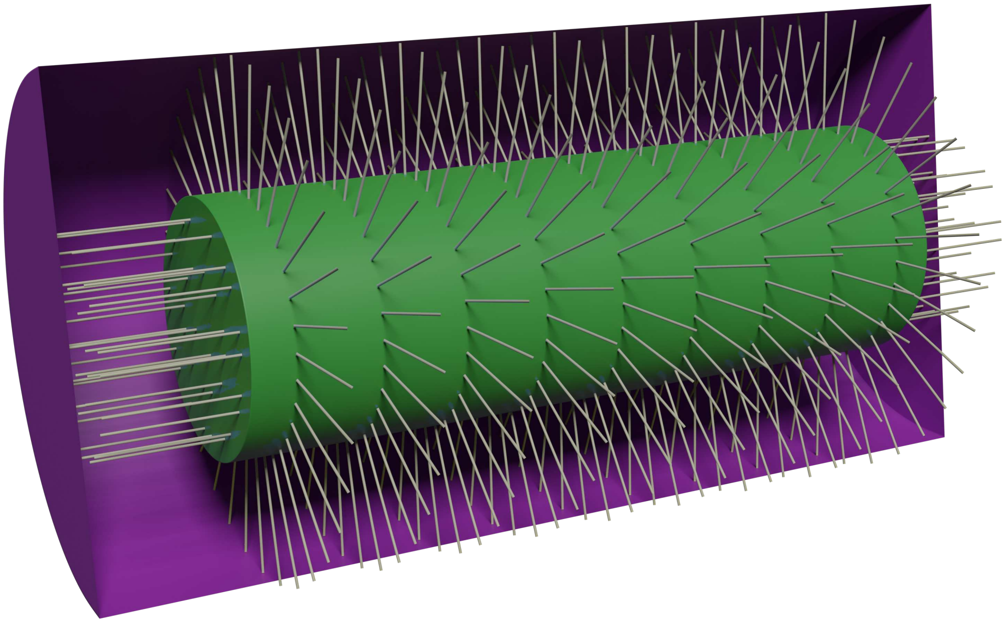

Figure B.1: The green cylinder represents the core while the purple cylinder represents the shell (shown as a cutaway). The "hairs" shown in gray represent the additional thickness added to the measures of shape of the core cylinder to create the shell cylinder. This is why the hairs are oriented as shown: extending radial around the length to extend the radius, and normal along the flat ends to extend the length.

(corners are not differentiable), so it is still true that this model creates a constant thickness everywhere normal to the surface. Additionally, the proof we develop here assumes that equation B.1 is linear, as shown. This effectively limits us to simple, regular shapes such as spheres, cylinders, rectangular prisms, *etc*. A truly amorphous shape does not have a precise mathematical description so this model does not apply.

Note that all measures used here are measurable quantities and therefore can be assumed to be in the positive real numbers. Additionally, this model assumes that all shapes have a constant density, which is generally a useful assumption in most chemical systems. An example of our model is shown in Figure B.1, showing the case of a cylindrical object.

B.5 Overture

In this work we examine how the CPE changes when a constant is added to all measures of shape to make a larger outer surface. There are two questions we must ask and examine. First, does our model lead to a change in the CPE between the inner and outer surfaces at all? And second, if it does change CPE, then how does CPE change? We show that, in our model, the CPE must change except in certain, limited circumstances. We are then able to show that when the CPE does change, it will always decrease.

There is a rather elegant, although not strictly rigorous demonstration of our findings that CPE changes as a layer "grows" onto it using Minkowski sums that we review here to preview our findings. For a Minkowski sum, consider two shapes, A and B, defined as the set of all vectors with endpoints on or within some arbitrary surface centered on the origin. The Minkowski sum is then given by:

$$A + B = \{\boldsymbol{a} + \boldsymbol{b} \,|\, \boldsymbol{a} \in A, \boldsymbol{b} \in B\} \tag{B.2}$$

which states that the Minkowski sum, $A + B = C$, is the set given by the sum of all vectors $\boldsymbol{a}$ in shape A and all vectors $\boldsymbol{b}$ in shape B[129]. This is demonstrated in Figure B.2 for an arbitrary polygon and a circle. Notice that this operation is essentially equivalent to translating the circle, B, around all points on and within the shape, A. This creates a shape that is larger by exactly the radius of the circle and which has rounded corners.

Our model is nearly perfectly reproduced by the the Minkowski sum of our arbitrary shape and a sphere whose radius is equal to the constant we would like to add. Our model only differs in the behavior around corners. Now let us imagine what happens as the outer surface increases by the distance equivalent to the radius of the cir-

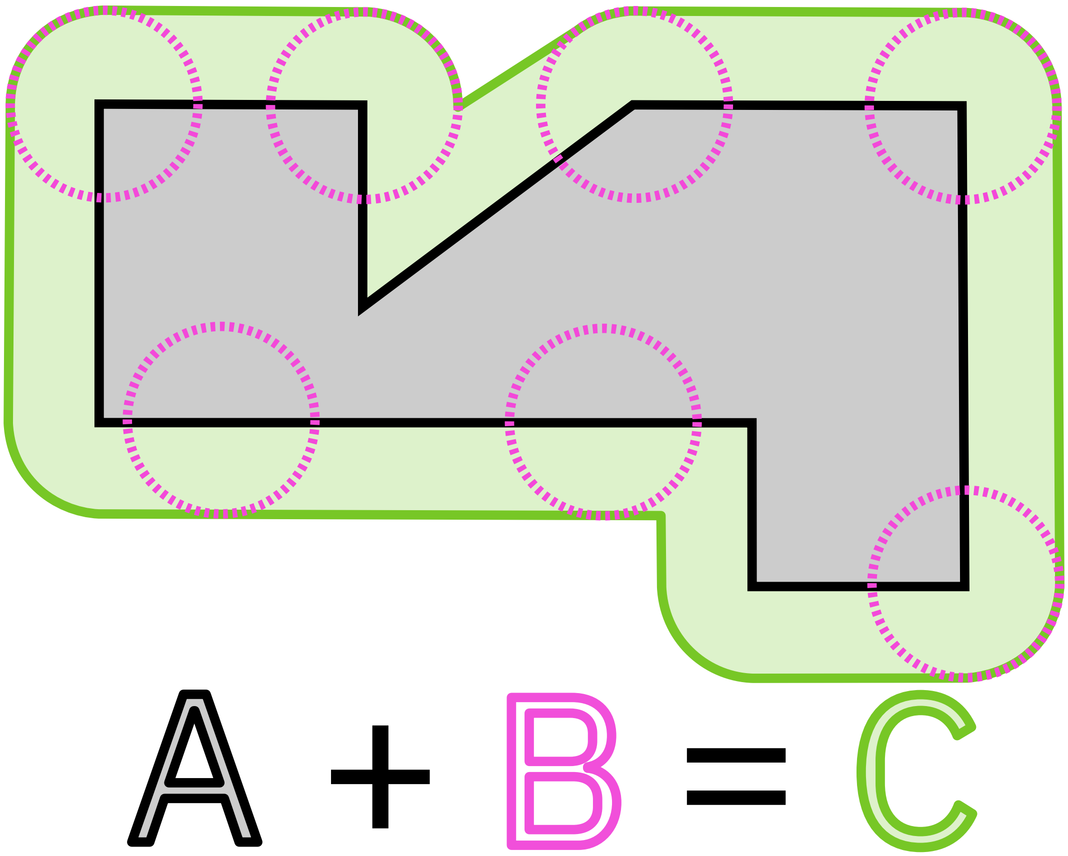

Figure B.2: Demonstration of Minkowski sum between the gray polygon, A, and the pink circle, B, to create the new, green shape, C.

cle, B in Figure B.2, or a sphere in our 3D case. As the circle or sphere becomes much larger than the original shape, the Minkowski sum will begin to resemble the circle or sphere more and more until, in the limit of an infinitly large circle/sphere, the shape simply becomes circular/spherical. So it is straightforward to demonstrate that the CPE should generally change and it will always decrease (the shape becomes relatively more spherical). Unfortunately, Minkowski sums do not offer a rigorous proof but they should provide the reader with a general understanding of what this proof does and some intuition as to why this proof works.

B.6 Mathematical Construction of the Model

Let $\boldsymbol{S}$ be a matrix containing the measures of shape, such that:

$$\boldsymbol{S} = \begin{bmatrix} S_1 \\ \vdots \\ S_n \end{bmatrix} \tag{B.3}$$

where S_n represents as many or as few measures as required to describe a given shape; the matrix has shape $(n \times 1)$. As far as we are aware, all of the tabulated equations to compute the moments of inertia use the square of the measures of shape, *e.g.* $s_n = r^2$, where r is the radius of some shape. However, the proof given here requires only that the moments of inertia be expressible as a system of linear equations and is therefore not limited to these tabulated equations. For example, a sphere may be represented by equation B.4, while a cylinder may be represented by equation B.5.

$$\boldsymbol{S}_{sph} = \begin{bmatrix} r^2 \end{bmatrix} \tag{B.4}$$

$$\boldsymbol{S}_{cyl} = \begin{bmatrix} r^2 \\ L^2 \end{bmatrix} \tag{B.5}$$

In this model, we examine the changes in shape between an inner and outer surface. So let $\boldsymbol{S}$ represent the measures of shape for the inner surface, and $\boldsymbol{S}'$ represent the measures of shape for the outer surface. The new measures of shape for the outer surface are found by adding a constant, $t \in \mathbb{R}^+$. We make no assumptions as to the form of the specific equations, so we simply note that there exists a vector, $\boldsymbol{S}'$, that can be computed in this manner, and that the elements of $\boldsymbol{S}'$ are strictly greater than the elements of $\boldsymbol{S}$. For the examples given above, the outer surfaces' measures of shapes may be written as:

$$\begin{aligned} \boldsymbol{S}'_{sph} &= \begin{bmatrix} (r+t)^2 \end{bmatrix} \\ \boldsymbol{S}'_{sph} &= \boldsymbol{S}_{sph} + \begin{bmatrix} 2rt + t^2 \end{bmatrix} \end{aligned} \tag{B.6}$$

$$\begin{aligned} \boldsymbol{S}'_{cyl} &= \begin{bmatrix} (r+t)^2 \\ (L+t)^2 \end{bmatrix} \\ \boldsymbol{S}'_{cyl} &= \boldsymbol{S}_{cyl} + \begin{bmatrix} 2rt + t^2 \\ 2Lt + t^2 \end{bmatrix} \end{aligned} \tag{B.7}$$

Even though there is a square in the measures of shape, $\boldsymbol{S}'$ can be separated into $\boldsymbol{S}$ plus some matrix containing t, which ensures that equation B.1 is still linear.

The moments of inertia tensor for an ellipsoid is given as:

$$\boldsymbol{M}_e = \begin{bmatrix} I_C \\ I_B \\ I_A \end{bmatrix} = \frac{m}{5} \begin{bmatrix} 0 & 1 & 1 \\ 1 & 0 & 1 \\ 1 & 1 & 0 \end{bmatrix} \begin{bmatrix} c^2 \\ b^2 \\ a^2 \end{bmatrix} \tag{B.8}$$

where I_A, I_B, and I_C represent the moments of inertia rotating about the direction of the semiaxes a, b, and c, respectively, and m is the mass of the ellipsoid. As a reminder, convention establishes that $a \geq b \geq c$ and therefore $I_C \geq I_B \geq I_A$. It is straightforward to show that $det\left(\overleftrightarrow{\boldsymbol{C}_e}\right) = 2$ and therefore $\overleftrightarrow{\boldsymbol{C}_e}$ is invertible by the invertible matrix theorem[155].

We then solve for the apparent semiaxes, $\boldsymbol{S}'_e$.

$$\begin{aligned} \overleftrightarrow{\boldsymbol{C}}' \boldsymbol{S}' &= \overleftrightarrow{\boldsymbol{C}_e}' \boldsymbol{S}'_e \\ \left(\overleftrightarrow{\boldsymbol{C}_e}'\right)^{-1} \overleftrightarrow{\boldsymbol{C}}' \boldsymbol{S}' &= \boldsymbol{S}'_e \end{aligned} \tag{B.9}$$

Note that $\overleftrightarrow{\boldsymbol{C}_e} = \overleftrightarrow{\boldsymbol{C}_e}'$ and $\overleftrightarrow{\boldsymbol{C}} = \overleftrightarrow{\boldsymbol{C}}'$ because these represent the tensors used to compute the moments of inertia and are not functions of the measures of shape. The CPE can then be computed using:

$$e'_{ax} = \sqrt{1 - \frac{x^2}{a^2}} = \sqrt{1 - \frac{\boldsymbol{S}'_{e,x}}{\boldsymbol{S}'_{e,a}}} \qquad \text{for } x \in \{b, c\} \tag{B.10}$$

B.7 CPE Changes with a Constant Increase in the Measures of Shape

In this section, we demonstrate that the CPE must change as the measures of shape increase except for in a few, discrete cases that we examine in more detail below. Because there are infinite cases where the CPE changes and only a few cases where it does not, we start with the latter case. We develop a condition that must be true for the CPE to remain constant and then consider the situations in which this Static CPE Condition is true, which implies that in all other cases, the CPE must change.

Developing the Static CPE Condition Where the CPE Does Not Change

Equation B.10 above implies that the CPE values, e_{ax}, will remain unchanged ($e'_{ax} = e_{ax}$), if and only if:

$$e'_{ax} = e_{ax} \qquad \Longleftrightarrow \qquad \frac{S'_{e,x}}{S'_{e,a}} = \frac{S_{e,x}}{S_{e,a}} \tag{B.11}$$

And consequently:

$$\frac{S'_{e,x}}{S'_{e,a}} = \frac{S_{e,x}}{S_{e,a}} \qquad \Longleftrightarrow \qquad \begin{cases} S'_{e,a} = \alpha S_{e,a} \\ S'_{e,x} = \alpha S_{e,x} \end{cases} \qquad \text{for } \alpha \in \mathbb{R}^+ \tag{B.12}$$

Practically Solving for the Static CPE Condition

To find the scalar factor relationship between the inner and outer surfaces, we can write equation B.13 without loss of generality:

$$S'_{e,y} = S_{e,y} + \varepsilon_y \qquad \text{for } y \in \{a, b, c\} \tag{B.13}$$

This also defines ε_y, as the “excess” apparent semiaxis length of the outer surface,

$$\varepsilon = \left(\overleftrightarrow{\boldsymbol{C}}_e'\right)^{-1} \overleftrightarrow{\boldsymbol{C}}' \left(\boldsymbol{S}' - \boldsymbol{S}\right) = \left(\overleftrightarrow{\boldsymbol{C}}_e'\right)^{-1} \overleftrightarrow{\boldsymbol{C}}' \left(\boldsymbol{S}_t\right) \tag{B.14}$$

where $\left(\boldsymbol{S}' - \boldsymbol{S}\right) = \boldsymbol{S}_t$ represents the impact of adding a constant to the measures of shape, that is, the linearly separable portion of the vector $\boldsymbol{S}'$. For example, in the case of the spherical demonstration, $\boldsymbol{S}_t = \left[2rt + t^2\right]$. Although $\boldsymbol{S}_t$ is created by the addition of a constant, t, the resulting excess, ε, will almost never be equal to t itself.

Although we can practically determine the amount by which each apparent semiaxis has changed as the addition of ε, our condition for determining if/when CPE changes, given in equation B.12, is written as a product. To connect these two formalisms, notice that the addition of some constant to a known value can be represented by multiplication of that known value by another constant, such that:

$$S_{e,y} + \varepsilon_y = \beta S_{e,y} \tag{B.15}$$

Therefore, the CPE will not change if and only if:

$$e'_{ax} = e_{ax} \qquad \Longleftrightarrow \qquad \beta_{y_1} = \beta_{y_2} = \alpha \qquad \text{for } y_1, y_2 \in \{a, b, c\}, y_1 \neq y_2 \tag{B.16}$$

The set of solutions to equation B.15 can be found by assuming β is constant, which defines the equation of a line along which the values of β are identical, as shown in equation B.17.

$$\varepsilon_y = (\beta - 1)\, S_{e,y} \tag{B.17}$$

Equation B.17 is only defined for single values, *i.e.* the value of β associated with a single apparent semiaxis, S_{e,y_1} and ε_{y_1}. In other words, for a typical arbitrary shape where the CPE changes, there will be three separate values of β such that $\beta_{y_1} \neq \beta_{y_2} \neq \beta_{y_3}$, and equation B.17 finds those three individual values. To find when those values are the same and the CPE does not change, we must find when two apparent semiaxes share the same value of β (such that $\beta_{y_1} = \beta_{y_2}$). To find this equivalency, we rewrite equation B.17 in terms of multiple components as:

$$e'_{ax} = e_{ax} \qquad \Longleftrightarrow \qquad \mathbf{Pr}_{ax}\left(\varepsilon\right) = (\alpha - 1)\, \mathbf{Pr}_{ax}\left(\boldsymbol{S}_e\right) \tag{B.18}$$

where $\mathbf{Pr}_{ax}\left(\boldsymbol{u}\right)$ denotes the projection of the vector $\boldsymbol{u}$ onto the plane ax ($x \in \{b, c\}$). Note that equation B.18 implicitly assumes that $\beta_{y_1} = \beta_{y_2}$ so we have substituted α to denote this equality, as per equations B.12 and B.16. Equation B.18 can be seen as finding when the projections of the vectors ε and $\boldsymbol{S}_e$ are parallel[7]. This means that equation B.18 is equivalent to asking if the ratio of semiaxis a to b is the same as the ratio of the amounts those semiaxes have grown by (the ratio of ε_a to ε_b), which is simply a restatement of equation B.12 and nicely confirms our derivation up to

---

[7] For those whose vector mechanics are rusty, remember that a projection of one vector onto a plane means the portion of that vector that is in the plane. For example, projection is often used in physics to decompose a force into the components normal and tangential to a surface. Because we are projecting onto a plane defined by the axes, projections is equivalent to setting to zero the component not involved. I.e., for some vector $\mathbf{u} = \langle a_1, b_1, c_1 \rangle$, then $\mathbf{Pr}_{ab}(\mathbf{u}) = \langle a_1, b_1, 0 \rangle$

this point. We ignore the *bc* plane because CPE only compares apparent semiaxes *a* to *b* and *a* to *c*. If apparent semiaxes *b* and *c* are equivalent, *e.g.* if equation B.18 is satisfied by projection onto the *bc* plane, then the shape is perfectly prolate ($a > b = c$) and $e_{ab} = e_{ac}$, even though the value of both are not known and may change. Although the shape may remain perfectly prolate, both values of CPE will still change.

Determining When Equation B.18 Is Satisfied

The question is, then, under what conditions will $\mathbf{Pr}_{ax}(\varepsilon)$ be parallel to $\mathbf{Pr}_{ax}(\boldsymbol{S}_e)$. It is useful to expand ε and $\boldsymbol{S}_e$ in terms of the original measures of shape as follows (substitutions from equations B.9 and B.13):

$$\mathbf{Pr}_{ax}\left(\left(\overleftrightarrow{\boldsymbol{C}}_e'\right)^{-1}\overleftrightarrow{\boldsymbol{C}}(\boldsymbol{S}_t)\right) = (\alpha - 1)\mathbf{Pr}_{ax}\left(\left(\overleftrightarrow{\boldsymbol{C}}_e'\right)^{-1}\overleftrightarrow{\boldsymbol{C}}(\boldsymbol{S})\right) \tag{B.19}$$

To simplify, we define the following operator:

$$\hat{\boldsymbol{G}}(\boldsymbol{u}) \coloneqq \left(\overleftrightarrow{\boldsymbol{C}}_e'\right)^{-1}\overleftrightarrow{\boldsymbol{C}}(\boldsymbol{u}) \tag{B.20}$$

Additionally, because $\alpha \geq 1$ (the outer surface must be at least as large as the inner surface), then $(\alpha - 1)$ is a constant $\lambda \in \mathbb{R}^+$.

$$\mathbf{Pr}_{ax}\left(\hat{\boldsymbol{G}}(\boldsymbol{S}_t)\right) = \lambda\mathbf{Pr}_{ax}\left(\hat{\boldsymbol{G}}(\boldsymbol{S})\right) \tag{B.21}$$

Therefore, $\beta_{y_1} = \beta_{y_2} = \alpha$ and there will be no change in the CPE if and only if the vector $\mathbf{Pr}_{ax}\left(\hat{\boldsymbol{G}}(\boldsymbol{S}_t)\right)$ is parallel to the vector $\mathbf{Pr}_{ax}\left(\hat{\boldsymbol{G}}(\boldsymbol{S})\right)$.

Finding When $\mathbf{Pr}_{ax}\left(\hat{\boldsymbol{G}}(\boldsymbol{S}_t)\right) \,||\, \mathbf{Pr}_{ax}\left(\hat{\boldsymbol{G}}(\boldsymbol{S})\right)$

Because the relation of $\boldsymbol{S}_t$ to $\boldsymbol{S}$ now defines whether CPE changes or not, we examine the vector $\boldsymbol{S}_t$ in more detail ($\boldsymbol{S}$ can point anywhere in the first quadrant, but $\boldsymbol{S}_t$ depends on $\boldsymbol{S}$ and therefore is the only vector capable of changing the relationship between the two, making it the relevant vector). For all tabulated moments of inertia of which we are aware, the squares of the measures of shape comprise $\boldsymbol{S}$. Therefore, an individual component of $\boldsymbol{S}_t$ is generally of the form:

$$S_{t,i} = 2S_i t + t^2 \tag{B.22}$$

and therefore, $\boldsymbol{S}_t$ can be further decomposed into several vectors.

$$\boldsymbol{S}_t = 2t\boldsymbol{S} + t^2\boldsymbol{1}_n \tag{B.23}$$

where $\boldsymbol{1}_n$ is a one vector of dimension n (an n-dimensional vector where every entry is a 1). In general, the vector $2t\boldsymbol{S}$ is just a scaled version of the original measures of shape and therefore parallel to the original vector. However, the vector $t^2\boldsymbol{1}_n$ can only point in the direction of the $\boldsymbol{1}_n$. Therefore, in general the vector $\boldsymbol{S}$ will not be parallel to the vector $\boldsymbol{S}_t$ unless $\boldsymbol{S}$ is parallel to the one vector, that is, unless all measures of shape are equal to each other.

Summary of Findings: Determining When the CPE Changes

Given the previous results, there are generally two instances under which the CPE will not change. The first situation occurs when the measures of shape are all equal to each other. In this case, $\boldsymbol{S}$ is parallel to $\boldsymbol{1}_n$ and therefore also parallel to $\boldsymbol{S}_t$. Because $\hat{\boldsymbol{G}}$ is a linear operator, and therefore also affine, lines that are parallel before the transformation will remain parallel after the transformation, which guarantees that $\hat{\boldsymbol{G}}(\boldsymbol{S}_t)$ is parallel to $\hat{\boldsymbol{G}}(\boldsymbol{S})$. Because the entire vector is parallel, any projection of the vectors will also be parallel, therefore satisfying equation B.18 and showing that the CPE will not change. This will be true for all values of t and therefore if these conditions are met, then both values of the CPE will always remain constant. For most shapes, this will correspond to something that appears spherical. For example, if all measures of shape are equal for a rectangular prism, then it is a cube and appears spherical to CPE. For a cylinder, however, this is not true. A cylinder will have equal moments of inertia about all axes and appear spherical when the measures of shape are unequal. Nevertheless, it is still true that if all of the measures of shape are equivalent, then there will be no change in the CPE.

The second situation concerns the case where the entire vector is not parallel, but the projections onto either the ab or ac planes are parallel. This situation is difficult to determine mathematically because it requires knowledge of the specific transformations performed by the moments of inertia equation (rotation, scale, shear, etc), which changes depending on the specific shape. However, this situation is intuitive and easy to identify for a given shape. In these cases, at most one of the two values of CPE remains constant and this lack of change occurs due to symmetry. For example, the cross-section of a cylinder across the length is a circle, giving it radial symmetry about the length. Therefore, the ellipsoid modeling a cylinder must have at least two equal semiaxes to also achieve the same radial symmetry. If $r \ll L$, then the corresponding ellipsoid will have $a > b = c$, making it a prolate ellipsoid and both e_{ab} and e_{ac} will change. In other words, the vectors are parallel only along the projection onto the plane bc, which we have previously noted is not of interest here. However, if $r > L$ then the cylinder is actually a disk and the corresponding ellipsoid is oblate, having $a = b > c$. In that case, the vectors are parallel along the projection onto the plane ab, it is an oblate ellipsoid and e_{ab} will remain constant at $e_{ab} = 0$ while e_{ac} changes. Note that in both cases, the projections of the vectors could easily be identified as parallel along a given plane by figuring out which two apparent semiaxes had to be equal to give the shape the proper symmetry to match the original shape. We cannot cover every possible shape in this way, but since these situations can be readily identified, we simply note the possibility and leave it as an exercise for the reader to identify specific instances of this behavior.

B.8 How CPE Changes with the Addition of a Constant

In this section, we demonstrate that when the CPE changes, it must always decrease. We start by noting that the general science of rotating objects[8] constrains the behavior of the moments of inertia equations such that if the measures of shape are more similar to each other, then the moments of inertia must also become more similar to each other. We then demonstrate that the addition of a constant to the measures of shape always guarantees that they become more similar, therefore ensuring that the apparent semiaxes also become more similar to each other and the CPE falls towards zero.

If the Measures of Shape are Similar, the Moments of Inertia will also be Similar

It is relatively straightforward to show and intuitive to understand that if the measures of shape for a particular shape become more similar to each other, then the moments of inertia for a shape will become more similar to each other as well. Con-

---

[8] One would assume that there is some mathematical property of the moments of inertia equation which would guarantee this behavior, but I have not been able to find it. It is an affine transformation, but from what I was able to find, this is not a strong enough condition to guarantee that more similar moments of inertia are created by more similar measures of shape. It would have to be true that it is an affine transformation and only limited to certain types of affine transformations, such as perhaps a rotation, but it is not clear how one could prove that every possible equation compututing the moments of inertia constitutes a pure rotation affine transformation. Therefore, I can only reliably cite the intuitive scientific notion if a shape appears more spherical, it will rotate more like a sphere.

sider a rod with a large aspect ratio. In this case, the moment of inertia associated with spinning around the long axis of the rod is much smaller than the other two moments of inertia. However, if we shorten its length, then the two large moments of inertia will drop until, as we continue to shorten the length, they are eventually equal to smaller moment of inertia. The converse is also true. To obtain more equal moments of inertia, the measures of shape must become more equal. Therefore, if we take an arbitrary shape and make the measures of shape more similar to each other, then we are making the moments of inertia more similar to each other. Then by the transitive property, we are also making the apparent semiaxes more equal to each other. CPE essentially measures how similar these apparent semiaxes are to each other. If the apparent semiaxes become more equal to each other, the CPE must fall.

Although it is generally easy to show scientifically that as the measures of shape become more similar, the moments of inertia also become more similar, we are unsure which specific mathematical property of the moments of inertia equation (equation B.1) gives rise to this behavior. It is particularly difficult to specify a mathematical reason because the moments of inertia are not limited to a single function but to many different functions. As noted in section B.7, the moments of inertia for different shapes comprise many different types of transformations and are generally functions mapping from many different dimensions into three dimensions. Therefore, it is not even clear if these equations all belong to the same class or set, mathematically speaking. To the best of our understanding, this behavior arises from a combination of being a linear transformation, the requirement that both the measures of shape and the moments of inertia be measurable, that the zero vector is fixed, and that the transformation is injective. This severely limits the number of transformations that are possible. For example, most rotations and reflections would result in some portion of the codomain[9] containing negative values, which are not measurable and therefore not possible. A translation is not linear and does not fix the zero vector, so translation is also forbidden. Similarly, although linear projections are allowed, not all projections are linear. This leaves only certain rotations, reflections, or projections, as well as scaling, and shear transformations or some combination of those possibilities. Of those possibilities, only shear is not angle preserving, but even in this case, the sign of a change in angle is preserved. Therefore, while angles may not generally be preserved under the transformation to the moments of inertia, a monotonic change in the angles in the measures of shape vector space will still produce a monotonic change in the angles in the moments of inertia vector space and the sign of the change will be preserved. This is sufficient to support the scientific intuition about the moments of inertia.

Developing a Metric for Measures of Shape Similarity

The moments of inertia will become more similar if the measures of shape become more similar, which in turn means that the apparent semiaxes will become more similar. Therefore, we need to prove that adding a constant, t, makes the measures of shape more similar to each other. We start by noting that computing the moments of inertia is a linear transformation that maps an n-dimensional vector onto a three-dimensional vector (see equations B.1 and B.9). We can examine how close the measures of shapes are to each other by comparing the vector, $\boldsymbol{S}'$ with a vector whose elements are all equal. The simplest (non-trivial) vector whose elements are all equal is the one-vector, $\mathbf{1}_n$. So we examine the angle between $\boldsymbol{S}'$ and $\mathbf{1}_n$, shown graphically in Figure B.3. If all measures of shape are exactly equal, then the $\boldsymbol{S}$ is a multiple of $\mathbf{1}_n$ and the angle between them is zero ($\boldsymbol{S}||\boldsymbol{S}'||\mathbf{1}_n$).

---

[9] Roughly similar to the range of a function, the codomain is the set of all outputs a function may have, such that the range is a subset of the codomain

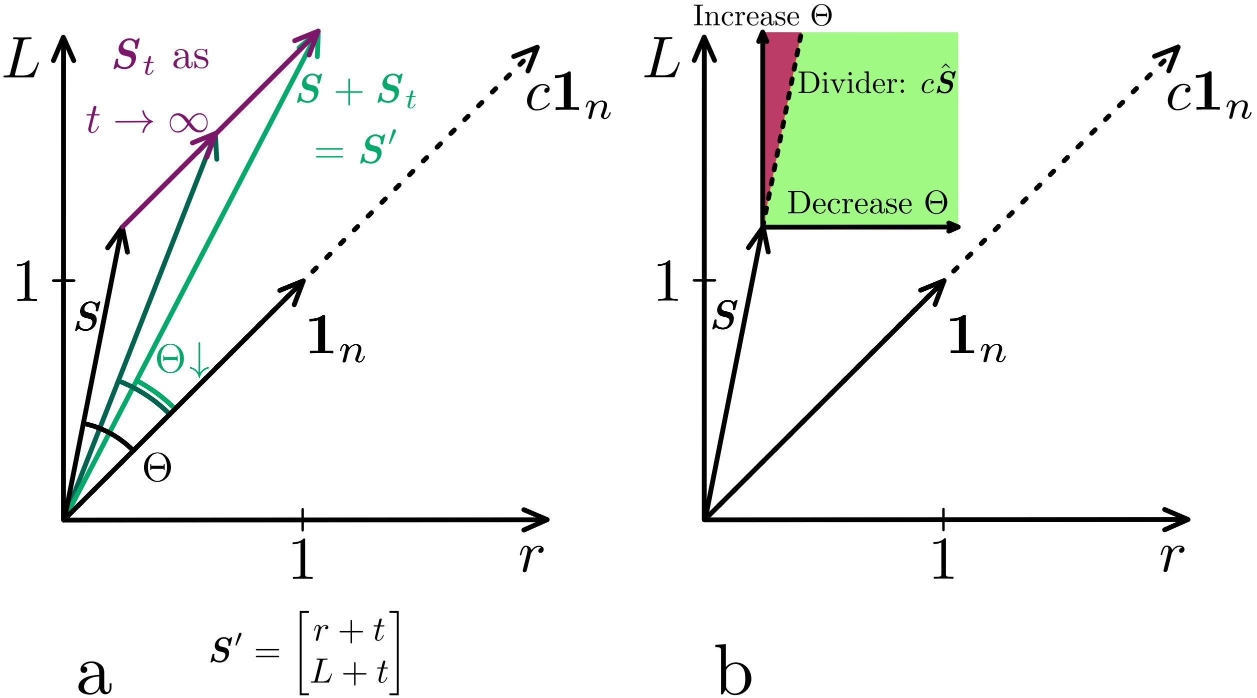

Figure B.3: A visualization of the vectors and angles arising from the addition of a constant thickness to the measures of shape. Here we show a cylinder as a representative shape with two measures of shape. a) Measures of shape for the outer surface, $\boldsymbol{S}'$ (green), are represented as a vector addition of the inner surface, $\boldsymbol{S}$ (black), and the vector resulting from adding t, $\boldsymbol{S}_t$ (purple). Here we examine the simpler, if uncommon, case where the outer surface can be obtained as shown in the equation below the vectors. As t increases, Θ is seen to decrease. b) The shaded region shows the directions where possible vectors for $\boldsymbol{S}_t$ may point, which follows from all measures of shape being measurable. If $\boldsymbol{S}_t$ is in the green-shaded region, then Θ will decrease. If $\boldsymbol{S}_t$ is in the maroon-shaded region, then Θ will increase. The dividing line is in the direction of $\boldsymbol{S}$ and will change as $\boldsymbol{S}$ changes. In both plots, c represents some scalar value.

The vector $\mathbf{1}_n$ lies at an angle of $\frac{\pi}{4}$ radians with respect to all axes. Additionally, as a real measure, all components of $\boldsymbol{S}'$ must be positive and the vector must be in the first quadrant (octant, etc), and therefore the angle between $\boldsymbol{S}'$ and $\mathbf{1}_n$ is constrained to be between 0 and $\frac{\pi}{4}$ radians.This construction is shown graphically in Figure B.3. The angle between the $\mathbf{1}_n$ and the measures of shape can be computed using equation B.24.

$$\Theta = \cos^{-1}\left(\frac{\sum_{i=1}^{n}(S_i + t)^2}{\sqrt{n\sum_{i=1}^{n}(S_i + t)^4}}\right) \tag{B.24}$$

Because Θ represents the angle between the measures of shape and a vector where all elements are equal to each other, the smaller Θ is, the more similar the measures of shape are to each other. It then also follows that if Θ decreases, the measures of shape become more similar to each other and the CPE will decrease. A shape that appears spherical ($e_{ab} = e_{ac} = 0$) has all measures of shape exactly equal to each other, so that $\boldsymbol{S}||\mathbf{1}_n$ and $\Theta = 0$. Note that equation B.24 assumes that the moments of inertia are computed from the squares of the measures of shape, see for example equation B.6 and B.7, because this is by far the most common situation encountered. Equation B.24 is obtained simply by substituting $\boldsymbol{S}'$ and $\mathbf{1}_n$ into the well-known formula for the angle between two vectors and simplifying so it can be recomputed for an arbitrary moments of inertia equation if needed.

Examining the Limits

When t is small, Θ assumes the value given for the original vector, $\boldsymbol{S}$. As t grows to infinity, we take the limit.

$$\lim_{t\to\infty}\Theta = \cos^{-1}\left(\frac{n(\infty)^2}{\sqrt{n^2(\infty)^4}}\right) = \cos^{-1}(1) = 0 \tag{B.25}$$

So equation B.25 must go to zero in the limit, as we have already shown much more simply with the Minkowski sums.

On the Monotonicity of the Change

In addition to the direction of the change in CPE, we also need to show that the CPE always moves in this direction (toward zero). We start with the simpler case where $\boldsymbol{S}'$ is of the form $S_i + t$, as depicted in Figure B.3a. Here, it is straightforward to note that from the vector $\boldsymbol{S}$, we have added a vector, $t\mathbf{1}_n$ and moved at an angle of $\frac{\pi}{4}$ radians with respect to each axes. As t continues to grow, the direction of this additional vector never changes and is always parallel to the line passing through the origin and in the direction of $\mathbf{1}_n$. Therefore, the angle between these two vectors can only ever decrease.

A more relevant case is where $\boldsymbol{S}'$ takes the form $S_i^2 + 2S_it + t^2$, as is the case for most tabulated shapes. As the sum of three terms, we can represent $\boldsymbol{S}'$ as the sum of three vectors, such that $\boldsymbol{S}' = \boldsymbol{S} + 2t\boldsymbol{S} + t^2\mathbf{1}_n$. We can now see that the situation is only slightly more complicated than in the case depicted in Figure B.3a. Like in the simpler case shown in Figure B.3a, we take the inner surfaces measures of shape, $\boldsymbol{S}$, and add vector parallel to the one vector, $t^2\mathbf{1}_n$, although this time it is proportional to t^2 instead of t and therefore receives significantly more weight. The chief difference is that we now have an additional vector being added, $2t\boldsymbol{S}$. The value of t is a scalar so this vector is simply a scaled vector, parallel to $\boldsymbol{S}$. There are no components that would move the vector into the orange region depicted in Figure B.3b and increase the angle, Θ. There are only the original vector, a scaled copy of the original vector, and a vector parallel to the one vector. Therefore, while the speed at which Θ will change is greatly affected, the result in still the same as in the simpler case and Θ must always decrease.

In the most general case where $\boldsymbol{S}'$ is of any unknown form, the same general reasoning applies. Both $\boldsymbol{S}$ and t must always be positive because they are real, measurable quantities. Therefore, there is no operation that can lead to any function for $\boldsymbol{S}'$ that is not monotonically increasing. In turn, the vector must always grow generally in the direction of $\mathbf{1}_n$, the angle between $\boldsymbol{S}'$ and $\mathbf{1}_n$ must always decrease, and the CPE must always drop.

B.9 Consideration for the Measures of Shape

To this point, we have developed this work entirely based on the properties of the functions involving the measures of shape without application to the real world cases this work aims to model. Although we developed this work based on the idea of a core/shell construct with a shell of constant thickness, in some cases, the model does not guarantee a constant thickness between the core and the shell. For instance, consider a cylinder. If we center the two surfaces so that they share the same center of mass, one finds that the "shell" on the circular faces of the cylinder is closer to the original shape than around the circumference of the cylinder, because the constant addition, t, is added to both the radius and the length. Adding t to the length adds $\frac{1}{2}t$ to either side. However, adding t to the radius, adds t on either side of the core's diameter. This is because length is what we may term a "spanning" measure of shape while the radius is not, where we define a spanning measure of shape to be one that measures from edge to edge. The radius, on the other hand, measures from the center to the edge and is therefore not spanning.

To create a shell of constant thickness, all of the measures of shape must either be spanning or not. If all of the measures of shape are spanning, then the shell has a thickness of $\frac{1}{2}t$, but one can simply adjust the value of t to compute the change that reflects the real thickness. If all of the measures of shape are not spanning, then the shell has a thickness of t directly and there is no issue. The shell thickness is only non-uniform if some are spanning and others are not.

Appendix C

Full Data Sets

C.1 CPE Raw Distributions

In this section, we provide the raw CPE population distributions like that exemplified in Figure 4.2a, but for all surfaces and all simulations.

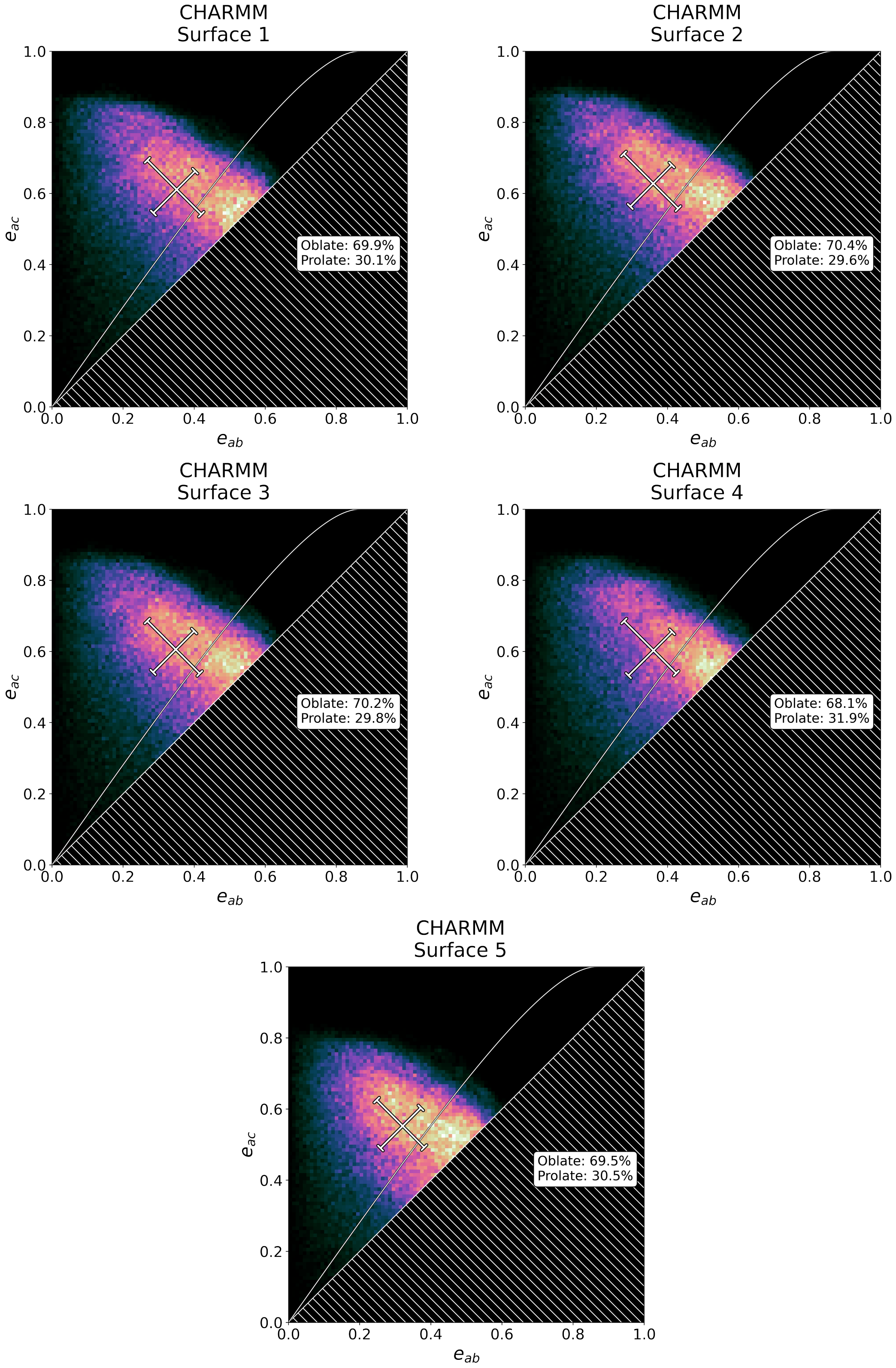

Figure C.1: CPE distributions for the CHARMM simulations, surfaces as labelled.

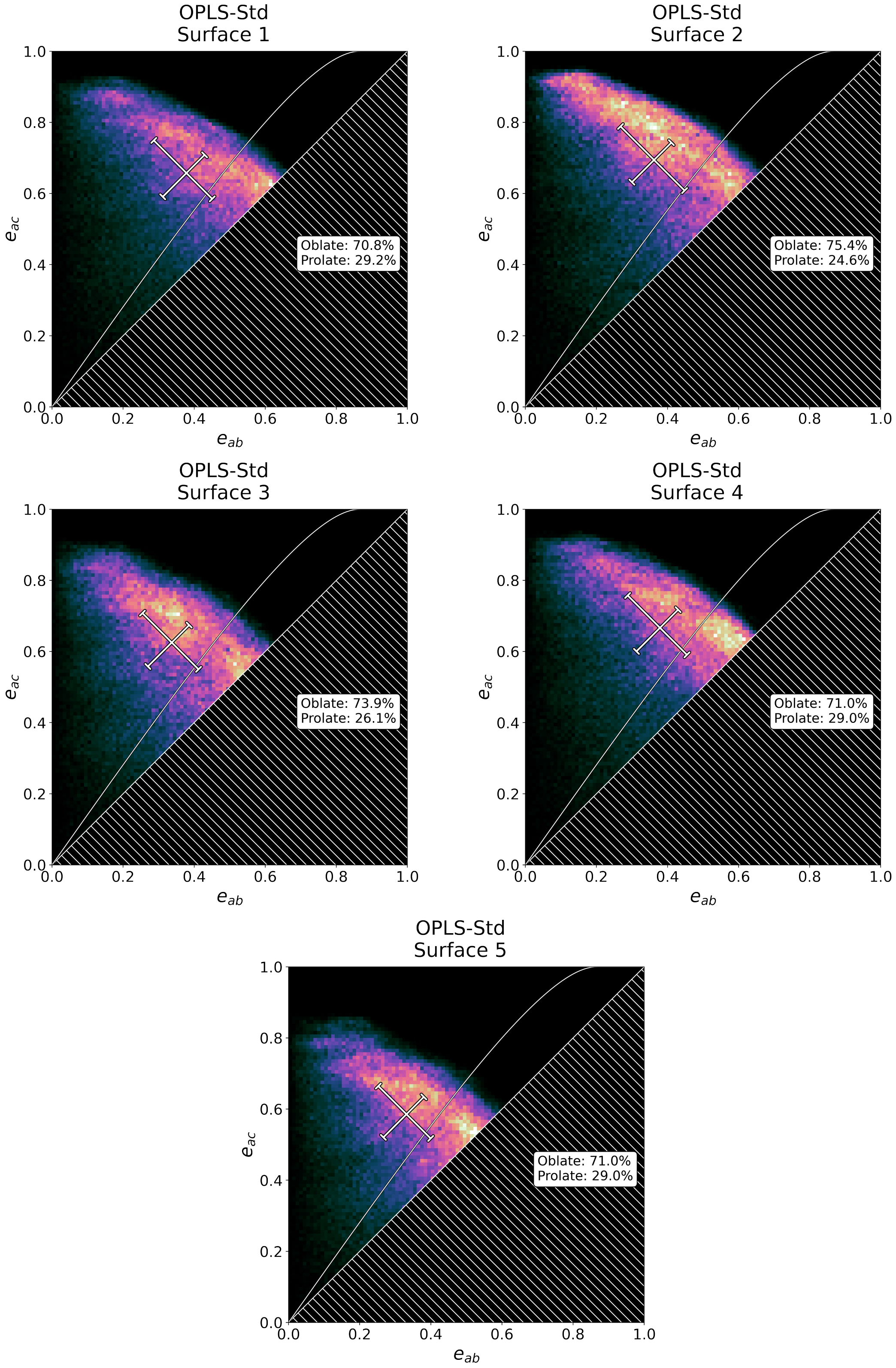

Figure C.2: CPE distributions for the OPLS-Std simulations, surfaces as labelled.

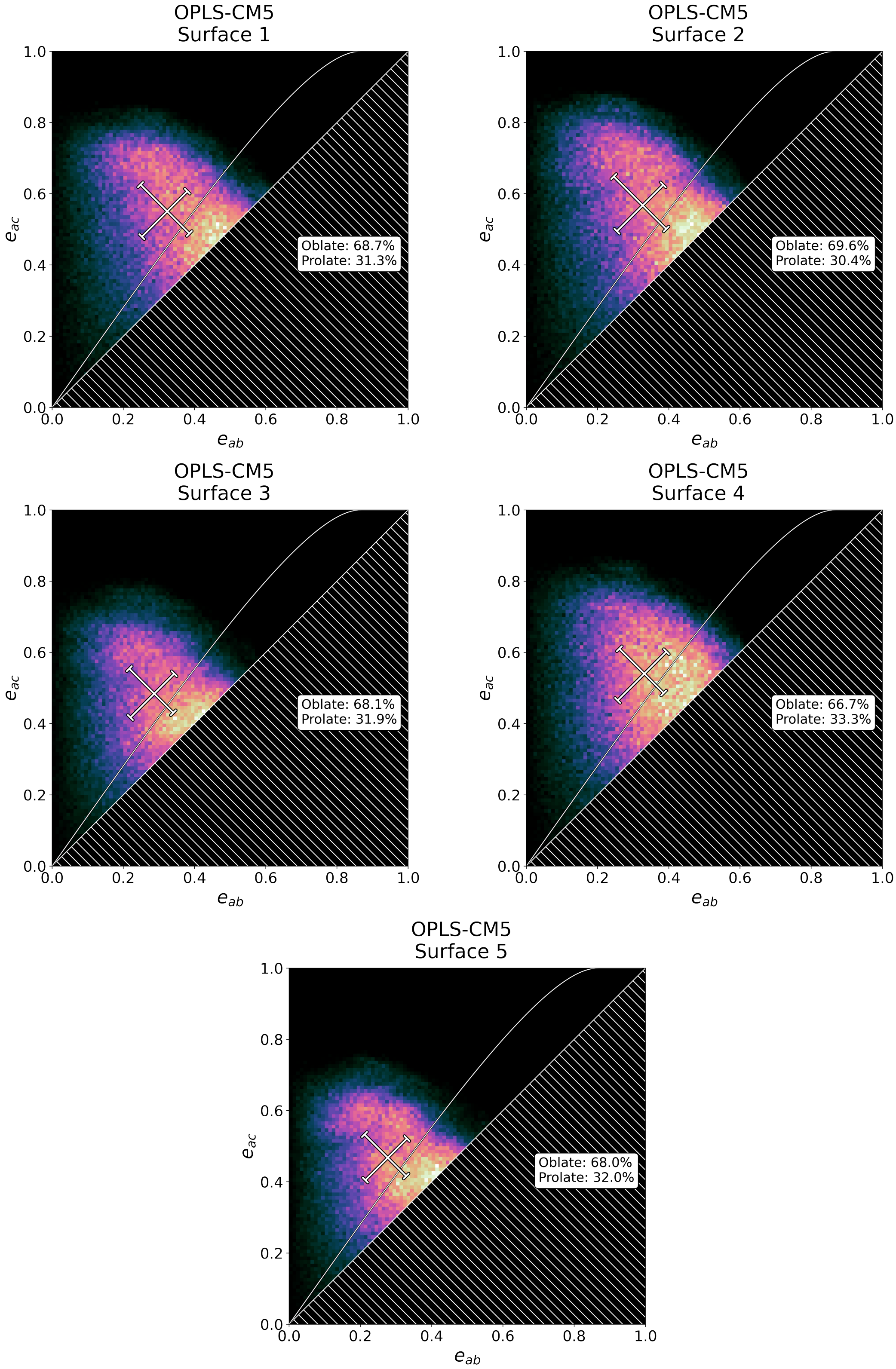

Figure C.3: CPE distributions for the OPLS-CM5 simulations, surfaces as labelled.

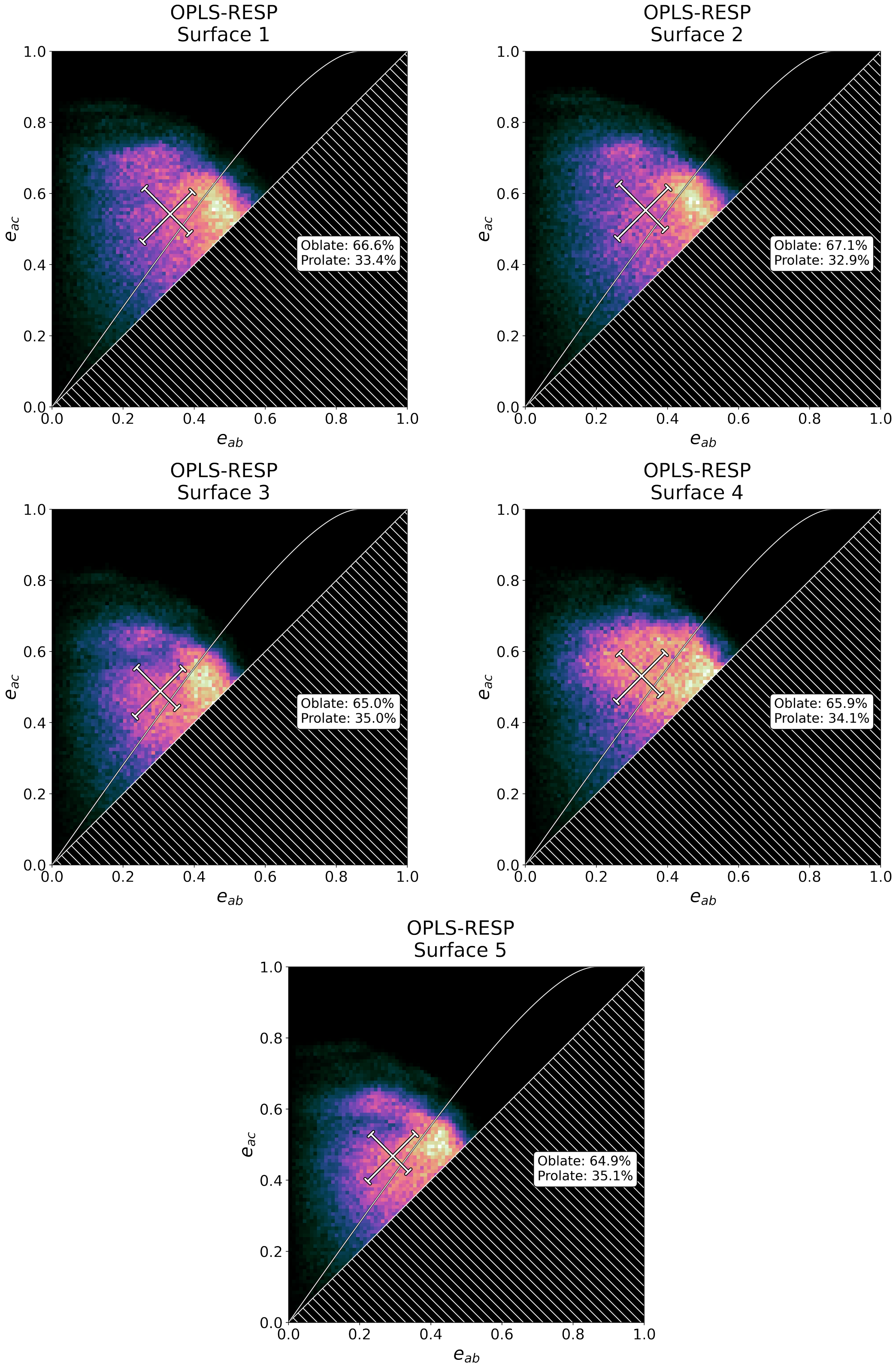

Figure C.4: CPE distributions for the OPLS-RESP simulations, surfaces as labelled.

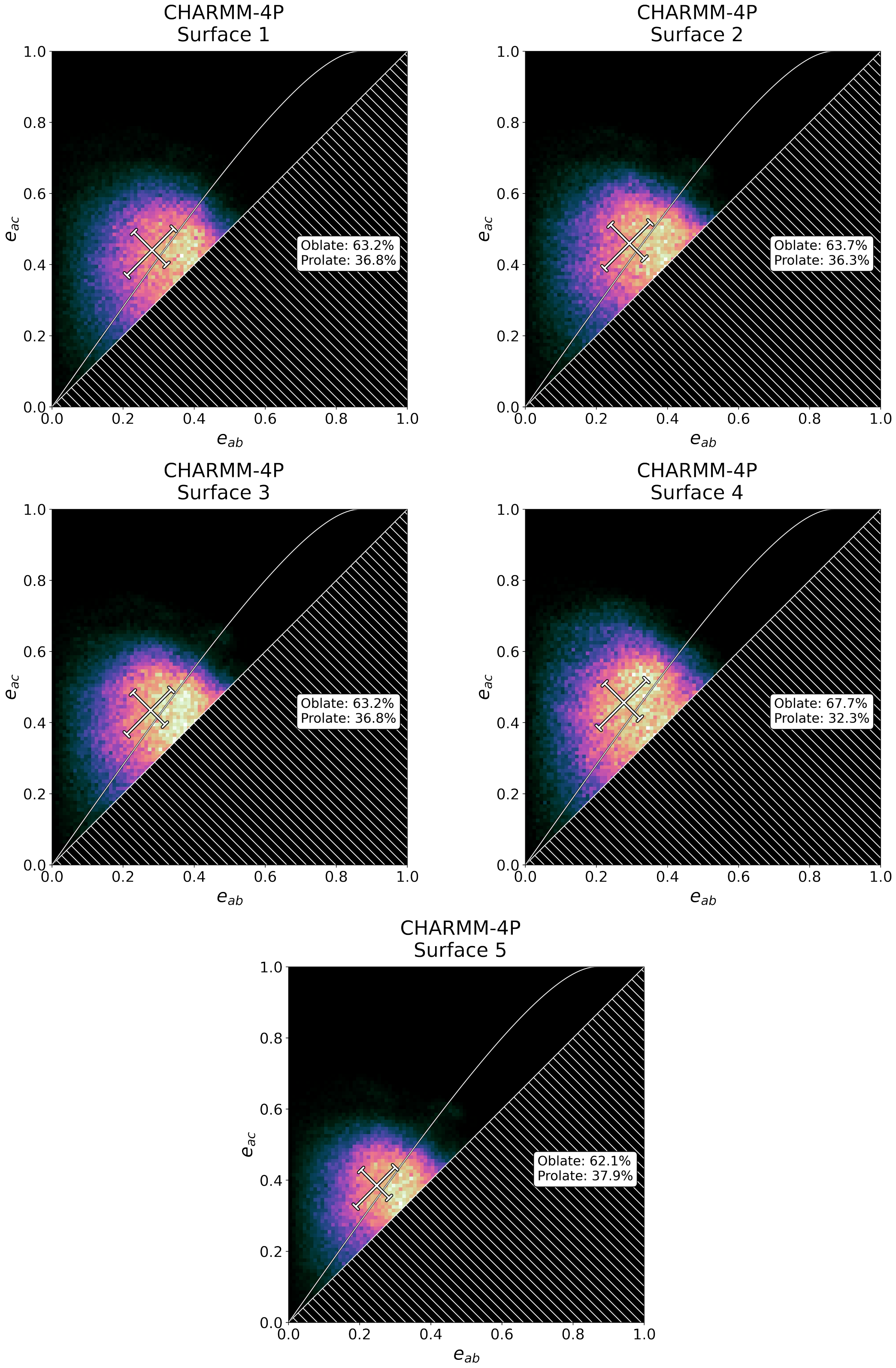

Figure C.5: CPE distributions for the CHARMM-4P simulations, surfaces as labelled.

C.2 Convexity Time Series

This section provides the time series of convexity for each simulation.

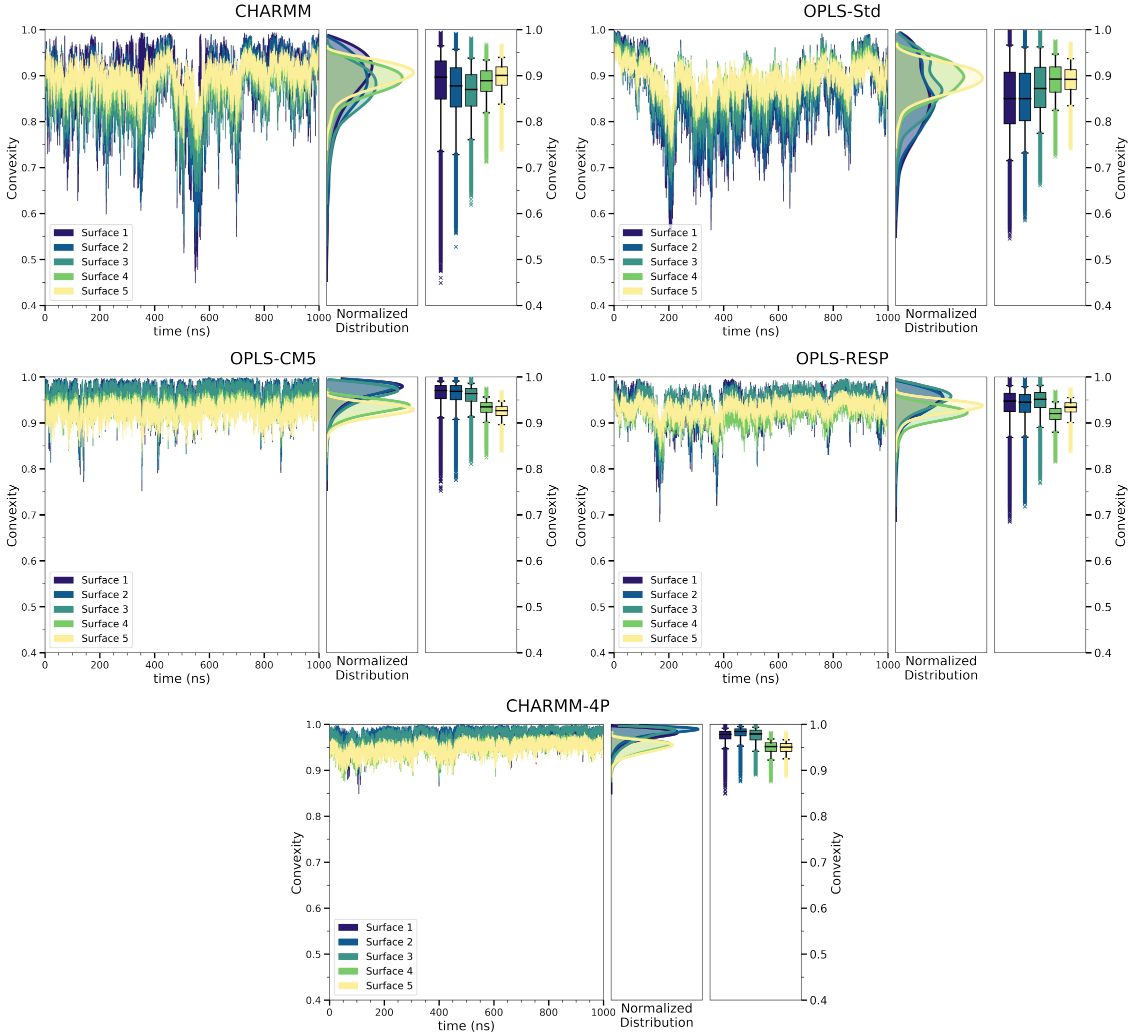

Figure C.6: Raw convexity time series and the associated population distributions for all simulations, as labelled.

C.3 Shape Autocorrelations and Residuals

Figure C.7 shows the raw autocorrelations of CPE, the fits and their residuals for all simulations and all surfaces. Figure C.8 provides the same information for the convexity of each simulation and surface.

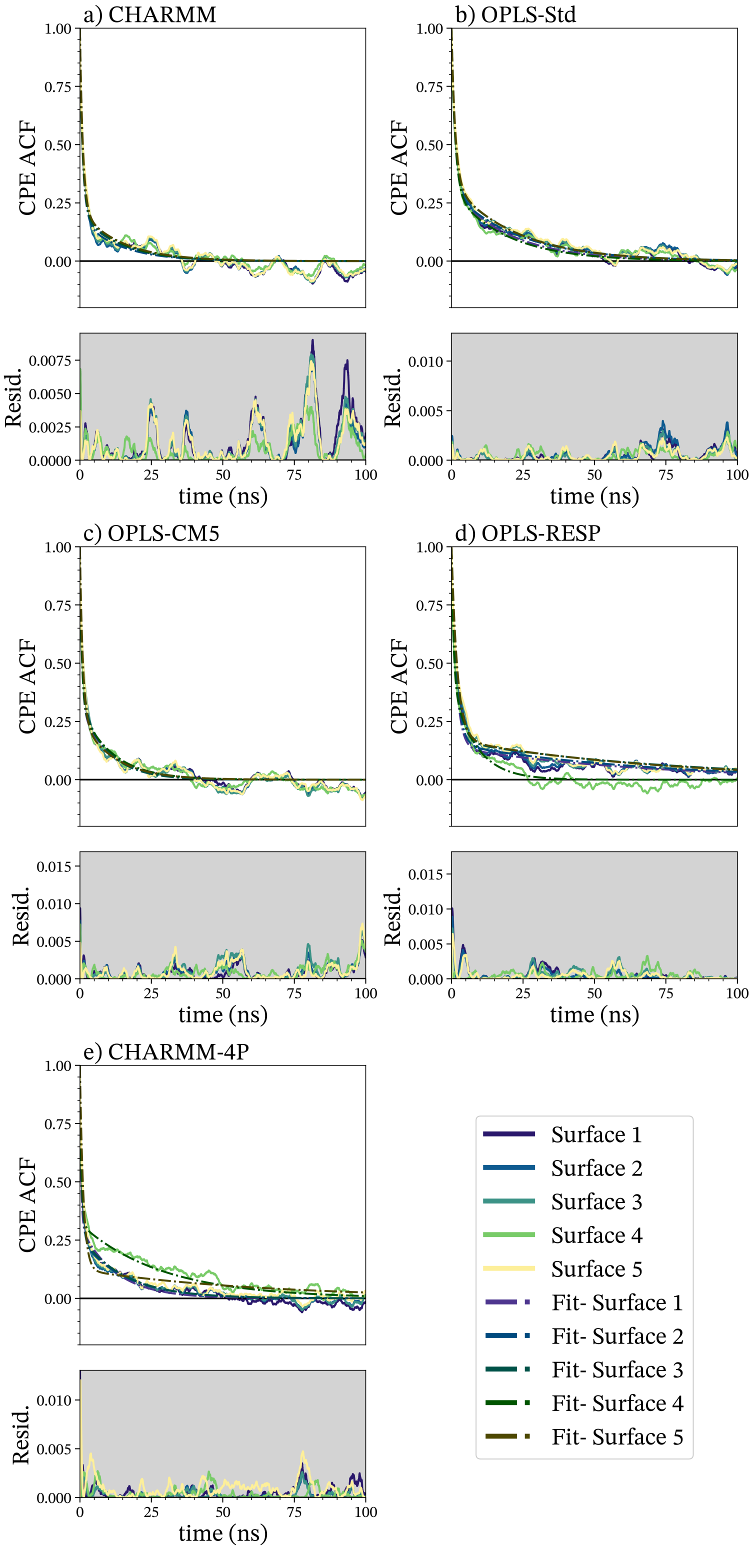

Figure C.7: a-e) Vector autocorrelations of CPE for each surface as well as the associated fits for each surface. Below the autocorrelations, in a gray plot, is the residuals for each fit.

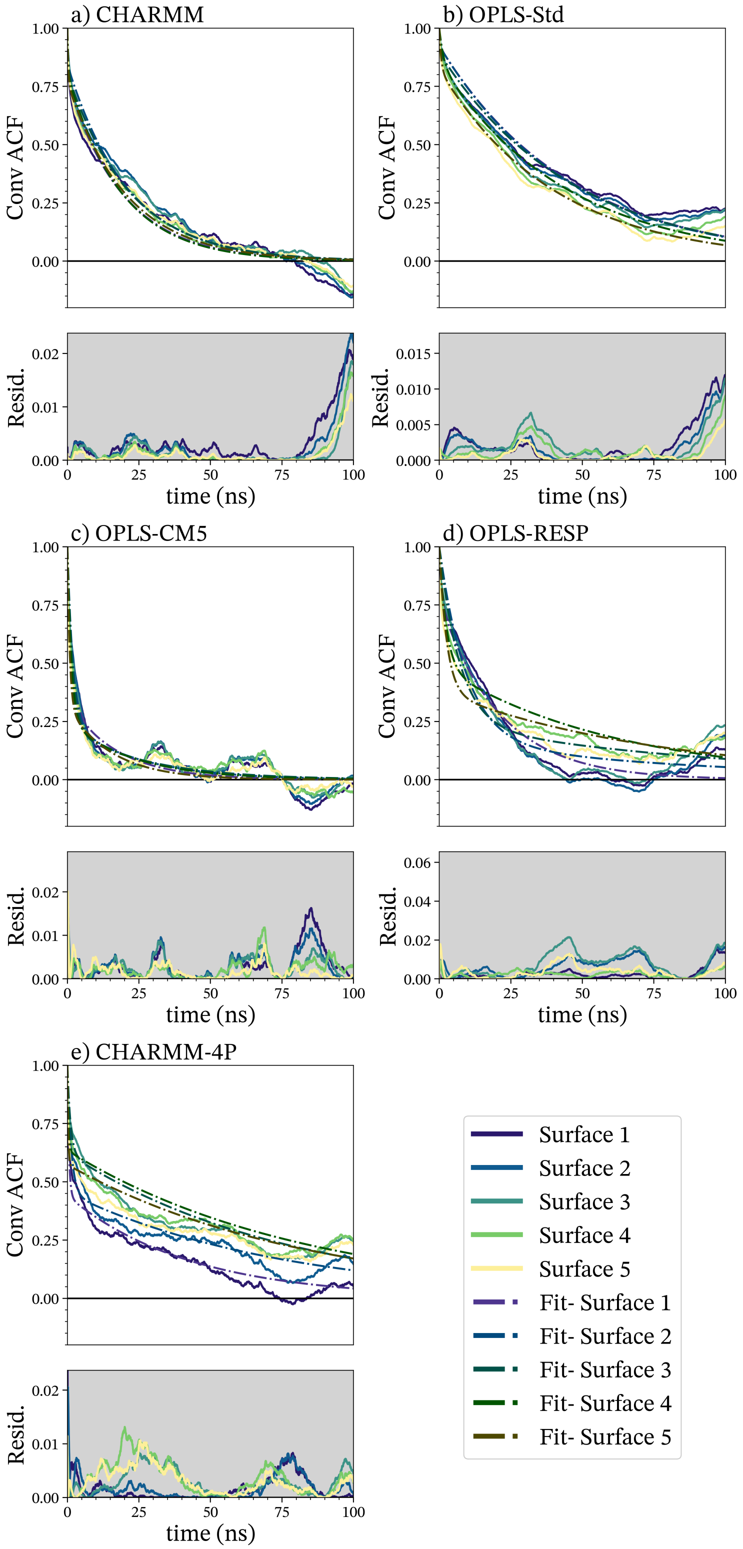

Figure C.8: a-e) Scalar autocorrelations of convexity for each surface as well as the associated fits for each surface. Below the autocorrelations, in a gray plot, is the residuals for each fit.

Appendix D

OPLS Force Field Parameters for AOT

The information in this chapter has been published in Ref. 3.

We continue the naming scheme OPLS uses for the other atom types to accomodate the new atoms needed to model AOT. At the time we made the files, these were 972, 973, and 974, with the appropriate "opls_" prefix, to represent the sulfonate sulfur, sulfonate oxygen, and the carbon bonded to the sulfonate, respectively. These can be given new names or updated to match the modern version of OPLS atom types as needed.

All atomic parameters are listed in the order that matches the structure files used here. We provide Figure D.1 to help match atom indices to their respective positions in the molecule. Each atom has been given a unique, if unimaginative, name as another means of identification. This unique name is consistent between the tables provided here as well as the attached structure and topology files.

D.1 Atoms and Partial Charges

The relevant quantities for the new atom types needed for this force field are provided in Table D.1. The full list of atoms, their OPLS atom type, and their partial charges in each charge scheme used in this work are provided in Table D.2.

		Lennard-Jones		
Atom Type	**Mass (amu)**	**σ (nm)**	**ϵ (kJ/mol)**	**Description**
opls_972	32.06600	0.319500	0.891192	Sulfonate S[74]
opls_973	15.99940	0.283500	0.711280	Sulfonate O[74]
opls_974	12.01100	0.351500	0.418400	C bonded to sulfonate S[74]

Table D.1: Definition of new atom type needed for modelling the sulfonate moiety

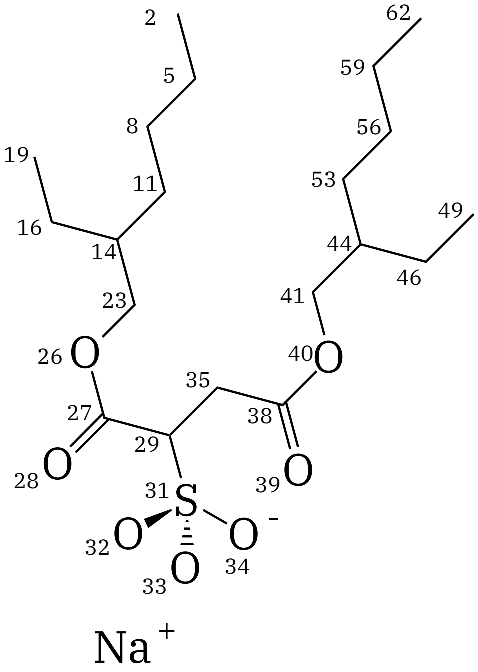

Figure D.1: The index of each atom used in the attached GROMACS files and associated tables. Only non-hydrogen atoms are numbered.

Table D.2: Atoms and Charges for OPLS Simulations

Index	Atom Type	Element	Std. Charge	CM5 Charge	RESP Charge
1	opls_140	H	0.06	0.072009	0.06529
2	opls_135	C	-0.18	-0.228523	-0.29695
3	opls_140	H	0.06	0.077337	0.06529
4	opls_140	H	0.06	0.075116	0.06529
5	opls_136	C	-0.13	-0.150505	0.143399
6	opls_140	H	0.06	0.070717	-0.023409
7	opls_140	H	0.06	0.072749	-0.023409
8	opls_136	C	-0.13	-0.149309	0.12076
9	opls_140	H	0.06	0.081329	-0.003799
10	opls_140	H	0.06	0.077438	-0.003799
11	opls_136	C	-0.13	-0.148861	-0.377429
12	opls_140	H	0.06	0.074194	0.066458

Index	Atom Type	Element	Std. Charge	CM5 Charge	RESP Charge
13	opls_140	H	0.06	0.072561	0.066458
14	opls_137	C	-0.06	-0.072621	0.069642
15	opls_140	H	0.06	0.087719	0.059228
16	opls_136	C	-0.12	-0.149474	0.17021
17	opls_140	H	0.06	0.086821	-0.027571
18	opls_140	H	0.06	0.071552	-0.027571
19	opls_135	C	-0.18	-0.229896	-0.187929
20	opls_140	H	0.06	0.07436	0.035986
21	opls_140	H	0.06	0.068267	0.035986
22	opls_140	H	0.06	0.077447	0.035986
23	opls_490	C	0.19	-0.040155	0.212639
24	opls_469	H	0.03	0.091389	0.028405
25	opls_469	H	0.03	0.099265	0.028405
26	opls_467	O	-0.33	-0.195868	-0.572906
27	opls_465	C	0.51	0.272589	0.974705
28	opls_466	O	-0.43	-0.341793	-0.621886
29	opls_974	C	-0.14	-0.079603	-0.368574
30	opls_140	H	0.06	0.099343	0.172709
31	opls_972	S	1.18	0.524515	1.094344
32	opls_973	O	-0.68	-0.465743	-0.641226
33	opls_973	O	-0.68	-0.461706	-0.622994
34	opls_973	O	-0.68	-0.465263	-0.633793
35	opls_136	C	-0.12	-0.146164	-0.52881
36	opls_140	H	0.06	0.104383	0.187399
37	opls_140	H	0.06	0.102122	0.187399
38	opls_465	C	0.51	0.277638	0.980161
39	opls_466	O	-0.43	-0.340796	-0.638557

Index	Atom Type	Element	Std. Charge	CM5 Charge	RESP Charge
40	opls_467	O	-0.33	-0.201716	-0.559863
41	opls_490	C	0.19	-0.040825	0.273523
42	opls_469	H	0.03	0.092829	0.006374
43	opls_469	H	0.03	0.095863	0.006374
44	opls_137	C	-0.06	-0.072926	0.177328
45	opls_140	H	0.06	0.083663	0.004636
46	opls_136	C	-0.12	-0.149764	-0.099375
47	opls_140	H	0.06	0.07219	0.030451
48	opls_140	H	0.06	0.074126	0.030451
49	opls_135	C	-0.18	-0.231122	-0.098519
50	opls_140	H	0.06	0.073379	0.031337
51	opls_140	H	0.06	0.081576	0.031337
52	opls_140	H	0.06	0.075563	0.031337
53	opls_136	C	-0.13	-0.146844	-0.310106
54	opls_140	H	0.06	0.074756	0.044019
55	opls_140	H	0.06	0.078509	0.044019
56	opls_136	C	-0.13	-0.149895	0.131821
57	opls_140	H	0.06	0.075656	-0.026103
58	opls_140	H	0.06	0.074947	-0.026103
59	opls_136	C	-0.13	-0.149474	0.163624
60	opls_140	H	0.06	0.074003	-0.024635
61	opls_140	H	0.06	0.07499	-0.024635
62	opls_135	C	-0.18	-0.228387	-0.290599
63	opls_140	H	0.06	0.074491	0.06259
64	opls_140	H	0.06	0.075146	0.06259
65	opls_140	H	0.06	0.074686	0.06259
66	opls_407	Na	1	1	1

D.2 Intramolecular Parameters

Table D.4 provides all of the bonded interactions. All listed interactions are a harmonic strertching potential of the form given in Equation D.1.

$$V_b(r_{ij}) = \frac{1}{2}k_b(r_{ij} - b_0)^2 \tag{D.1}$$

V_b is the potential energy, r_{ij} denotes the distance between atoms i and j, k_b is the harmonic spring constant, and b_0 is the equilibrium distance between atoms i and j.

Table D.4: Definition of bond stretching parameters

Atom 1	**Atom 2**	b_0 **(nm)**	k_b **(kJ/mol nm^2)**	**Comments**
opls_974	opls_140	0.109	284512	OPLS' (HC-C)
opls_972	opls_973	0.1455	533100	Ref. 73
opls_974	opls_972	0.1792	197000	Ref. 73
opls_974	opls_136	0.1529	224262.4	OPLS' (CT-CT)
opls_465	opls_974	0.1522	265265.6	OPLS' (C_2-CT)

Table D.5 provides all of the angle bending interactions. All listed interactions use a harmonic angle potential of the form given in Equation D.2.

$$V_a(\theta_{ijk}) = \frac{1}{2}k_a(\theta_{ijk} - \theta_0)^2 \tag{D.2}$$

Like for the harmonic bond potentials, V_a represents the potential energy, θ_{ijk} represents the angle between atoms i, j, and k, k_a is the harmonic spring constant for the angle, and θ_0 is the equilibrium angle between atoms i, j, and k. Be careful of the units because we provide the GROMACS default units here. The equilibrium angle, θ_0 is provided in degrees while the harmonic spring constant is given in kJ mol^{-1} rad^{-2}, using radians for the angle here.

Table D.5: Definition of angle bending parameters

Atom 1	**Atom 2**	**Atom 3**	θ_0 **(deg)**	k_a **(kJ/mol nm^2)**	**Comments**
opls_973	opls_972	opls_973	114	969	Ref. 73
opls_140	opls_974	opls_972	107.3	390.3	Ref. 73
opls_140	opls_974	opls_136	110.7	313.8	OPLS' (CT-CT-HC)
opls_974	opls_972	opls_973	104.5	870	Ref. 73
opls_972	opls_974	opls_136	113.3	583	Ref. 73
opls_467	opls_465	opls_974	111.4	677.808	OPLS' (OS-C_2-CT)
opls_466	opls_465	opls_974	120.4	669.44	OPLS' (CT-C_2-O_2)
opls_465	opls_974	opls_140	115	292.88	OPLS' (CT-C_2-HC)
opls_465	opls_974	opls_972	113.3	583	Ref. 73
opls_465	opls_974	opls_136	111.1	527.184	OPLS' (C_2-CT-CT)

Table D.6 provides all of the proper dihedral interactions. There is a mix of both Ryckaert-Bellemans (RB) dihedrals or as a truncated Fourier expansion (F). The Ryckaert-Bellemans dihedrals are defined by the function given in equation D.3.

$$V_{rb}(\phi_{ijkl}) = \sum_{n=0}^{5} C_n(\cos(\psi))^n \qquad ,\psi = \phi - 180° \tag{D.3}$$

The Fourier series is taken out to four terms and the dihedrals are computed using equation D.4.

$$V_F(\phi_{ijkl}) = \frac{1}{2}\left[F_1(1+\cos(\phi)) + F_2(1-\cos(2\phi)) + F_3(1+\cos(3\phi)) + F_4(1-\cos(4\phi))\right] \tag{D.4}$$

The two methods can be related via the double angle identity and associated multi-angle formulae to yield the relations given in equations D.5-D.10.

$$C_0 = F_2 + \frac{1}{2}(F_1 + F_3) \tag{D.5}$$

$$C_1 = \frac{1}{2}(-F_1 + 3F_3) \tag{D.6}$$

$$C_2 = -F_2 + 4F_4 \tag{D.7}$$

$$C_3 = -2F_3 \tag{D.8}$$

$$C_4 = -4F_4 \tag{D.9}$$

$$C_5 = 0 \tag{D.10}$$

Because both functions are interconvertible and the parameters take the same units, Table D.6 lists the parameters equally. The dihedrals we borrow from the standard OPLS parameters all had values of zero for C_4 and C_5 so we have omitted these columns.

Table D.6: Definition of proper dihedral parameters

					Parameters (kj mol^{-1})				
Atom 1 prefix: ”opls_”	**Atom 2** prefix: ”opls_”	**Atom 3** prefix: ”opls_”	**Atom 4** prefix: ”opls_”	**Func. Type**	C_0	C_1	C_2	C_3	**Comments**
140	974	972	973	F	0	0	1.625	0	Ref. 73
140	974	136	140	RB	0.6276	1.8828	0	-2.5104	OPLS (HC-CT-CT-HC)
136	974	972	973	F	0	0	1.3938	0	Ref. 73
972	974	136	140	F	0	0	1.3797	0	Ref. 73
490	467	465	974	RB	2.87441	0.58158	2.092	-5.54799	OPLS (CT-CT-CT-OS)
467	465	974	140	RB	0.97905	2.93716	0	-3.91622	OPLS (HC-CT-CT-OS)
467	465	974	972	F	-16.1	-2.0046	0.7674	0	Ref. 73
467	465	974	136	RB	-1.15688	-3.47063	0	4.6275	OPLS (CT-CT-C_2-OS)
466	465	974	140	RB	0	0	0	0	OPLS (HC-CT-C_2-O_2)
466	465	974	136	RB	3.10662	-3.77606	-5.13795	5.80739	OPLS (CT-CT-C_2-O_2)
465	974	972	973	F	0	0	1.3938	0	Ref. 73
465	974	136	140	RB	-0.15899	-0.47698	0	0.63596	OPLS (C_2-CT-CT-HC)
465	974	136	465	RB	2.9288	-1.4644	0.2092	-1.6736	OPLS (CO-CT-CT-CT)

Appendix E

Relating Semiaxes and Moments of Inertia

While not incredibly difficult, it is useful to write out how one computes the semiaxes from the moments of inertia as well as moving in the other direction to derive the moments of inertia from semiaxes. This relation is useful for several different works presented here. I begin by simply defining the moments of inertia for an ellipsoid, in a linear algebra format, which will become convenient shortly.

$$\begin{pmatrix} A \\ B \\ C \end{pmatrix} = \frac{M}{5} \begin{pmatrix} 0 & 1 & 1 \\ 1 & 0 & 1 \\ 1 & 1 & 0 \end{pmatrix} \begin{pmatrix} a^2 \\ b^2 \\ c^2 \end{pmatrix} \tag{E.1}$$

$$\begin{aligned} \frac{5}{M} \begin{pmatrix} -1/2 & 1/2 & 1/2 \\ 1/2 & -1/2 & 1/2 \\ 1/2 & 1/2 & -1/2 \end{pmatrix} \begin{pmatrix} A \\ B \\ C \end{pmatrix} &= \begin{pmatrix} -1/2 & 1/2 & 1/2 \\ 1/2 & -1/2 & 1/2 \\ 1/2 & 1/2 & -1/2 \end{pmatrix} \begin{pmatrix} 0 & 1 & 1 \\ 1 & 0 & 1 \\ 1 & 1 & 0 \end{pmatrix} \begin{pmatrix} a^2 \\ b^2 \\ c^2 \end{pmatrix} \\ &= \begin{pmatrix} 1 & 0 & 0 \\ 0 & 1 & 0 \\ 0 & 0 & 1 \end{pmatrix} \begin{pmatrix} a^2 \\ b^2 \\ c^2 \end{pmatrix} \end{aligned} \tag{E.2}$$

Where:

$$\begin{pmatrix} 0 & 1 & 1 \\ 1 & 0 & 1 \\ 1 & 1 & 0 \end{pmatrix}^{-1} = \begin{pmatrix} -1/2 & 1/2 & 1/2 \\ 1/2 & -1/2 & 1/2 \\ 1/2 & 1/2 & -1/2 \end{pmatrix}$$

In standard notation, this gives equations E.3.

$$\frac{5}{2M}(-A+B+C)=a^2 \tag{E.3a}$$

$$\frac{5}{2M}(A-B+C)=b^2 \tag{E.3b}$$

$$\frac{5}{2M}(A+B-C)=c^2 \tag{E.3c}$$

And so we have an expression both for computing the moments of inertia from the semiaxes in (E.1) and for computing the semiaxes from the moments of inertia in (E.3).

Appendix F

Derivation of CPE Equivalency

I am currently aware of two different formalisms that are similar to CPE. Both essentially distinguish between spherical and aspherical objects and include a second parameter that allows one to also differentiate between oblate and prolate ellipsoids. There is currently no generally accepted name for each of these sets of equations and so I have taken to calling them the Eta Parameters, named for the variable names given, and the Polymer Shape Parameters, named after the field who appears to predominantly use those equations. The Eta Parameters are given in (F.1) and the Polymer Shape Parameters are given in (F.2).

$$\eta_1 = 1 - \frac{I_{min}}{I_{avg}} \qquad \eta_2 = \frac{I_{max}}{I_{min}} \tag{F.1}$$

$$\Delta = \frac{3}{2}\frac{3\sum_{i=1}^{3}\left(\lambda_i - \bar{\lambda}\right)^2}{\left(\sum_{i=1}^{3}\lambda_i\right)^2} \qquad S = 27\frac{\prod_{i=1}^{3}\left(\lambda_i - \bar{\lambda}\right)}{\left(\sum_{i=1}^{3}\lambda_i\right)^3} \tag{F.2}$$

I have kept the original variables even though they overlap somewhat as there are slight differences. In the Eta Parameters, I_{min}, I_{max} and I_{avg} refer to the minimum, maximum and average (mean) principal moments of inertia, respectively. For the Polymer Shape Parameters, λ_i refer to each of the principal moments of inertia, and $\bar{\lambda}$ refers to the mean moment of inertia. While the similarities in variables, number of equations and even to some degree the function of the parameters to my own CPE are somewhat obvious, there are several clear differences that demonstrate why I have chosen to use CPE over the other available alternatives. First, it is important to note that while these other parameters exist, none of them appear to be widely adopted, as far as I was able to find, even to the point of lacking clearly defined names. Second, the limits, boundaries and therefore interpretations of each parameter vary wildly, even within each set (Eta and Polymer Shape parameters). In contrast, both values of CPE, e_{ab} and e_{ac}, vary between 0 and 1. This makes them nicely bounded and easy to interpret as well as symmetric. The way you interpret one axis is identical to the way you interpret the other, making for easy analysis. Finally, while CPE is derived from and could be written in terms of the principal moments of inertia if so desired, it is typically defined in terms of length, *e.g.* the semiaxes. This leads to a much more straightforward and intuitive interpretation.

I have been able to demonstrate that the CPE and the Eta parameters are equivalent and derived CPE in terms of the Eta parameters, given in (F.3). I strongly suspect the same could be done for the Polymer Shape parameters, although the effort is likely unhelpful and unproductive. The similarities are clear and the direct equivalence has already been proven once. So given that these are not incredibly popular parameters, there may be additional, similar parameters, and that it seems clear that CPE is a more useful metric of shape, I take it for granted that some enterprising soul could prove it again as needed and leave the issue there.

$$\begin{aligned} e_{ab} &= \sqrt{2 + \frac{\eta_2(1-\eta_1)}{\eta_1 + \frac{1}{2}}} \\ e_{ac} &= \sqrt{\frac{(1-\eta_1)(\eta_2-1)}{\eta_1 + \frac{1}{2}}} \end{aligned} \tag{F.3}$$

To derive the result given in (F.3), I will re-write semi-axis lengths in terms of the moments of inertia as used in the Eta Parameters. Given that the Eta parameters are defined in terms of the principal moments of inertia while CPE is defined in terms of the semiaxes, the relationships between them are key. This has been addressed in Appendix E. Although CPE and the Eta Parameters make use of all three principal moments of inertia, they use slightly different notation. These conventions can be interconverted by the relations:

$$A = I_{min} \tag{F.4a}$$

$$C = I_{max} \tag{F.4b}$$

$$B = 3I_{avg} - I_{min} - I_{max} \tag{F.4c}$$

where the last follows from the basic definition of a mean. Plugging equations F.4 into equations E.3, I obtain equations F.5.

$$a^2 = \frac{5}{2M}\left(3I_{avg} - 2I_{min}\right) \tag{F.5a}$$

$$b^2 = \frac{5}{2M}\left(-3I_{avg} + 2I_{min} + 2I_{max}\right) \tag{F.5b}$$

$$c^2 = \frac{5}{2M}\left(3I_{avg} - 2I_{max}\right) \tag{F.5c}$$

These equations can then be substituted into the definitions of CPE, as provided in Section 3.1 of the main paper, to obtain equations F.6.

$$e_{ab} = \sqrt{\frac{6I_{avg} - 4I_{min} + 2I_{max}}{3I_{avg} - 2I_{min}}} \tag{F.6a}$$

$$e_{ac} = \sqrt{\frac{2I_{max} - 2I_{min}}{3I_{avg} - 2I_{min}}} \tag{F.6b}$$

In order to best accomodate the equivalency, however, it is preferable to re-write these equations as shown in equations F.7.

$$e_{ab} = \sqrt{2 + \frac{2I_{max}}{(2I_{avg} - 2I_{min}) + I_{avg}}} \tag{F.7a}$$

$$e_{ac} = \sqrt{\frac{2I_{max} - 2I_{min}}{(2I_{avg} - 2I_{min}) + I_{avg}}} \tag{F.7b}$$

Focusing only on e_{ac} for the time being, notice that there is a $I_{avg} - I_{min}$ term in the denominator that is closely related to η_1. We can solve equation F.8 to match this formulation.

$$\eta_1 = \frac{I_{avg} - I_{min}}{I_{avg}} \tag{F.8}$$

Then I can plug this into equation F.7b and simplify the result.

$$\begin{aligned} e_{ac} &= \sqrt{\frac{2I_{max} - 2I_{min}}{2\eta_1 I_{avg} + I_{avg}}} \\ &= \sqrt{\frac{2I_{max} - 2I_{min}}{I_{avg}(2\eta_1 + 1)}} \\ &= \sqrt{\frac{1}{(\eta_1 + \frac{1}{2})}\left(\frac{I_{max}}{I_{avg}} - \frac{I_{min}}{I_{avg}}\right)} \end{aligned} \tag{F.9}$$

Once again, I can re-write equation F.8 as follows.

$$I_{min} = I_{avg}(1 - \eta_1) \tag{F.10}$$

This new formulation can now be plugged into equation F.10 to provide a way of relating I_{max} to I_{avg}.

$$\eta_2 = \frac{I_{max}}{I_{avg}(1-\eta_1)} \tag{F.11}$$

This is now equivalent to one of the terms in equation F.9 and can be substituted in. The other term still containing any of the eta parameter's moments of inertia variables is solved for trivially from equation F.10 and can also be substituted in to obtain the final equation.

$$\begin{aligned} e_{ac} &= \sqrt{\frac{1}{\eta_1+\frac{1}{2}}\left(\eta_2(1-\eta_1)-(1-\eta_1)\right)} \\ &= \sqrt{\frac{(1-\eta_1)(\eta_2-1)}{\eta_1+\frac{1}{2}}} \end{aligned} \tag{F.12}$$

e_{ab} can be solved for similarly. First I will substitute equation F.8 into equation F.7a.

$$e_{ab} = \sqrt{2+\frac{1}{\eta_1+\frac{1}{2}}\frac{I_{max}}{I_{avg}}} \tag{F.13}$$

I can then substitute equation F.11 into equation F.13 to obtain the final result.

$$e_{ab} = \sqrt{2+\frac{\eta_2(1-\eta_1)}{\eta_1+\frac{1}{2}}} \tag{F.14}$$

Appendix G

Median of Mean Curvature as a Function of CPE

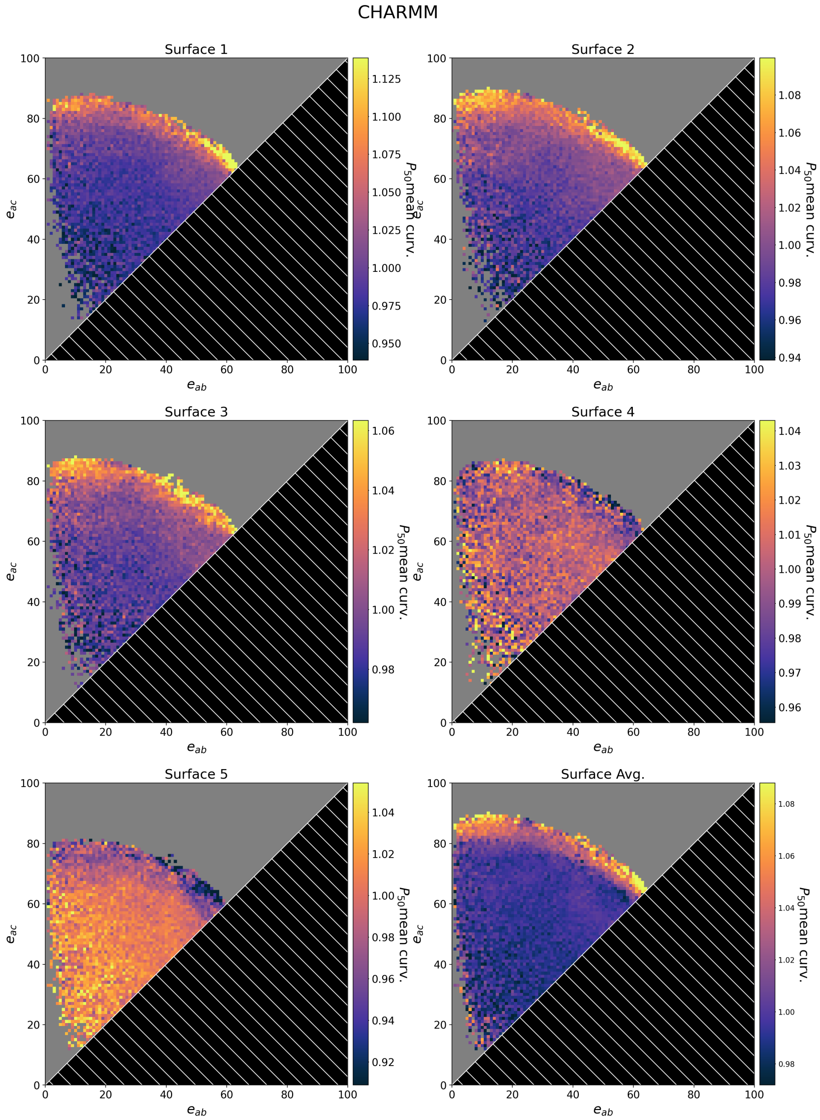

Figure G.1: a-e) A heatmap of CPE colored according to the median value of mean curvature when the RM has the CPE value indicated for the CHARMM simulation. Each subplot displays the mean curvature as a function of CPE for the surface as indicated at the top of the plot. f) The average distribution of mean curvature as a function of CPE over all surfaces.

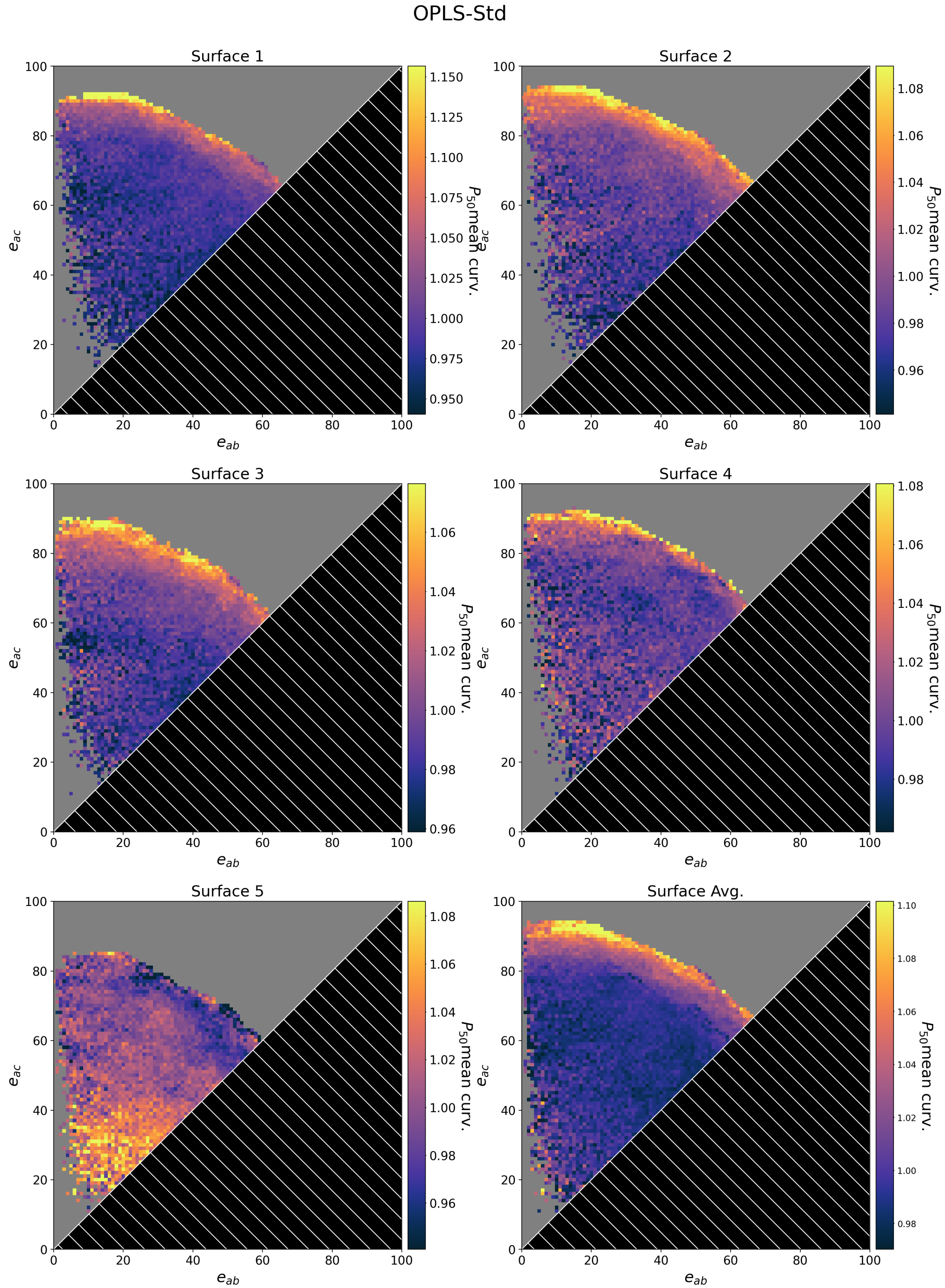

Figure G.2: a-e) A heatmap of CPE colored according to the median value of mean curvature when the RM has the CPE value indicated for the OPLS-Std simulation. Each subplot displays the mean curvature as a function of CPE for the surface as indicated at the top of the plot. f) The average distribution of mean curvature as a function of CPE over all surfaces.

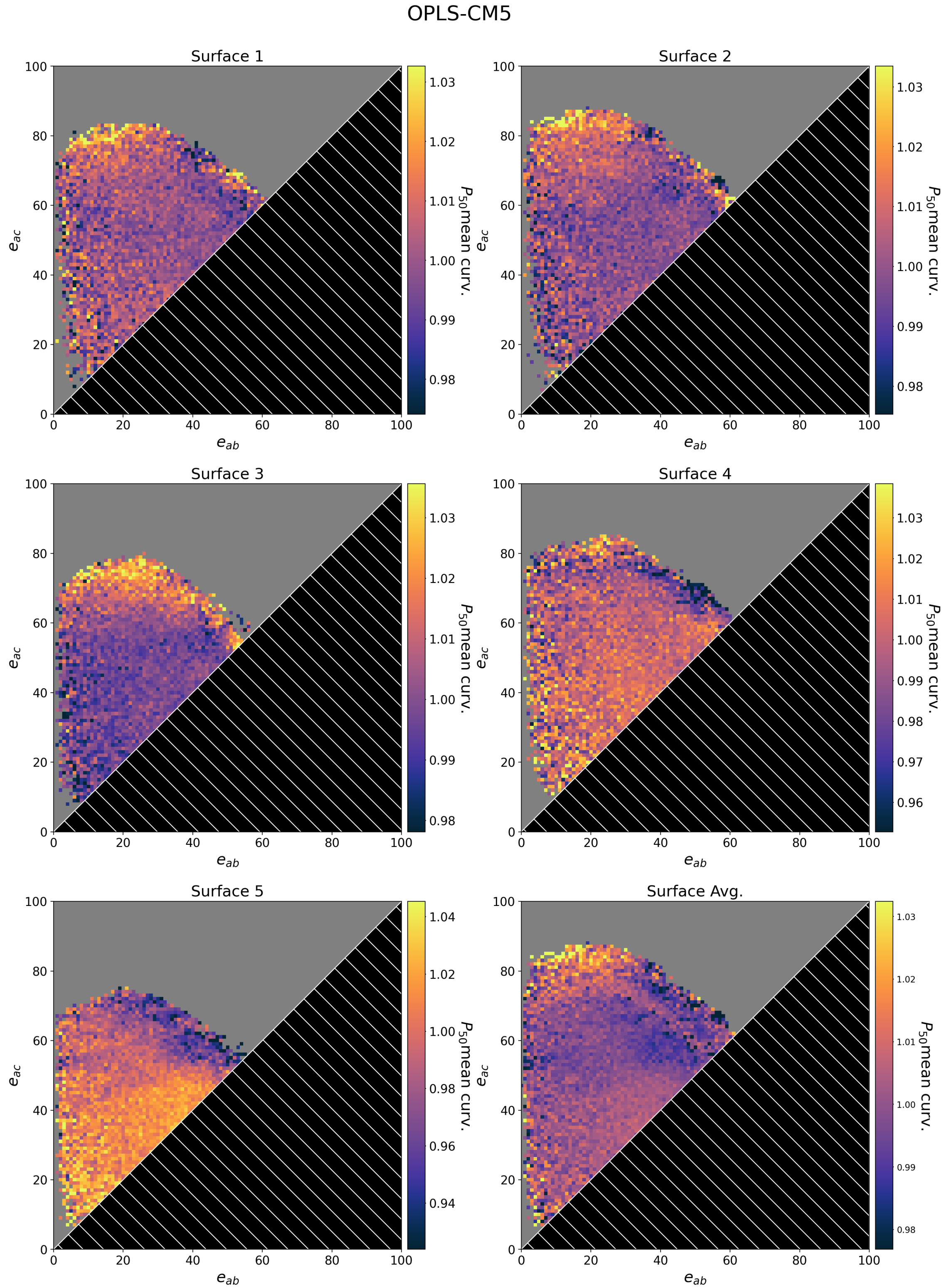

Figure G.3: a-e) A heatmap of CPE colored according to the median value of mean curvature when the RM has the CPE value indicated for the OPLS-CM5 simulation. Each subplot displays the mean curvature as a function of CPE for the surface as indicated at the top of the plot. f) The average distribution of mean curvature as a function of CPE over all surfaces.

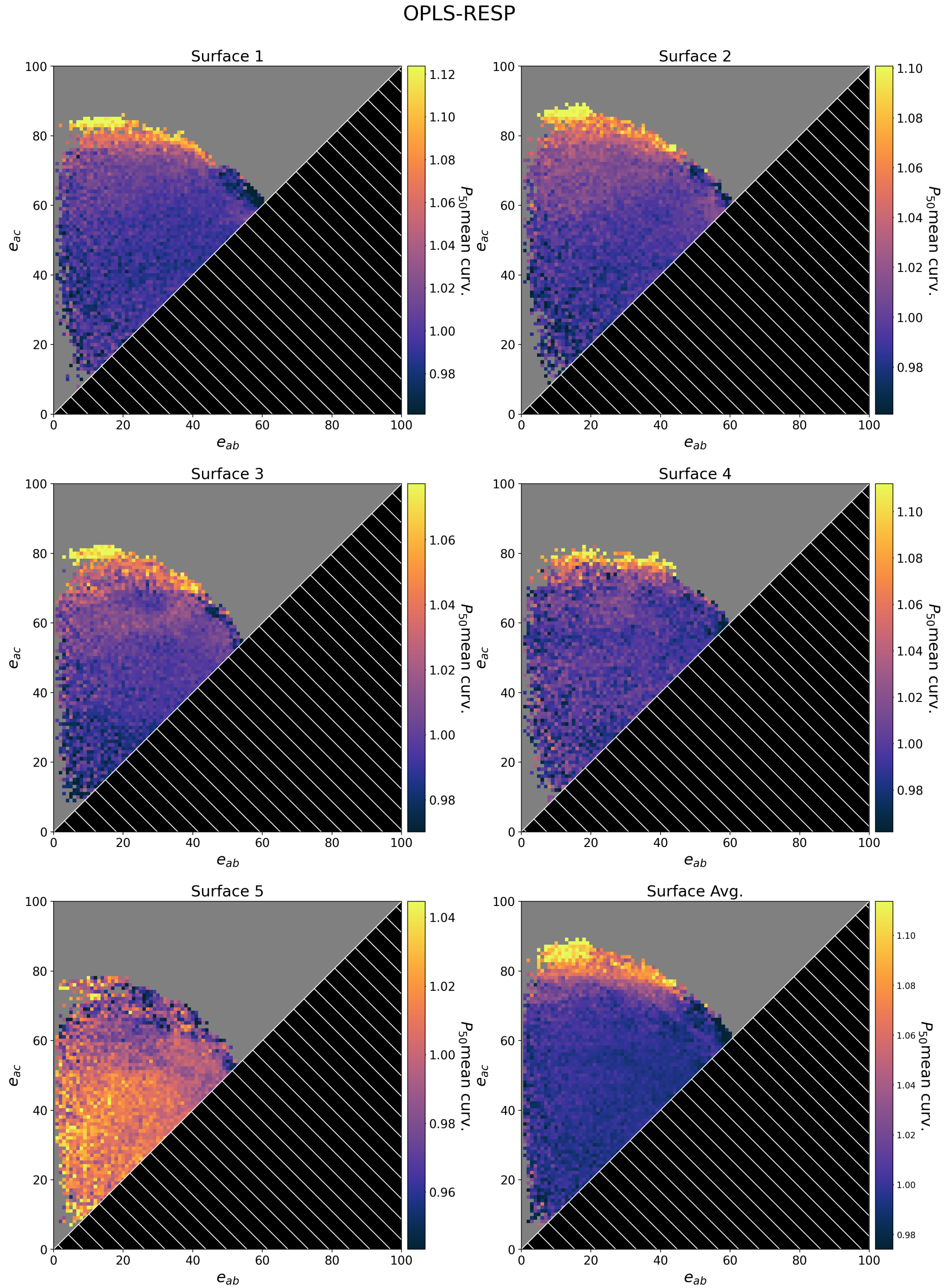

Figure G.4: a-e) A heatmap of CPE colored according to the median value of mean curvature when the RM has the CPE value indicated for the OPLS-RESP simulation. Each subplot displays the mean curvature as a function of CPE for the surface as indicated at the top of the plot. f) The average distribution of mean curvature as a function of CPE over all surfaces.

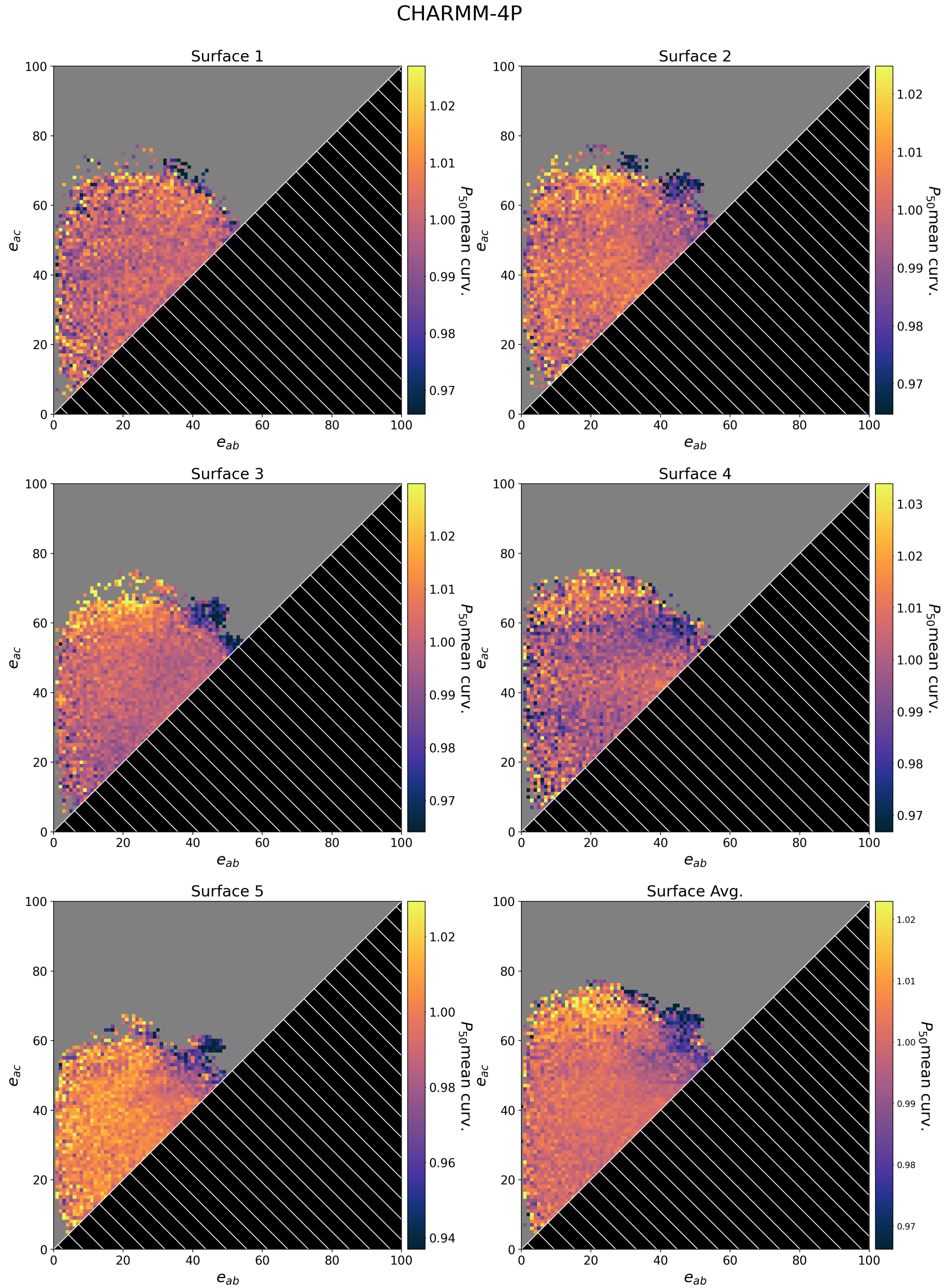

Figure G.5: a-e) A heatmap of CPE colored according to the median value of mean curvature when the RM has the CPE value indicated for the CHARMM-4P simulation. Each subplot displays the mean curvature as a function of CPE for the surface as indicated at the top of the plot. f) The average distribution of mean curvature as a function of CPE over all surfaces.

Appendix H

Water Rotational Anisotropy Decay, Fit Parameters

All of the fits reported in this work used the fit function given by equation H.1, a double stretched exponential function.

$$f(t) = A_1 e^{(-t/\tau_1)^{\beta_1}} + A_2 e^{(-t/\tau_2)^{\beta_2}} \tag{H.1}$$

The fitted parameters for each simulation are provided in Table H.1.

Simulation	A_1	τ_1	β_1	A_2	τ_2	β_2
CHARMM	0.0379	61.54	0.0587	0.9525	0.9460	0.4450
OPLS-Std	0.4659	42.3516	0.1610	0.5251	13.4902	0.5861
OPLS-CM5	0.5815	7.2502	0.7107	0.4104	1.9838	0.1802
OPLS-RESP	0.4616	92.5047	0.1014	0.5455	11.1161	0.6729
CHARMM-4P	0.1660	64.2397	0.0033	0.8323	5.1406	0.4972

Table H.1: Fit Parameters

Appendix I

Full Range Radial Distribution Functions

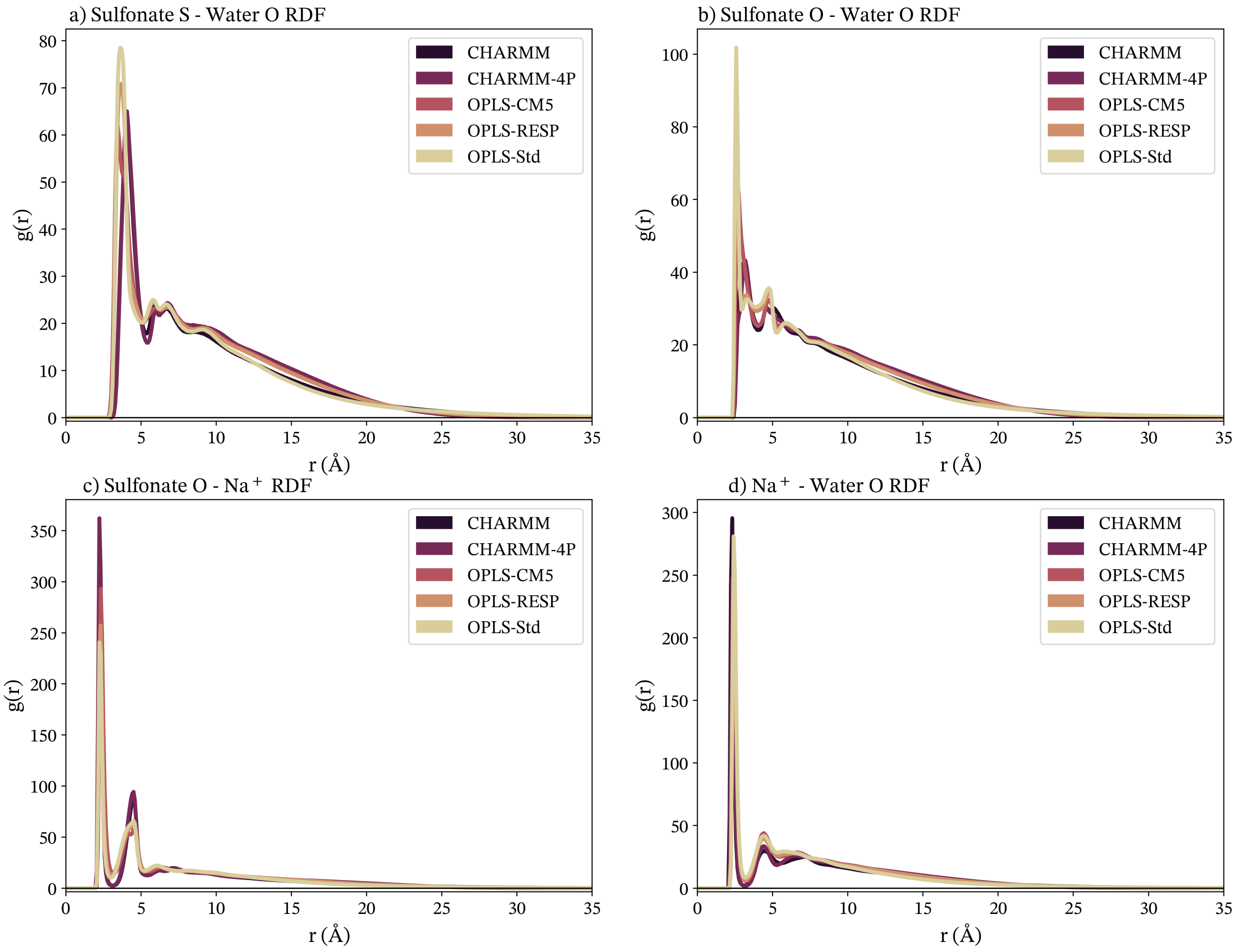

Figure I.1: Radial Distribution Functions for some key atoms in the AOT reverse micelles, labeled above the plots. This figure shows the full range of the RDF, out to the maximum distance possible for the simulations performed here and showing that the RDF has decayed to 0.

Appendix J

Concerning Hedgehogs

Postulate 1: Hedgehogs have names.

Lacking any discernible language, it is impossible to know for certain whether the wee animals have any names. Plato may argue that each thing is simply a reflection of its true Form (*ειδος*), saying “Nor, again, if a person were to show that all is one by partaking of one, and at the same time many by partaking of many, would that be very astonishing. But if he were to show me that the absolute one was many, or the absolute many one, I should be truly amazed,” (Socratic Dialogue: Parmenides); but on the other hand, chemists are well aware of the simultaneous, paradoxical, and oddly Daoist peculiarity and uniformity of particles. 像「道可道，非常道」，和阴阳, a molecule is both entirely unique and entirely interchangeable with every other copy of that molecule. Take for instance a water molecule in the reaction center of an enzyme. This water molecule is identical to every other water molecule and could be interchanged at will with no difference, but at the same time, that water molecule is occupying a position that is both important and brilliantly unique, if for just that brief moment. And so why should a hedgehog not have a name to clearly indicate their unique position and experience, regardless of what Plato says?

Lemma 1: If hedgehogs have names, then there is a hedgehog named Craig.

According to the US Census, just 2,000 names are needed to identify roughly 86% of the population, and there are about 4,000 names in common use[156]. There are estimated to be about a million hedgehogs currently alive in the wild, with a lifespan of about 5 years. Assuming that the population is evenly split between yearly generations over a 5 year total lifespan, there are roughly 200,000 hedgehogs born each year. Hedgehogs evolved approximately 15 million years ago, so while the modern population is conservative, we can safely assume that there have been at least 3 trillion unique hedgehogs on Earth at various points in time. Therefore, it seems exceedingly likely that at least one of them was named Craig. Specifically, the probability that at least one hedgehog has been named Craig, $\mathbf{P}_{\text{Craig}}$, is given in (J.1).

$$\begin{aligned}\mathbf{P}_{\text{Craig}} &= 1 - \mathbf{P}_{\text{Not Craig}} \\ &= 1 - (3999/4000)^{3{,}000{,}000{,}000{,}000} \\ &= 1 - 4.762 \times 10^{-325{,}761{,}584} \approx 1 \end{aligned} \tag{J.1}$$

Theorem 1: There exists a hedgehog named Craig the Valiant, Knight of Shape, Plato's Bane.

The Hedgehog Hypothesis was named after Craig the Valiant, in honor of his valor at the Battle of Leftover Peach Cobbler. Any useful, analogous aspects of the hedgehog to my work are purely coincidental.

Appendix K

Research is Good: But Could it be Better?

Research is good. It has to be. We are doing it and we did not waste our lives, therefore it must be good. Could it be better? If it could be better, it could also be worse so it is best to simply leave it as is. However, after bravely considering the options, I will meddle with what works anyway; and I have noticed that we usually only publish positive results. Which is to say, we only publish things we believe to be true more likely than not. But why would one only paint in a single color? That is called a sketch and they are always terrible. One should paint with at most two colors, and no less. Like a game of minesweeper, if we click enough things, we can outline the truth, potentially avoid certain death, and maybe even learn something. So in order to investigate AOT and reverse micelles more efficiently, I have turned to our most trusted institutions for inspiration: casinos. In a Monte Carlo-style spread of credibility, I have prepared a list of false facts. Each one has been double checked for lack of accuracy and certified to be more disingenuous than the last. Sit back, relax, and enjoy the future of science.

- There are 5 z's in the correct spelling of AOT. The third one will surprise you.
- AOT was the secret ingredient in "New Coke"
- AOT was the inspiration behind "Slurm"
- AOT reverse micelles can only be properly enjoyed from a comfortable chair (This is false, they may also be enjoyed from a comfortable bed)
- AOT is what plants crave
- AOT does not obey Newton's Laws of Motion. It prefers Abigail's Three Recommendations.

- AOT painted the Mona Lisa, but insisted on giving credit to Leonardo da Vinci to boost the poor, dumb man’s spirit
- AOT plays League of Legends as a Riven main and is responsible for 95% of all salt in the community
- The one disagreeable dentist recommends AOT for superior teeth
- AOT reverse micelle’s shape is better than your shape

Please do not add to this list at home. Only a trained professional and subject matter expert is certified to safely be this wrong.

Appendix L

The unanimous Declaration of the thirteen united State Functions of America

When in the Course of human events, it becomes necessary for one people to dissolve the scientific theories which have connected them to their surroundings, and to assume among the powers of the earth, the separate and quantized reality to which the Laws of Nature and Nature's God entitle them, a decent respect to the opinions of mankind requires that they should declare the causes which impel them to quantization.

We hold these truths to be self-evident, that all particles are created equal, that they are endowed by their Creator with certain unalienable wave-like properties, that among these are interference, group velocity, and the pursuit of Happiness. –That to secure these properties, Wavefunctions are instituted among particles, deriving their just powers from the consent of the particles, – That whenever any Form of Wavefunction becomes non-orthonormal, it is the Right of the Particles to alter or to abolish it, and to institute a new Wavefunction, laying its foundation on such principles and organizing its powers in such form, as to them shall seem most likely to effect the Gram-Schmidt Orthonormalization. Prudence, indeed, will dictate that Wavefunctions long established should not be changed for light and transient causes; and accordingly all experience hath shewn, that Wavefunctions should be changed for light and other electromagnetic effects. But when a long train of abuses and usurpations, pursuing invariably the same Object evinces a design whereupon UV, X-ray, and gamma radiation should dominate the solar spectrum; and whereupon the reason for discrete particles to be ejected from a metallic surface should be related to the intensity, rather than the frequency, of the incident light; it is their right, it is their duty, to throw off such Theories, and to provide new Guards for their future self-consistency. –Such has been the patient sufferance of these Particles; and such is now the necessity which constrains them to alter their former Systems of Description. The history of the present Descriptors of the Particles is a history of repeated injuries and usurpations, all having in direct object the establishment of an absolute Tyranny over these Particles. To prove this, let Facts be submitted to a candid world.

They have refused their Assent to Theories, the most wholesome and necessary for the public good. They have forbidden the accurate description of directly observable phenomena of immediate and pressing importance. They have refused to pass other Laws for the accomodation of large bodies of observed data, unless those data relinquish the Right of Verisimilitudinous Representation in the Academic Literatures, a right inestimable to them and formidable to tyrants only. They have called together deliberative bodies at places unusual, uncomfortable, and distant from the depository of their public Records, for the sole purpose of fatiguing them into compliance with their measures. Probably. Conferences are always so far away. They have affected to render the Military independent of and superior to these Natural Laws of Physics, self-evidently shewn. They have imposed Taxes on the Particles without their Consent; and against all Common Reasoning and Modest Ambitions.

In every stage of these Oppressions We have Petitioned for Redress in the most humble terms: Our repeated Petitions have been answered only by repeated injury. A Prince whose character is thus marked by every act which may define a Tyrant, is unfit to be the ruler of a free people.

We, therefore, the Representatives of the Particles of the united State Functions of America, in General Congress, Assembled, appealing to the Supreme Judge of the world for the rectitude of our intentions, do, in the Name, and by Authority of the good Particles of these Colonies, solemnly publish and declare, That these United

Colonies are, and of a Right ought to be, Free and Independent of the Continuous Model of Light and Pure Particle Corollary; that they are Absolved from all Allegiance to These Principles, and that all scientific connection between them is and ought to be totally dissolved; and that as a Free and Independent State Function, they have full Power to levy Molecular Bonding, conclude Fluorescence, contract Excitation, establish the Energy of the system, and to do all other Acts and Things which Independent State Functions may of right do. And for the support of this Declaration, with a firm reliance on the protection of divine Providence, we mutually pledge to each other our Half-Lives, our Probabilities, and our Spooky-Action-At-A-Distance.

“So long, and thanks for all the fish.”

— Douglas Adams, *The Hitchhiker’s Guide to the Galaxy*